EVOLUTION OF DROPLET DISTRIBUTIONS IN HYDRODYNAMIC SYSTEMS

Dissertation
for the award of the degree
“Doctor rerum naturalium”
of the Georg-August-University Göttingen

submitted by

Tobias Lapp
from Buxtehude

Göttingen 2011

Member of Thesis Committee (Reviewer): Dr. Björn Hof
Complex Dynamics and Turbulence, Max-Planck-Institute for Dynamics and Self-Organization

Member of Thesis Committee (Reviewer): Prof. Dr. Jürgen Vollmer
Dynamics of Complex Fluids, Max-Planck-Institute for Dynamics and Self-Organization

Member of Thesis Committee (Reviewer): Prof. Dr. Andreas Tilgner
Institute for Geophysics, University of Göttingen

Date of the oral examination: 25th November 2011

Declaration

I hereby declare that I have written the present thesis independently and with no other sources and aids than quoted.

Göttingen, 31$^{\text{st}}$ October 2011

Great are the works of the Lord,
studied by all
who delight in them.

Psalm 111,2

Contents

1 Introduction

1.1 Droplet Distributions in Hydrodynamic Systems

The appearance of droplets is an every day phenomenon. We are familiar with water vapor condensing on cold glasses in winter, on a mirror after having a bath or on the lid of a cooking pan. When having a shower or using a deodorant in the morning, the day starts in the presence of droplets. Liquid droplets in a gas occur naturally in the atmosphere and manifest under different conditions as fog [47, 89], clouds [14, 36, 90, 103, 120], dew [16, 17, 19, 86] or steam [2, 136].

Furthermore, droplets are technically relevant in many fields, including sprays, humidifiers, heat exchangers [57, 97, 104, 117], combustion chambers, turbines [136] and food preparation [37].

A rich variety of phenomena is involved in the evolution of droplets. Droplets nucleate and grow by condensation or evaporate [101], depending on the ambient conditions. They can collide [61] and coalesce [138], be deformed and break up [122]. In the presence of gravity, droplets may sediment or drip off a substrate. Further more, chemical reactions and surfactants can affect the fate of droplets [119].

The size distributions of droplets are typically broad, polydisperse, sometimes mono- or bidisperse. Sometimes self-similarity in the distributions arises due to the interplay of several growth processes [18, 30, 51, 52, 83, 142], meaning that a rescaled part of the droplet distribution is statistically similar to the whole distribution.

Studying the evolution of droplet distributions is a crucial step in enhancing the understanding of physical processes in nature like the formation of rain [44, 90] or dew [16, 19]. Heat and mass transport as well as turbulence characteristics are affected significantly by the distribution of droplet sizes [62]. With online in situ measurements of the droplet distribution, industrial processes can be monitored and optimized by studying the effect of the process parameters on the droplet distribution [62, 70, 73].

In the presence of solid walls, wetting properties are important, yielding phenomena like drop-wise condensation, also called breath figures [3, 4, 18, 46, 52, 53, 91, 92]. In other cases, interaction with the carrier flow and sedimentation due to gravity dominate the picture [5, 75, 93, 110].

1.2 Aims and Scope of Thesis

The overall aim of this thesis is to investigate the evolution of droplet size distributions in hydrodynamic systems. For this purpose, two systems were chosen which allow to study different phenomena affecting the evolution of size distributions.

Breath Figures As a first paradigm we look at the formation of breath figures, where droplets nucleate on a surface. A natural example for breath figures is dew forming on leaves (figure 1.1(a)) or spider webs (figure 1.1(b)). The photograph in figure 1.1(a) shows a broad size distribution of droplets. Sliding down and coalesce of droplets can be observed. The shape of the droplets is controlled by the wetting properties of the surface.

(a) (b)

Figure 1.1: Breath figures in nature: Dew droplets can be found on two-dimensional substrates like a leaf (a[1]) and on effectively one-dimensional substrates like a spider's web (b[2]).

[1] http://commons.wikimedia.org/wiki/File:Dew_drops_on_a_leaf.jpg by Vishesh Bajpai (own work), CC-BY-SA-3.0 via Wikimedia Commons

[2] http://commons.wikimedia.org/wiki/File:Dew_on_spider_web_Luc_Viatour.jpg by Luc Viatour (www.lucnix.be), CC-BY-SA-3.0 via Wikimedia Commons.

The interplay of nucleation, diffusion, coalescence and sliding or dripping creates a self-similar and strongly correlated droplet pattern, that we study with means of digital image processing. To this end, we build an experimental setup and we develop an image processing algorithm based on the reflection patterns of the droplets to detect droplets in the range of 3μm to 3mm in radius. Experimental data are compared to molecular dynamic simulations of droplets on horizontal substrates performed by Blaschke [23]. We extend the scaling description from Family and Meakin [46] by relating breath figures to fractal packings. Further more, we develop a model for the lower cutoff of the droplet size distribution. We correct for the discrepancies of the description in [46] for the scaling of the size distribution and the change of the substrate fraction wetted by droplets. Then we analyze the correlations of the droplet pattern and relate it to the coalescence probability of droplets. We show that a kinetic equation based on a pairwise coalescence kernel is not suitable for modeling the evolution of the droplet size distribution.

Phase Separation As a second paradigm, droplets in slowly demixing binary fluids are investigated. A complex interplay between nucleation, diffusion, collisions and sedimentation yields an oscillatory behavior of the phase separation process [8, 15, 33, 60, 128–130]. A fully automated experimental setup is designed and constructed to visualize droplets down to a radius of 3μm. We develop a droplet detection and tracking algorithm in order to accurately measure the droplet size distribution and droplet and flow velocities. We show that the droplet size distribution undergoes repeated precipitation cycles of nucleation, diffusional growth, collisions and sedimentation. The observed cycle forms an analogy to the precipitation cycle observed in rain formation. In clouds, the micro-physics of the droplet evolution is coupled to large scale turbulence (see figure 1.2). The phase separation experiment however is much simpler because the influence of turbulence on the droplet dynamics is suppressed.

We study the parameter dependence of the oscillation period and amplitude finding a non-trivial dependence on the rate of temperature change. Based on a simple model equation for the droplet growth rate, we derive a prediction for the period and amplitude of the oscillation in droplet volume fraction. Further more, we predict a bottleneck in droplet growth that we relate to the evolution of the typical droplet radius in the experiment.

Figure 1.2: Cumulus cloud in Nepal[1]. Cloud droplets scatter light and therefore influence the heat balance of the earth's atmosphere. They couple the micro-physics of clouds to large scale turbulence.

[1] http://commons.wikimedia.org/wiki/File:Cloud_in_nepal.jpg by Krish Dulal (own work), CC-BY-SA-3.0 via Wikimedia Commons

In the next chapter 2, we investigate the formation of breath figures. It is followed by chapter 3 on the phase separation in binary fluids. Finally, we summarize our work and conclude with chapter 4.

2 Breath Figures

2.1 Introduction

The first studies of droplet patterns on plates go back to Lord Rayleigh [91, 92] and Aitken [3, 4]. They were motivated by the following observation: If one aspirates on a cold plate, the moisture condenses and the droplet pattern reveals dirt or imperfections on the plate. Depending on the wetting properties of the substrate, either a film is formed which appears dark, or droplets are created that scatter light [18]. These breath figures are a simple way of visualizing surface defects. In nature, these patterns can be observed as dew on leaves at chilly conditions (see figure 1.1(a)). In general, one finds three dimensional droplets on a two dimensional plane. However, three dimensional droplets can also be found on one dimensional wires, for example dew droplets on a spider's web (figure 1.1(b)) or on grooved surfaces [85]. Drop-wise condensation has been studied experimentally on a variety of systems. Léopoldès and Bucknall [68] looked at chemical patterned substrates and found droplets self-assembling and coalescing on the chemical boundaries between different wetting properties. Other examples for substrates and solvents include GaAs on Si [20], Ga on GaAs(001) [142] or tin on sapphire [46]. Also droplets on the surface air/paraffin oil or liquid crystals, or on cyclohexane near the melting point and super-hydrophobic patterned substrates were studied [17]. Finally, also water droplets on promoted copper surfaces [57, 117] have been used for investigations.

Technical studies on the evolution of breath figures have been motivated by the effort in optimizing heat exchangers [57, 97, 104, 106, 117]. The evaporation of droplets [101] and the condensation of water vapor on the surface of the condenser consumes or releases a significant amount of latent heat [12]. Additionally, droplets attached to a wall affect the fluid motion next to it. A distribution of droplets on a wall effectively creates a rough structure on the wall. If the biggest droplet radii become comparable to the thermal boundary layer thickness, this will further affect the heat transport [113]. Since the presence of droplets is a wide spread phenomenon, breath figures are relevant for a variety of disciplines, including medicine (sterilization process), agriculture (green houses) and hydrology (production of drinkable water) [17, 82, 86].

Our interest in studying breath figures is motivated by the following two observations: In the first place, they constitute an example for self-similar droplet distributions with non-trivial scaling properties [46] that are still not fully understood so far. In numerical simulations, Meakin, Beysens and coworkers [30, 45, 46, 51, 52, 79, 80, 112] investigated the evolution of the size distribution of the droplets and extended their analysis to arbitrary

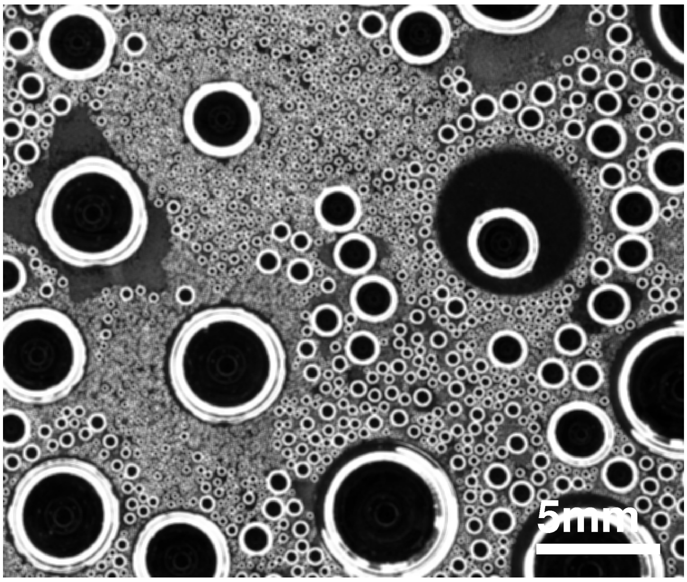

Figure 2.1: Water droplets on a glass plate covered by a polyethylene foil at 20°C. Contact line pinning is reduced and the droplets are almost perfectly spherical caps. A strong correlation between droplet sizes within neighborhoods can be observed.

dimensions of droplets and substrate. Family and Meakin provide theoretical predictions for the scaling of the size distribution [46], however, the simulated exponents deviate from the prediction, the origin of the deviation remaining unclear. We will resolve this issue by a careful analysis of the lower cutoff of the distribution and by comparing breath figures to fractal packings. In the second place, visual inspection of a breath figures, such as the one shown in figure 2.1 reveals a strong correlation between droplet sizes within neighborhoods. To our knowledge, this has not been looked into before, and we want to characterize and to understand the reason for these correlations.

To measure the droplet size distribution and the correlation between droplet sizes, we design and construct an experimental setup to produce breath figures in a well controlled manner. We set up an imaging system with two different resolutions to measure droplet sizes in the range of 3μm to 3mm. For each resolution, we develop an image processing algorithm from scratch to fully automatically detect more than 5000 droplets in each image for a broad range of radii. Taking about 10000 images during each measurement yields the basis for the statistical analysis of correlations.

In the following, we give a short outline of the structure of the chapter. We start by reviewing the state of the art modeling of breath figures in section 2.2. In section 2.3, the experimental setup is introduced and the measurement protocol is explained. We then describe in section 2.4 the image processing algorithms that we developed in order to detect the droplets. In section 2.5 we present the experimental results for the droplet size distribution and the pair distribution function. We compare our experimental results to our model and to numerical simulations of Blaschke [23]. The chapter is completed by a discussion in section 2.6.

2.2 State of the Art Modeling

In this section, we review the state of the art modeling for breath figures. First, we look at the wetting of substrates by individual droplets in section 2.2.1. Then, in section 2.2.2 we introduce the four stages in the evolution of breath figures which have been discussed in the literature. We introduce the concept of fractal packings in section 2.2.3, which will form a starting point for our analysis. Finally, we present a kinetic equation for the evolution of the droplet size distribution in section 2.2.4.

2.2.1 Wetting of Substrates

In order to understand the properties of droplet distributions on substrates, it is essential to be familiar with the wetting of substrates by individual droplets. The surface of a liquid is associated with a surface energy . It originates in the cohesiveness of the molecules that form the liquid. The molecules that are in the bulk of the fluid are attracted by molecules from all directions, so the net force is zero. Molecules residing on the surface are attracted from the bulk molecules yielding a net force normal to the surface plane towards the liquid. Therefore, it is energetically favorable to minimize the area of the interface between the two fluids. The energy which is necessary to increase the surface area is called surface energy or surface tension γ.

In figure 2.2 a sketch of a droplet in a gas phase attached to a solid substrate is shown. A three phase contact line forms with an apparent contact angle ϑ. The contact angle is determined by a balance between the surface energy of the liquid-gas (γ_{lg}), liquid-solid (γ_{ls}) and gas-solid (γ_{gs}) interfaces, as sketched in the figure. The balance of the tangential forces is described by the Young equation

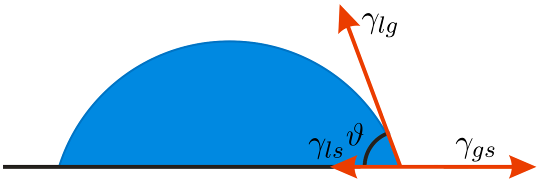

Figure 2.2: When a liquid droplet is attached to a solid, a three phase contact line forms. The liquid-gas interface forms an apparent contact angle ϑ. The tangential part of the liquid-gas surface tension γ_{lg} is balanced by the liquid-solid γ_{ls} and the gas-solid γ_{gs} tensions. The normal component of the liquid-gas surface tension is balanced by a small deformation of the substrate.

$$\gamma_{lg} \cos \vartheta = \gamma_{gs} - \gamma_{ls}. \tag{2.1}$$

The normal component of the liquid-gas surface tension is balanced by a small deformation of the substrate. In case of moving contact lines, advancing and receding contact angles usually differ from the static contact angle [42]. This phenomenon is known as contact angle hysteresis resulting from pinning of the contact line [115, 116] due to microscopic geometric imperfections or chemical impurities on the substrate [25, 94]. In general, this causes irregular droplet shapes, which have been observed in preliminary breath figure experiments with water droplets on a glass plate, shown in figure 2.3.

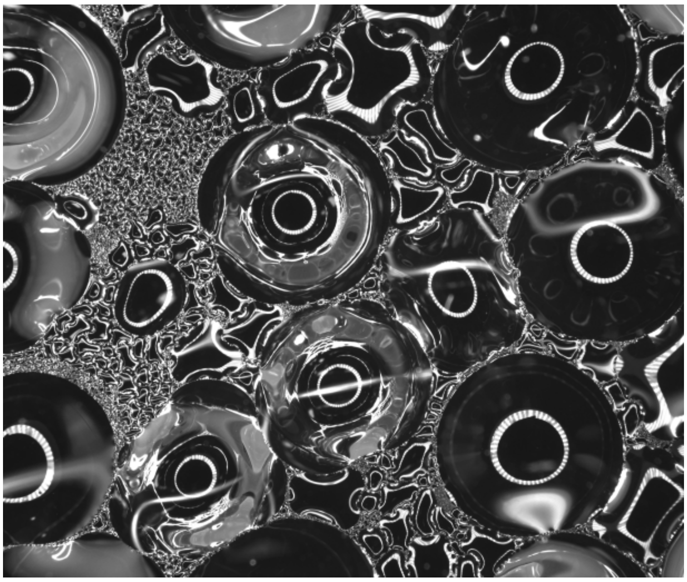

Figure 2.3: Water droplets on a glass plate at 20°C. Contact line pinning causes irregular shapes which can be seen by the reflections on the droplet surface. The dimensions of the image are 5 × 4 cm. The biggest droplets (diameter ∼1cm) are deformed by gravity, yielding a close to circular contact line.

For precise measurements of the droplet size and a detailed comparison to analytical models and numerical simulations, it is preferential to suppress pinning effects. Contact line pinning is smallest if the contact angle is close to 90°, when the liquid-solid and the gas-solid tensions have the same magnitude. A classical way to achieve this is immersing borosilicate glass plates into a hydrofluoric acid solution with subsequent silanization [18]. An alternative procedure is to cover the substrate by a thin polyethylene foil. It can be purchased as cling foil in the supermarket. The resulting droplet pattern consists of fairly circular droplets as can be seen in figure 2.4.

For small droplets, gravity can be neglected and the droplet shape has the form of a spherical cap, if pinning can be neglected. The size (i.e. volume) of droplets is given by

$$s(r,\vartheta) = c(\vartheta) r^3, \tag{2.2}$$

where $c(\vartheta)$ is a geometric function depending on the contact angle [116]

$$c = \frac{\pi}{3} \frac{2 - 3\cos\vartheta + \cos^3\vartheta}{\sin^3\vartheta}. \tag{2.3}$$

For a contact angle of $\vartheta = 90°$, the droplet size is given by equation (2.2) with $c = 2\pi/3$.

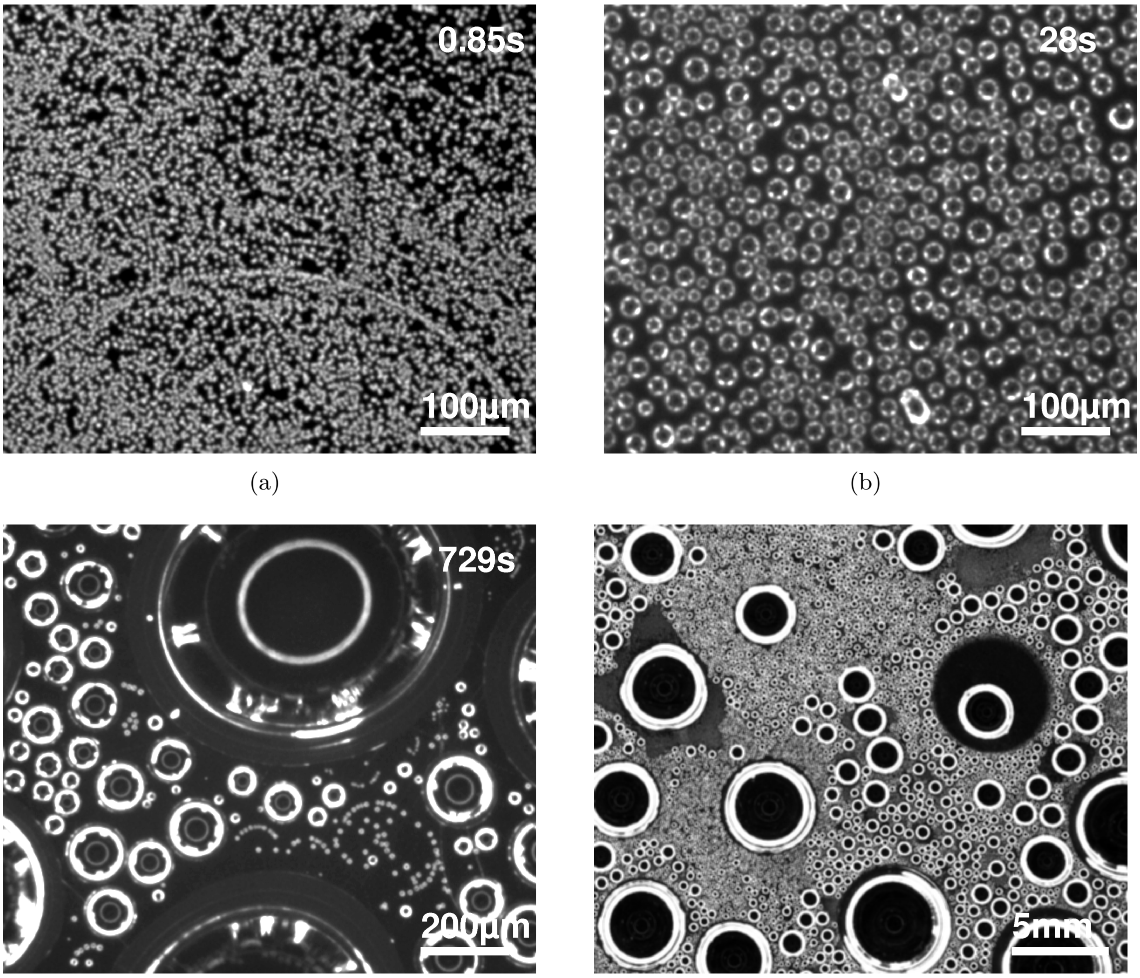

(a) (b)

(c) (d)

Figure 2.4: Water droplets on a polyethylene foil. Pictures representative for the four different regimes in the formation of breath figures are shown.
(a) Isolated growth regime (i): Droplets grow to a radius $R \sim 2\mu$m solely limited by diffusion, coalescences being insignificant.
(b) Intermediate-time regime (ii). Droplets grow to a radius $R \sim 12\mu$m by diffusion and coalescences. The size distribution is quite narrow with a radius polydispersity of about 0.18 [51] centered around a typical radius growing in time. The wetted fraction saturates at about 55%.
(c) Self-similar size distribution (iii): In the free substrate area between the droplets new generations of droplets are nucleated creating a bimodal size distribution. Many generations of droplets form a self-similar tail of the size distribution with a scaling regime. Note that the smallest droplets are relatively isolated compared to regime (ii). The biggest droplet at the top is relaxing after a coalescence event and therefore not circular yet.
(d) Steady-state drop-wise condensation (iv): Droplets with a radius $r \gtrsim 0.2 l_c$ close to the capillary length get distorted and eventually drip off. The released areas are repopulated by new generations of droplets. Many self-similar size distributions of type (iii) are growing next to each other on the substrate. After a few hours a steady-state is reached.
The time scale for the evolution of the droplet pattern depends on the volume flux onto the substrate. The photographs are taken in a measurement with the flux 0.13μm/s.

The length scale on which gravity dominates is the capillary length

$$l_c \equiv \sqrt{\frac{\gamma}{\rho g}}, \tag{2.4}$$

where γ denotes the liquid-gas surface tension, ρ is the density of the liquid and g=9.81m/s^2 is the gravitational acceleration. For a water droplet on air at 20°C, γ=72.8mN/m and ρ=0.998g/cm^3 giving l_c=2.73mm for the capillary length. When the radius of a droplet exceeds about 20% of the capillary length, it gets distorted and the shape deviates from a spherical cap [23, 135]. The details of the distortion depend on the contact angle and on the contact angle hysteresis [104].

2.2.2 Droplet Growth Regimes

Experimental studies of breath figures identified four stages of growth [51]. In figure 2.4 we present images recorded during an experiment, that are representative for the different regimes. After a big portion of the substrate is released by coalescence and dripping of big droplets, it is covered by a large number of rather isolated droplets (i) for about one second. In a subsequent intermediate time regime (ii), the droplets coalesce and form a distribution which is self-similar in time. This means that the shape of the distribution remains constant, only the mean droplet size evolves in time. After approximately half a minute, secondary nucleation sets in and a self-similar droplet size distribution (iii) develops. Two hours later, the radius of the first droplets gets close to the capillary length (2.4) and drip off. On the released area new generations of droplets form, yielding a steady state of drop-wise condensation (iv). In the following, the four regimes are described in detail. Note that the exact time scales of the regimes depend on the details of the system. The times given above correspond to an experimental run with a volume flux of 0.13μm/s onto the substrate.

2.2.2.1 Isolated Droplets (i)

At the beginning, the surface coverage is quite low. Therefore the droplets rarely coalesce and grow independent of each other. Briscoe and Galvin [31] distinguish two types of growth in this regime:

Type I: Diffusion Limited Type I growth is limited by diffusion of vapor or heat. Rogers et al. [95] give a derivation for the growth exponent of the droplet radius. We present a simplified version here, for a more thorough discussion the reader is directed to the literature [95]. From a boundary layer of thickness ξ monomers diffuse to the perimeter of the droplet

$$\dot{V} \sim \frac{D}{\xi} 2\pi r \tag{2.5}$$

where D denotes the diffusion coefficient, r the droplet radius and V the droplet volume. Hence in dimensionless quantities the radius growth rate reads

$$\dot{r} \sim \frac{1}{\xi r}. \tag{2.6}$$

To estimate the evolution of the boundary layer thickness, it is helpful to look at the depletion of monomers h in the boundary layer, which is proportional to

$$h \sim \pi r \xi. \tag{2.7}$$

On average, the number of monomers entering the growing droplet has to balance the amount leaving the boundary layer. Averaging over the droplet radius distribution $n(r)$ leads to the relation

$$\int \mathrm{d}r n(r) \dot{h} \sim \int \mathrm{d}r n(r) \dot{V}. \tag{2.8}$$

Following [95], we introduce averages over the radius distribution

$$\langle f \rangle \equiv \frac{\int \mathrm{d}r n(r) f(r)}{\int \mathrm{d}r n(r)}. \tag{2.9}$$

Inserting (2.6) and (2.7) into (2.8) and applying the product rule for differentiation gives

$$\xi \langle \dot{r} \rangle + \langle r \rangle \dot{\xi} \sim \frac{\langle r \rangle}{\xi}. \tag{2.10}$$

Multiplying by $\xi / \langle r \rangle$ yields

$$\frac{\xi \langle r^{-1} \rangle}{\langle r \rangle} + \xi \dot{\xi} \sim \text{const.} \tag{2.11}$$

Provided the second term on the left hand side asymptotically dominates over the first term, the asymptotic scaling of the boundary layer thickness follows [95]

$$\xi \sim t^{1/2}. \tag{2.12}$$

Together with (2.6) one gets the scaling for the droplet radius

$$r \sim t^{\mu} \tag{2.13}$$

with the growth exponent $\mu = 1/4$.

Type II: Flux Limited In the other case, the volume flux onto the substrate is limiting the growth rather than diffusion. The growth rate of the individual droplet volume V is given by

$$\dot{V} \sim \frac{F}{\pi(l/2)^2}, \tag{2.14}$$

where F is the volume flux on the substrate and l is the average droplet distance. In regime (i) coalescences can be neglected, implying that the droplet distance is constant. As a consequence, we find

$$\begin{aligned} V &\sim t \quad \text{and therefore} && (2.15)\\ r &\sim t^{1/3}, && (2.16) \end{aligned}$$

hence μ=1/3 [79, 123].

Usually in the isolated droplet regime, the droplet radius is difficult to measure in optical experiments because droplets are smaller than 2μm where the resolution is limited by diffraction.

2.2.2.2 Intermediate-Time Regime (ii)

After about one second, the droplets are closely packed and start to touch their neighbors. This happens, when the wetted fraction exceeds about 30% [17], compare figure 2.5. Coalescences of adjacent droplets are observed frequently (compare figure 2.4(b)). The free space between the droplets is so small that hardly any new droplets are nucleated. The size distribution is almost uniform [51] with a radius polydispersity of about 18% [17]. When a big droplet is formed by coalescence, the area is released around it so that it is relatively isolated for some time. During this time, smaller droplets can catch up and coalesce to form bigger droplets themselves.
Beysens and cooperators [16, 17, 30, 31, 51] emphasize that the wetted fraction w approaches a saturation value of about 55% in this regime. The increase of w by the individual growth of droplets is balanced by the release of substrate area through coalescences. This results in a droplet pattern that is self-similar in time. The droplet radius distribution $n(r,t)$ can be rescaled by the typical droplet radius $R(t)$

$$n(r,t) \sim f\left(\frac{r}{R(t)}\right) \tag{2.17}$$

where f characterizes the asymptotic shape of the distribution. The mean radius grows according to $R \sim t^{\mu_0}$ with $\mu_0 = 3\mu$, as can be seen in figures 2.5 and 2.6. Figure 2.5 (left) shows the mean droplet radius as a function of time, where the growth exponent changes from 1/3 to 1. Figure 2.5 (right) shows the evolution of the wetted fraction with time, saturating between 55% and 60%. The growth of an individual droplet is shown in figure 2.6. The factor between the two growth exponents is determined by the dimensions of the

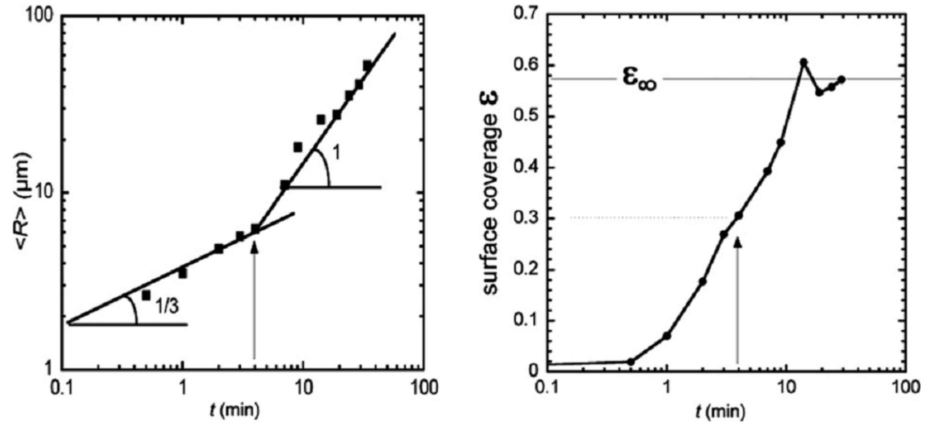

Figure 2.5: Evolution of the mean droplet radius (left) and the wetted fraction (right) in time. The growth exponent for the radius changes from $\mu = 1/3$ for isolated droplets (i) to $\mu_0 = 1$ for coalescing droplets (ii), when the wetted fraction is about 30%. The figure is taken from [17], showing experimental data for type II growth.

droplets δ_d and the substrate δ_s [123]

$$\mu = \mu_0 \frac{\delta_d - \delta_s}{\delta_d}. \tag{2.18}$$

Growth exponents $1/4 \leq \mu \leq 1/3$ are observed in experiments. Fritter et al [51] find an exponent that depends on whether temperature effects play a role or not. The relation $\mu_0 = 3\mu$ is demonstrated to be quite robust in the experiments of Fritter [51]. Based on a kinetic equation for the evolution of the droplet size distribution, which will be described later in section 2.2.4 and a scaling assumption for the droplet size distribution, Rogers et al. [95] also derive $\mu_0 = 3\mu$ for three dimensional droplets on two dimensional substrates.

2.2.2.3 Self-Similar Size Distribution (iii)

Formation of a Bimodal Distribution When the space between droplets reaches a critical size, diffusion of the monomers on the substrate towards the droplets is slow. Away from the droplets the nucleation threshold is reached at some imperfections of the substrate and secondary nucleation sets in. New droplets nucleate on the areas released through coalescences of droplets. A bimodal size distribution develops [51], which can be seen in the photograph in figure 2.4(c). The first generation of droplets continues to grow the way it did in regime (ii). The portion of substrate which is wetted by these droplets remains at about 55%. Inbetween the first generation droplets, the new generations of nucleated droplets form a distinct second part of the size distribution.

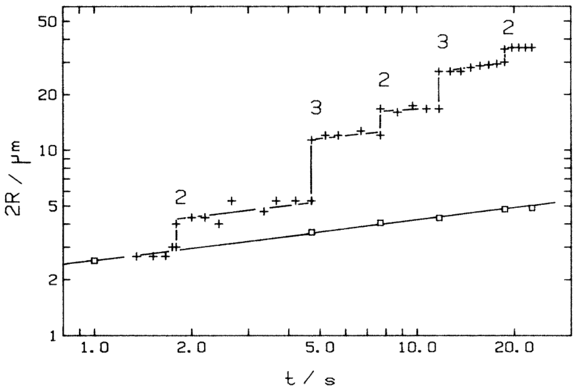

Figure 2.6: Growth of an individual droplet, as published in [18]. The individual droplet grows with exponent $\mu = 0.23$ between coalescences with adjacent droplets (type I growth). At a coalescence, the radius jumps resulting in steps in the radius evolution. The mean radius grows with the exponent $\mu_0 = 3\mu$.

Scaling of Size Distribution First simulations of the droplet size distribution in regime (iii) were performed by Family and Meakin [45, 46]. The result of their simulation for 3d droplets on 2d substrates is shown in figure 2.7. The number N_s of droplets of size (i.e. volume) s at different times are plotted (figure 2.7(a)). One observes the position of the peak in the size distribution (the oldest droplets) to grow in time. The tail of smaller droplets follows a power law distribution. The shape of the full distribution simulated in [46] is constant. This motivates a scaling approach for the description of the droplet size distribution

$$n(s,t) \sim s^{-\theta} f\left(\frac{s}{S(t)}\right) \tag{2.19}$$

where $S(t)$ is the typical size of the biggest droplets and $n(s)$ is the number of droplets per unit area. For $\theta = 5/3$ Family and Meakin [46] find that the distribution of different times can be perfectly rescaled, which is shown in figure 2.7(b).

Furthermore, they provide an argument based on (2.19) to derive the exponent θ as a function of the dimensions of the droplets δ_d and the substrate δ_s. For 3d droplets on 2d substrates their derivation is summarized in the following. Family and Meakin calculate moments of the size distribution without dealing explicitly with the boundaries of the integrals in [46]. In our exposition here, we will explicity keep track of the boundaries of integration over the size distribution in order to point out some pitfalls of the original argument. The size of the biggest droplets is assumed to scale with time according to

$$S(t) \sim t^z. \tag{2.20}$$

The volume in the system is proportional to the time t, i.e. the volume flux onto the substrate is fixed. Using (2.19) for the computation of the total volume per unit area

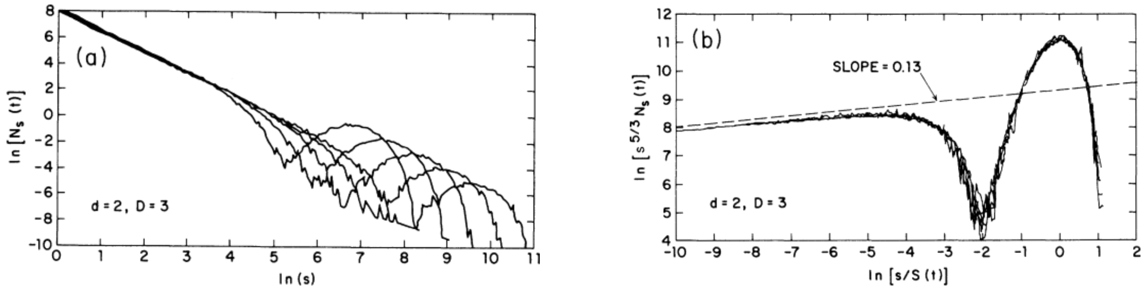

(a) (b)

Figure 2.7: Self-similar droplet size distributions, obtained in numerical simulations by Family and Meakin [46].
Left: The number of droplets N_s of size (i.e. volume) s is plotted for several instances in time.
Right: The number of droplets N_s is rescaled with $s^{5/3}$ and the droplet sizes s are rescaled by the size $S(t)$ of the "bump" in the distribution. The rescaled distributions at different times fall on top of each other. Note that the scaling assumption was used a priori in the design of the numerical scheme.

gives

$$\begin{aligned} t &\sim \int_{s_0}^{\infty} sn(s)\mathrm{d}s \\ &\sim \int_{s_0}^{\infty} s^{1+\theta} f\left(\frac{s}{S(t)}\right)\mathrm{d}s \\ &\sim S(t)^{2-\theta} \times \int_{s_0/S(t)}^{\infty} x^{1-\theta} f(x)\mathrm{d}x \\ &\sim t^{z(2-\theta)}. \end{aligned} \tag{2.21}$$

On the way the substitution $x \equiv s/S$ was used and s_0 is the size of the smallest droplets in the system. The last line follows from the assertion that the integral $\int_{s_0/S(t)}^{\infty} x^{1-\theta} f(x)\mathrm{d}x$ does not depend on time. We emphasise, that this is only true if

$$x^{1-\theta} f(x) \to 0 \text{ for } x \to 0 \tag{2.22}$$

We end up with a relation for the growth exponent of the size S and the exponent of the size distribution θ

$$1 = z(2-\theta). \tag{2.23}$$

To pin down the exponent θ, the wetted fraction of the substrate w is considered analogous to the volume density of the system (2.22)

$$\begin{aligned} w(t) &\sim \int_{s_0}^{\infty} s^{2/3} n(s,t) \mathrm{d}s \\ &\sim \int_{s_0}^{\infty} s^{2/3-\theta} f\left(\frac{s}{S(t)}\right) \mathrm{d}s \\ &\sim S(t)^{5/3-\theta} \times \int_{s_0/S(t)}^{\infty} x^{2/3-\theta} f(x) \mathrm{d}x. \end{aligned} \tag{2.24}$$

Family and Meakin argue that since the wetted fraction of the substrate cannot diverge, the scaling exponent has to be $\theta = 5/3$. Together with (2.23) follows $z = 3$, hence

$$S(t) \sim t^3. \tag{2.25}$$

. In their numerical work, they find $z = 2.92$, while the rescaling of the size distribution with the derived value for θ works very well.

Problems in Present Theory We see three problems in the presented theoretical description: At first, it is important to note that the scaling assumption was a priori used in the construction of the numerical scheme: In each time step, all droplets are rescaled by a certain factor and then overlapping droplets coalesce to bigger droplets. This way, the effect of lower or upper cutoffs for the size distribution are obscured.

In real physical systems, however, there is a smallest droplet size. Therefore, one has to keep track of the upper and the lower bounds of the integrals in (2.22) and (2.25). The integrals may diverge if the lower bound goes to zero and $f(x)$ does not go fast enough to zero for $x \to 0$.

Secondly, the scaling part of the rescaled size distribution is not flat (confer figure 2.7(b)), but a finite slope of 0.13 is observed. This slope is not explained in the theory presented by Family and Meakin [46].

Finally, it turns out that the wetted fraction is not a constant in regime (iii), but slowly increasing (confer section 2.5.1.6). The time dependence of w should therefore be accounted for in the analysis of (2.25).

2.2.2.4 Steady-State Drop-wise Condensation (iv)

Droplets residing on vertical substrates slide down once they reach a critical radius of the order of the capillary length, defined in equation (2.4) [104]. They coalesce with droplets on their way, yielding stripes in the droplet pattern. On the stripes, new generations of droplets are nucleated. After an initial transient, a steady-state is observed [80], where the size distribution depends on the vertical coordinate. The size distribution of droplets in the vertical setting was investigated by engineers because of the droplets' impact on the performance of heat exchangers [97, 117]. They found a droplet radius distribution of the form

$$n(r) \sim r^{-\theta_r} \text{ with } \theta_r \approx 2.7. \tag{2.26}$$

Note that this scaling of the radius distribution corresponds to the exponent 5/3-0.13 observed in the simulations of Family and Meakin [46] for the self-similar size distribution in regime (iii), when transferring radii into sizes (volumes) in (2.26).

Considering pendant droplets on a horizontal substrate, the situation is slightly simpler. Droplets of a critical radius drip off without sliding and new generations of droplets are nucleated in the released areas of the substrate, as can be seen in figure 2.4(d). In the latter setting, the distribution is isotropic and homogeneous in contrast to the vertical setting making data analysis and theoretical modeling more tractable.

How does droplet distortion and dripping of droplets due to gravity affect the droplet size distribution? Do we find the same scaling of the size distribution on horizontal substrates as the one measured on vertical substrates (2.26)?

2.2.3 Characterizing the Droplet Patterns: Fractal Packings

The size distribution of droplets in regimes (iii) and (iv) shows a self-similar pattern: Taking only a part of the droplet pattern and rescaling the size, it is statistically similar to the whole original pattern. Loosely speaking, this means that zooming into images of breath figures, they still look the same. For several orders of magnitude in length scale, the patterns are scale free. Only when looking at the smallest or the biggest droplets, the influence of fixed length scales is observed.

Self-similar packings of particles have been studied in great detail in order to characterize fractal packings [26, 27, 49, 58, 76, 77, 121]. Due to the self-similarity of the droplet pattern, breath figures can be regarded as a physical example for a fractal packing. Breath figures evolve from small scales to large scales. A fractal packing however is constructed vice versa. First big particles are added to the system, then free gaps are subsequently filled with smaller particles following certain rules. A variety of fractal packings have been described , which are characterized by a fractal dimension d_f

$$N \sim \left(\frac{R}{r}\right)^{d_f}, \tag{2.27}$$

Where N is the number of particles in the system, R is the radius of the biggest and r is the radius of the smallest particles. An example for a fractal packing [76] is shown in figure 2.8. This packing is created applying the rule that each disc should have exactly one neighbor. Interestingly the fractal dimenstion of this packing $d_f = 1.64$ turns out to be very close to the fractal dimension of breath figures, which we will determine in section 2.5.1. We will now present another approach that has been used to study the evolution of the droplet size distribution in regime (ii) [95].

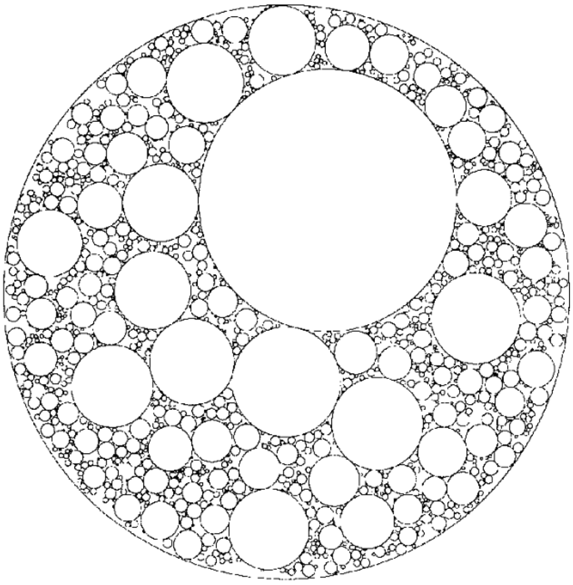

Figure 2.8: The random packing pattern shows 1500 disks. The packing created by Manna [76] has a fractal dimension of 1.64, which turns out to be very close to the fractal dimension of breath figures (confer section 2.5.1). The pattern is produced following the rule that each droplet has exactly one touching neighbor.

2.2.4 Kinetic Equation for Evolution of Droplet Size Distribution

Often, the aggregation of clusters is studied with the coagulation equation proposed by Smoluchowski [108]. It has been applied to breath figures, e.g. to derive the radio between the growth rates of individual droplets and mean droplet radius [95]. The Smoluchowski equation for the evolution of the size distribution reads

$$\frac{\partial n(s,t)}{\partial t} = \frac{1}{2}\int_0^s K(s-s',s')n(s-s',t)n(s',t)\mathrm{d}s' - \int_0^\infty K(s,s')n(s,t)n(s',t)ds'. \tag{2.28}$$

The first term on the RHS describes the creation of particles by collisions of smaller ones. The second term refers to the particles being consumed by collisions with other particles. This equation is only useful of course, if the factor $K(s,s')$ is known.

Applying a scaling argument, Family and Meakin [46] show that when rescaling the droplet sizes by a factor $s \to \lambda s$, the factor K has to be rescaled according to $K \to \lambda^{1/3}K$. They add terms to equation (2.28) to account for the intrinsic growth of individual droplets due to the volume flux from the vapor onto the droplets.

In the work of Rogers et al. [95] a guess for $K(r,r')$ is given (now refering to radii instead of sizes)

$$K(r,r') = 2\pi(r+r')(\dot{r}+\dot{r'}). \tag{2.29}$$

The radii of the coalescence partners are r and r'. The growth rates $\dot{r}$ and $\dot{r'}$ refer to the intrinsic droplet growth rates. Equation (2.29) is consistent with the scaling prediction of [46] mentioned above. Spatial correlations in the droplet pattern are not accounted for in equation (2.29). As we will show later, the average growth rate of individual droplets does not depend on size. Therefore we define a coalescence kernel by

$$\kappa(r,r') \equiv \frac{K(r,r')}{2\dot{r}}. \tag{2.30}$$

It will be used in the analysis of spatial correlations in breath figures (confer section 2.5.3). Provided the coalescence kernel is known, can the evolution of the droplet size distribution in regime (iii) to (iv) also be modeled by integration of the Smoluchowski equation (2.28)? We will try this in section 2.5.4. We now move on to describe the experimental setup that we designed to study breath figures.

2.3 Experiment

2.3.1 Experimental Setup

To study the evolution of the droplet size distribution in breath figures, we choose to look at pendant droplets on a horizontal substrate. Depending on the magnification, different regimes can be studied. When a low resolution is chosen (44.4 pixel/mm), a large portion of the substrate can be imaged and measurements for the steady-state regime can be taken for one or two days. With a high resolution (2.0 pixel/μm), however, it is possible to study regimes (i) to (iii) on a region released after a coalescence and dripping event. In the following, the details of the experimental setup are described.

Vapor Cell A sketch of the experimental setup is shown in figure 2.9. The setup is similar to a steam cooker: A heating plate at the bottom heats a layer of water (about 1cm height) which evaporates. The vapor is transported by convection to the cooled top plate, where it condenses. The glass plate is covered with polyethylene yielding a contact angle of about 90° [12] (compare figure 2.10). The droplets grow until they reach a critical size and drop. Using a constant heating power (16.2 W) and a constant top plate temperature of 20℃, the system is in a steady state after a few hours. The temperature of the top plate is controlled by a Haake thermostat DC 30 to $\pm$0.02K. A temperature sensor (PT100) measures the water surface temperature. The amplified signal is acquired by a National Instruments data acquisition card. The cell and the temperature sensor are coated with black color to reduce unwanted reflections.

Image Acquisition Images are taken with a JAI BM500 CL 2/3" CCD camera at a constant frame rate between 0.1Hz and 5Hz with the resolution of 2448$\times$2058 pixels. The data is transfered by a CameraLink cable to a frame grabber, which controls the camera. With an Edmund optics macro video zoom lens (f=18-108mm, numerical aperture 1/2.5) the magnification is adjusted to 44.4pixel/mm of the substrate. Alternatively, with the macro system and a f=35mm macro objective with aperture 1/2.8 of SCHNEIDER Optics a magnification of 2034pixel/mm is achieved. The camera is mounted on a custom-made stand with adjustable vertical and horizontal position and adjustable viewing angle. We developed a C++ executable based on C and C++ libraries and examples provided by SaperaLT to operate the camera. The acquisition time of each frame is recorded in a log file. the frame rate of each image series is calculated from the log file.

Illumination The substrate is illuminated applying a dark field illumination. When the substrate is clean, the images are dark. Light coming from the side is reflected by the droplets and projected on the camera chip. Two different devices are used for the illumination. For the low magnification images, a strip with LEDs is wound twice around a plexiglass plate (see figure 2.9). The LEDs of the two rings have alternating positions.

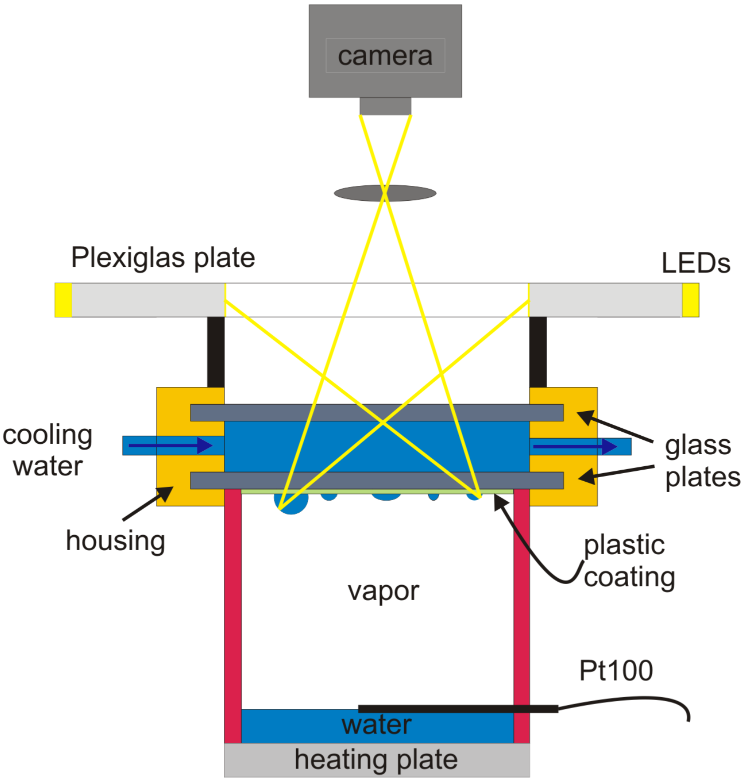

Figure 2.9: In the experimental setup water is heated from below, evaporates and condenses on a cooled glass plate coated with polyethylene. The droplets are illuminated with a double ring of LEDs, mounted on a tailor-made plexiglass light diffuser. A high resolution camera takes images of the droplet patterns.

The plexiglass acts as a diffuser yielding a homogeneous bright ring. For the high magnification images, a higher light intensity is required. For this purpose, a Zeiss cold light source KL 2500 is used with a ring-light. The illumination has to be centered around the optical axis of the camera and the objective, to ensure axial-symmetric reflection patterns of droplets in the images. The setup is shielded with a cylinder and a black sheet from stray light.

2.3.2 Experimental Procedure

The cell is cleaned and filled with deionized water to a level of one centimeter. The top plate is cleaned, dried and covered with dry polyethylene foil. Using gloves air bubbles and wrinkles are removed carefully. Then the foil is rinsed with deionized water to remove soluble molecules. After closing the cell, the temperature control and the heating plate are switched on and the camera is adjusted. After a few hours the system reaches a steady state and images are taken for one or two days. Typically after two days the foil has to be replaced.

For measuring the dynamics of the initial droplet growth the central area of a big droplet is viewed and a long sequence of images is taken. Once the droplet reaches a critical size

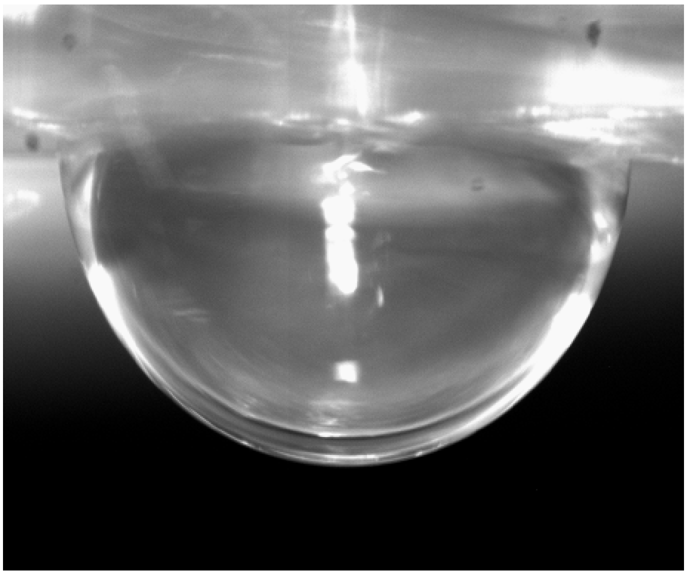

Figure 2.10: Pendant water droplet on polyethylene (side view). The contact angle is close to 90°, and the shape is well approximated by a hemisphere (confer section 2.2.1).

it drips off and new droplets are nucleated. If the observed part of the plate is completely released by the dripping event, the images after the dripping event are saved and the first part is deleted. If part of the image section is still covered by a big droplet after coalescing or dripping, the image sequence is deleted completely. For measuring the steady state distribution, a random area is selected and an image series is taken for one to two days. The main challenge of the project, however, was not the development of the experimental setup. It turned out to be very demanding to detect a broad distribution of droplets in the images simultanously. Most image processing tools work on a specified length scale. In the following section, the describe the algorithms that we developed from scratch to detect the droplets in the images automatically.

2.4 Image Processing

In the images, reflection rings are visible in each droplet, which can be seen on the photograph in figure 2.12. The shape of the reflection pattern depends on the illumination, the magnification and the droplet size. For each magnification and droplet size we developed a different image processing algorithm from scratch. The image processing algorithm for low resolution images (44.4 pixel/mm, see figure 2.4(d)) is described in section 2.4.1. In the high resolution images (2.0 pixel/μm, see figure 2.4 (a)-(c)), a broad distribution of droplet sizes is observable. We aim at detecting droplet radii in the range from 3 to 3000 pixels (note that the height of the images is only 2058 pixels). The algorithm for the droplet detection in high resolution images is outlined in section 2.4.2. It is based on a detailed analysis of the droplet reflection pattern, which is described in appendix 2.A. Readers who are not inclined to look into the details of the description of the algorithms are referred to the summary given in section 2.4.3.

2.4.1 Droplet Detection in Low Resolution Images

The basis of this algorithm was developed by Andrew Scullion during his internship. Two subalgorithms are developed to detect small droplets (about 4 to 17 pixel radius) and large droplets (about 14 to 105 pixel radius).

The contrast in the image of small droplets is enhanced by applying a high pass Fourier filter. Then it is binarized using a threshold and the dark regions (candidates for droplet centers, confer figure 2.11) in the image within a certain size range are detected. Regions with a high eccentricity or a large perimeter in comparison to the area are sorted out. The radius of the dark central region is related to the droplet radius by a quadratic function found by visual comparison of the result with the image.

To detect the large droplets, the image is binarized based on a threshold directly. Again, with adjusted thresholds for the maximal eccentricity and the perimeter the dark regions corresponding to the centers of large droplets are detected. They are related to the droplet radius with a similar function as the one used for the small droplets.

Finally, the list of small and large droplets detected by the algorithm is combined and multiple droplet detections are corrected for. Smaller droplets detected on areas where a large droplet was detected are deleted from the droplet list, too. The algorithm was validated by viusal comparison of the detected droplet radii with the raw image. Figure 2.11 shows the droplets detected by the algorithm superimposed as circles on the image. The color corresponds to the droplet radius. Above a certain radius threshold, almost all ($\gtrsim$ 999/1000) droplets are safely detected. This allows for automatically detecting and measuring coalescence events (see section 2.5.3.4 and figure 2.26). The only shortcoming is that we did not manage to glue the size distributions detected by the two subalgorithms perfectly together. This is the reason for the peak at $r \approx 0.13 l_c$ visible in figure 2.17(a).

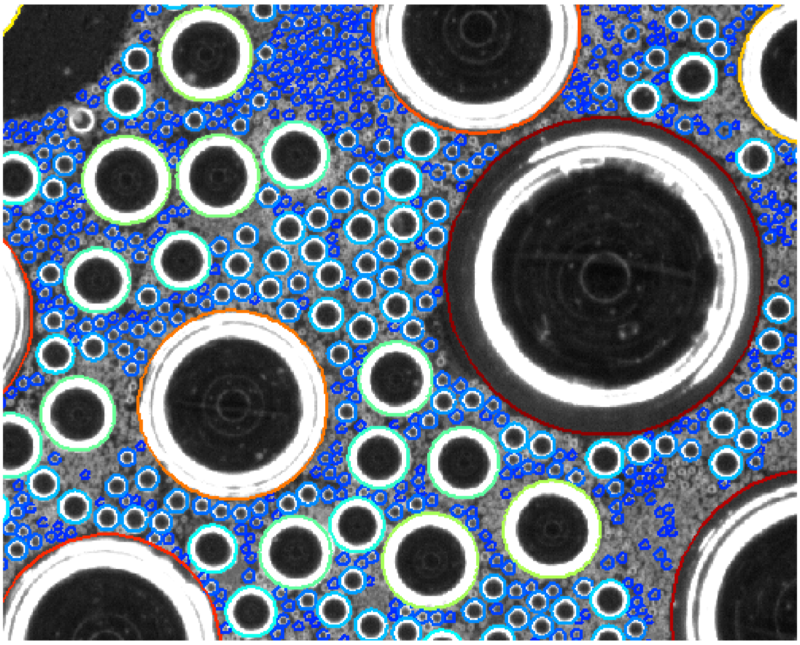

Figure 2.11: The droplets which are detected are superimposed as circles on the image. The color encodes the radius of the droplet. Here we show only the left top corner of the image. For scale: the biggest droplets are 2.4mm in radius.

2.4.2 Droplet Detection in High Resolution Images

For the detection of the droplets in the images with high resolution, the development of the algorithm was much more demanding. Whereas the algorithm presented above was programmed within a few days, for the development of the droplet detection algorithm for the high resolution images several months were needed. Detecting the droplets in these images is significantly more difficult for two reasons. In the first place, the range of droplet radii that are to be found is much larger (3 to 3000 pixel in radius). In the second place, droplets which are only partially visible inside the image can cover large portions of the image (confer figure 2.4(c)).

The following steps are taken in the image processing algorithm. First, the image is preprocessed to improve its quality. Secondly, a set of subroutines detects droplets of several size ranges. Then two different match functions (defined in the appendix 2.A.4) are used to compare the detected droplets to the image. The definition of the match functions is based on our study on the droplet reflection patterns, that are presented in the appendix 2.A. Finally, several methods are used to identify and remove artifacts. Again, visual comparison of the detection result with the image (see figure 2.12) is used to validate and optimize the algorithm. The droplet radius can be determined very precisely by the observation that overlapping droplets coalesce immediatelly.

2.4.2.1 Preprocessing

The image is filtered with a standard 3 × 3 pixel averaging filter to reduce noise. It is then deblurred with a Lucy-Richardson algorithm implemented in the MATLAB Image Processing Toolbox. This is necessary to detect droplets of less than 5 pixel radius. For the deconvolution, a Gaussian with half width 5 pixel is taken as an estimate for the point spread function. It is calculated by the blind deconvolution algorithm implemented in the MATLAB Image Processing Toolbox.

2.4.2.2 Droplet Classes

As the typical features of a droplet image depend on its radius, several subroutines are used to find "giant" (550 - 3000 pixels), "large" (40-1500 pixels), "medium" (15-90 pixels), "small" (9-30 pixels), "very small" (7-18 pixels) and "tiny" (3-15 pixels) droplets, respectively. Furthermore, another subroutine is developed to find "edge" droplets, which are only partially visible in the image.

The subroutines use different strategies to find droplet centers and to estimate the radius. Positions and radii are varied to find local maxima of the profile based match (2.110). Then the gradient based match function is used to get a consistent determination of the droplet radius for all droplet sizes - independent of the used detection subroutine. Finally, each subroutine sorts out artifacts in a number of steps, which will be described below in section 2.4.2.3. The precise order and parameters of match optimization and artifact reduction is different for each subroutine.

We now move on to introduce the seven subroutines which detect droplets within certain radius ranges. Each subroutine receives a list of the afore found droplets. These droplets are removed from the image to avoid parts of the reflection patterns of big droplets to be misinterpreted as small droplets. Note that the size ranges of the subroutine have significant overlaps to minimize the number of droplets that remain undetected. Figure 2.12 shows a snapshot as illustrative example, where the color of the droplets corresponds to the size range of the droplet classes.

Giant Droplets By giant droplets we refer to droplets which have a size comparable to the size of the field of view with radii in the range 550-3000 pixels. By thresholding the preprocessed image, the dark central region of the droplet is found. This central region may not necessarily be entirely visible in the image. The complement of the central region we denote as “background”. We look for the point which has the highest distance to the background and define it as the droplet center. By a linear interpolation we can infer the droplet radius (which may be bigger than the dimensions of the image) from the radius of the central region.

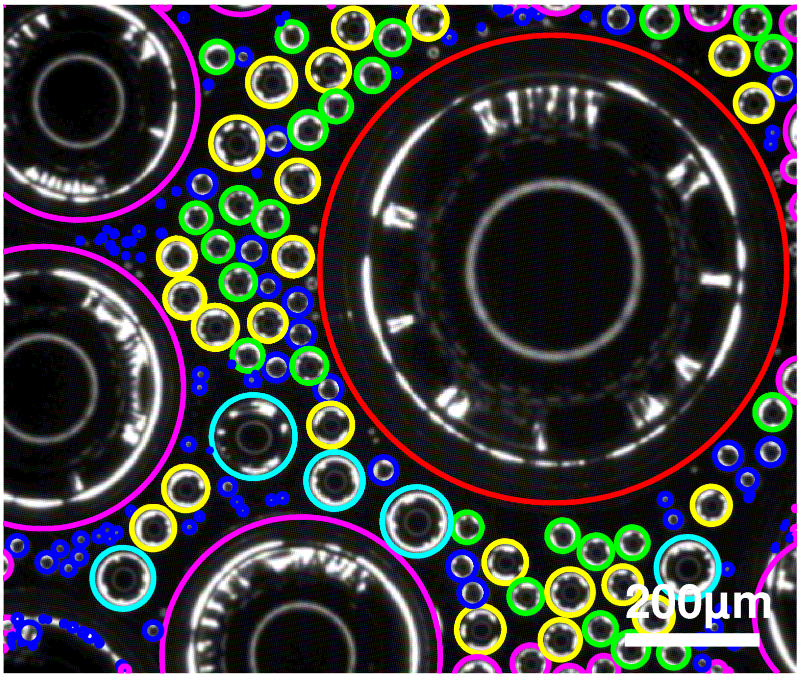

Figure 2.12: A typical snapshot showing seven classes of droplets detected by the image processing algorithm. For illustration, the color of the droplets corresponds to the size range of the droplet classes (overlaps of the size ranges are cut in halves). Large (red), medium (cyan), small (yellow), very small (green) and tiny (blue) droplets as well as droplets touching the edge (magenta) are found in the image.

Large Droplets Large droplets (40-1500 pixels) are also detected by finding the circular dark central regions with thresholding. Again with a linear function the droplet radius is estimated. The estimates of radii and positions are improved by optimizing the match to the image and artifacts are excluded from the droplet list.

The droplets which are found in this way are removed from the preprocessed image. Then a second routine looks for the large droplets which remained undetected. Some inner reflection rings are interrupted resulting in less circular central droplet regions. Applying less rigorous thresholds for the circularity of droplet centers, these regions can be found, too. Now the distance to the background (i.e. the complement of central regions) is used to find droplet centers and radii. Again the match to the image is optimized and artifacts are reduced. The droplet lists of the two routines are combined, double detections are combined and small droplets enclosed by bigger ones are deleted.

Medium Droplets By thresholding the image and by looking for extended minima in the image, the centers of medium droplets (15-90 pixel radius) are found. A linear function is used to estimate the droplet radius from the radius of the dark droplet center. The match functions are applied to improve the estimate of the coordinates (radius and position) and erroneous droplet detections are excluded from the droplet list.

Edge Droplets This subroutine makes several attempts to detect droplets which touch the edge and are only partially on the image. At first, droplets inside the image bigger than 50 pixel in radius are removed. By thresholding the image, the core regions of medium and large droplets are found. Then the droplet cores that touch one of the corners of the image are selected. By analyzing the extrema of the core region pixels (left, right, top and bottom end of the region), the center and the radius of the cores can be calculated. With a linear function the droplet radius is computed from the core radius. Then the remaining droplet cores touching the edge are analyzed. The image containing the cores is embedded into a bigger matrix. Then the distance of the background (everything but the droplet cores) is calculated and the distance to the original image is subtracted. Then extended maxima of this distance difference are detected. From the maxima the position and the radius of the droplets can be determined, even if the droplet centers are outside the image. The detected droplets are covered with black disks. Then reflection rings and regions between concentric reflection rings are detected. They are combined and the regions touching the edge of the image are selected. Then a similar procedure as described above is followed to find the droplet positions and radii.
Finally, position and radius of the edge droplets are varied to find an optimal profile based match. The radius is then determined by the optimum of the gradient based match. Droplets with a bad match and droplets enclosed by others are deleted.

Small Droplets To find the centers of small droplets (9-30 pixels), small dark regions in the image are detected by applying different gray value thresholds and searching for intensity minima. Then the distance of the droplet centers to the background (unwetted substrate) is taken as an estimate for the droplet radius. Finally the gradient based match is optimized and artifacts are sorted out.

Very Small Droplets Prior to finding very small droplets (7-18 pixels), afore detected droplets are removed. By thresholding the image, the background is obtained. The background consists of unwetted substrate and removed droplets. Small dark regions in the image (potential centers of very small droplets) are excluded from the background. Then a short pass filter is applied to the preprocessed image to enhance the contrast between the reflection ring and the central region of very small droplets. Extended minima in the filtered image contain potential droplet center regions. From these regions, the background determined before is subtracted. The remaining center regions are taken for droplet centers and the distance to the background is the corresponding droplet radius. Droplets with a bad match are excluded from the list and overlaps are removed.

Tiny Droplets Finally, tiny droplets (3-15 pixels) are detected. By thresholding the image and by thresholding a short pass filtered image a background image is calculated. Then an iterative procedure is used up to three times to detect tiny droplets.

For each pixel, the distance to the background is calculated. Local maxima in the distance are the candidates for droplet centers with the distance being the radius. Now radius and position are varied to optimize the profile based match and droplets with a bad match are deleted. Then the radius is determined by optimizing the gradient based match. Again droplets with a bad match or a high number of apparent overlaps are deleted. Finally the detected tiny droplets are added to the background.

This procedure is repeated up to three times. A big portion of tiny droplets can be found this way. To find the residual tiny droplets, the image (with covered droplets) is segmented with the watershed transformation [55, pp. 417]. For circular regions, the area and the centroid are used to define droplet radius and position. The droplets are added to the background.

As a last attempt to find tiny droplets, the image is again segmented by the watershed transformation and found droplets are covered. Centers of the segmented regions are then used as starting points for the droplet search by the iterative procedure described above. Finally, the results are combined and copies and enclosed droplets are deleted.

2.4.2.3 Removing artifacts

In the first steps of droplet detection, many features are erroneous potential droplet candidates. On the one hand, there are interruptions of reflectance rings. On the other hand, droplets which are partly outside the image are difficult to detect. Additionally, when droplets are densely packed, dark gaps surrounded by several small droplets can easily be mistaken for droplet centers. Finally, the identification of potential droplet centers relies on thresholding. As the result is sensitive to the exact values of the threshold (±3 on a scale 0 to 255 can make quite a difference!) problems arise when the illumination is changing between measurements. For this variety of reasons, a bunch of criteria is used to subsequently remove artifacts from the list of detected droplets. For being able to find almost all droplets, the criteria to detect potential droplet centers are rather relaxed. Therefore, also the criteria to sort out artifacts should not be too strict. Said this, the number of unidentified artifacts should be small to get reliable results for the droplet distribution. Thus a careful combination of criteria has to be applied for identifying as many artifacts as possible without affecting the detection of real physical droplets.

Droplet Radius Each subroutine is optimized for a certain range of droplet radii. All droplet detections outside this range are therefore deleted. The ranges of the droplet detection subroutines have significant overlap to ensure all droplets are covered.

Edge Distance Droplets with a significant fraction outside the image cannot be detected safely by the standard routines and are therefore deleted. As described above, a specific subroutine is implemented to detect edge droplets which are only partially visible inside of the image.

Match to Image The main purpose of defining the match functions in section 2.A.4 is to use them as a criterion to distinguish valid droplet detections from artifacts. The profile based match function (2.110) compares the expected sequence of dark an bright rings with the image and does a good job in revealing detections which cover several smaller physical droplets. The gradient based match (2.107) sorts out false droplet detections in free spaces between physical droplets.

Enclosed Droplets Due to condensation of water vapor the droplets grow continuously. If the sum of the coalescence radii r_c of two neighboring droplets exceed the distance of their centers, they immediately coalesce and relax to a spherical droplet shape within seconds (or less for small droplets). Hence the detection of two severely overlapping droplets can be regarded as an artifact. Often parts of the reflection rings are detected as small droplets. If small droplets are detected on an area where a big droplet was found, they are deleted.

Multiple Detections To ensure that (almost) all droplets are detected, often several routines are applied subsequently which are able to detect the same droplet. A copy finder algorithm detects multiple representations of the same droplet in the droplet list and replaces them by one instance with the mean value of the representations.

Reduction of Apparent Overlaps Starting point for the droplet detection is usually the dark central region of droplets. Quite often, however, regions between several adjacent droplets are erroneously detected as droplet centers. This results in a huge number of apparent droplet overlaps. To distinguish between real droplets and artifacts, two criteria are used. Firstly, droplets which overlap with other droplets are likely to be artifacts. Secondly, real droplets in general have a better match than artifacts. By subsequent application of these criteria, artifacts can be removed successfully in a number of steps.

2.4.3 Summary

In this section, we mainly summarize the detection algorithm for the high resolution images. For big droplets, two reflection rings can be seen. Inside the inner reflection ring, the droplet images show a dark core, also between the reflection rings and outside the outer ring the image is relatively dark. The size of these alternating dark and bright regions, as well as their mean intensity and the intensity variation is parametrized.
The backbone of the actual droplet detection algorithm are two match functions (see appendix 2.A.4). With the first match function, the detection of droplets is compared

to the image and the match between the outer reflection ring and the area around it. The second match function is more involved, it compares the image to the parametrized intensity of the sequence of dark and black regions in the droplet image.
The detection of droplet operates in four steps:

1. Preprocessing of the image with deblurring and smoothing.
2. Detection of potential droplet positions and rough estimate of the droplet radius.
3. Variation of droplet radii and positions to optimize the match to the image.
4. Exclude false droplet detections from the list of droplets.

To detect the large range of droplet radii in the high magnification images (3-3000 pixels), six different subroutines are optimized each to detect a subrange of droplet radii. A seventh subroutine is implemented to find droplets which are only partially visible on the image. For processing low resolution images, only two subroutines are necessary. In this case, the algorithm only follows the steps 1, 2 and 4 described above. The detection in the low resolution data works so reliably that coalescence and dripping events can be characterized by comparing the lists of detected droplets of subsequent frames (see section 2.5.3.4 and figure 2.26).
Having invested so much effort into the detection of the droplets in the images, we are very excited about the results that we can get from this procedure.

2.5 Evolution of the Droplet Size Distribution

In this section our results for the evolution of the droplet size distribution of breath figures are presented. We detect droplet radii using the image processing described above (section 2.4). To compare it to the theoretical description of Family and Meakin [45, 46], radii are converted into sizes (i.e. volumes) using (2.2). We assume a droplet shape of a hemisphere (compare figure 2.10) for the droplets detected in the high resolution images. For the droplets in the low resolution images, we cannot be sure about the droplet shape, because the droplets with radii exceeding 20% of the capillary length (see section 2.2.1. Therefore the data for these measurements is given in radii.

The present study of breath figures was undertaken in close collaboration with Blaschke, who set up molecular dynamics type simulations of breath figures [23]. We compare our experimental results to the numerical data and observe where the physics present in the experiment is extending the physical mechanisms modelled in the simulation. We therefore give a short account over the assumptions used implicitly in the setup of the numerical simulations. For details of the algorithm the reader is referred to the Master Thesis of Blaschke [23]. In the numerical simulations, volume flux on the substrate is modelled by a "rain" of monomers of size $s_0 = 1$ onto the substrate. The monomer is put on the substrate at a random position. In case it hits a free part of the substrate, a droplet of size s_0 is nucleated at that position. In case it overlaps with any other droplet, the two coalesce and form a bigger droplet conserving volume and the center of mass. Subsequently, overlap of droplets leads to coalescences, until there are no droplet overlaps in the system. Then the next monomer "rains" onto the substrate and the step is produced. Periodic boundary conditions are used. The simulations are stopped at the latest when the diameter of the biggest droplets reaches 10% of the box length. For the simulations of the steady-state distribution, droplets larger than a critical radius are removed from the substrate. The effect of gravity is thus modeled just by dripping, the distortion of the shape is neglected.

Having summarized the setting that we use to obtain our experimental and the numerical data, we give an outline of the results presented in this chapter. In the first section 2.5.1 the self-similar droplet size distribution of regime (iii) (confer section 2.2.2.3) observed in the experiment and in numerical simulations of Blaschke [23] are studied. In the second section 2.5.2 the steady-state size distribution (regime (iv), confer section 2.2.2.4) is analyzed, which develops in the presence of an upper limit for the droplet radius. In the third section 2.5.3, the coalescence kernel for pairwise droplet coalescences is inferred from the pair correlation of the droplet distribution in the experimental and the numerical data. Following several steps, we are able to analyze and finally to parametrize the different contributions to the coalescence kernel. In the final section 2.5.4, the Smoluchowski equation (confer section 2.2.4) is extended by terms accounting for intrinsic droplet growth, nucleation and dripping. The equation is integrated in time numerically and the result is compared to the observed distributions.

2.5.1 Self-Similar Size Distribution

2.5.1.1 Reference length and time scale

The self-similar droplet size distribution was introduced as regime (iii) in section 2.2.2.3. To compare the experimental data to the numerical data, it is desireable to introduce dimensionless quantities. Therefore a reference length scale r_0 for the droplet radius and a time scale t_0 has to be defined. The numerical simulations of Blaschke are constructed using a smallest droplet radius r_0, which corresponds to the smallest droplet size s_0. We are interested in the time scale at which on average one monomer of size s_0 has been deposited on its wetted area πr_0^2. Thus the time scale t_0 is related to the volume flux F on the substrate

$$Ft_0 \equiv \frac{s_0}{\pi r_0^2} = \frac{cr_0}{\pi}. \tag{2.31}$$

Equation (2.31) can be interpreted as the definition equation for t_0. The time scale t_0 is proportional to the smallest scale r_0 resolved in the simulations

$$t_0 = \frac{cr_0}{F\pi}. \tag{2.32}$$

The choice of a suitable reference length scale r_0 is not obvious for the experimental setting. By comparison of numerical and experimental data, we will later be able to estimate the radius r_0 for the experiment. For the comparison to the numerical data, the dimensionless time $\tau \equiv t/t_0$ was used [23].

2.5.1.2 Growth Rate of the Characteristic Droplet Size

The investigation is started by looking at the evolution of the characteristic droplet radius. It is computed by dividing the sixth moment of the droplet radius distribution by the fifth moment

$$R \equiv \frac{\int_0^\infty n(r) r^6 \mathrm{d}r}{\int_0^\infty n(r) r^5 \mathrm{d}r} \tag{2.33}$$

where $n(r)\mathrm{d}r$ is the number of droplets of a radius in the interval $[rr + \mathrm{d}r]$ per unit area. Figure 2.13(a) shows the evolution of the radius R of the biggest droplets for a typical measurement. We find that the radius R grows linear in time. This is in line with the prediction $cR^3 = S \sim t^3$ of Family and Meakin (confer section 2.2.2.3).

Also the total droplet volume per unit area in the system increases linearly in time (see figure 2.13(b)). The volume $V(t)$ that has been deposited on the area wetted by a big droplet with radius $R(t)$ is determined by

$$V(t) = Ft\pi R(t)^2. \tag{2.34}$$

However, this is not the volume of the biggest droplets. Growing droplets coalesce with

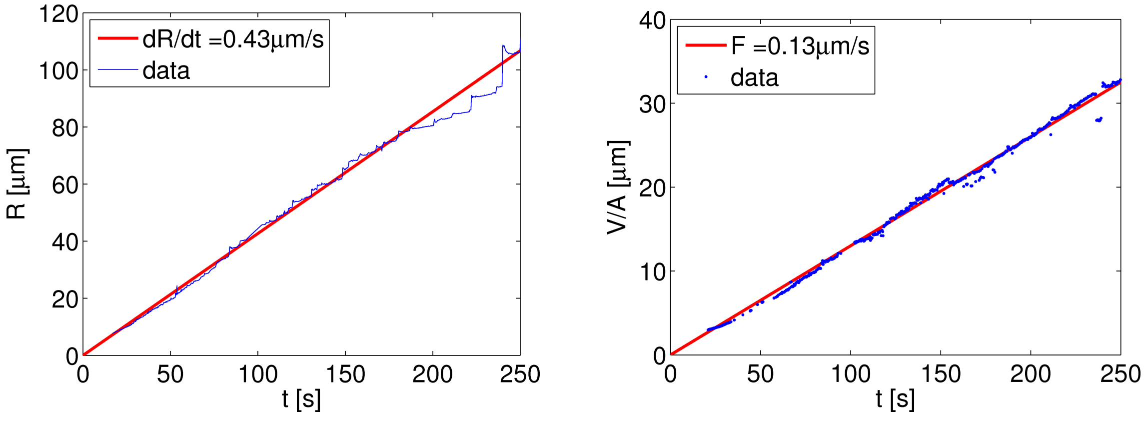

(a) (b)

Figure 2.13: Left: Radius of the biggest droplet as a function of time. It grows linear in time with the rate $\dot{R} = 0.43\mu$m/s. The steps in the radius are due to the coalescences of the biggest droplets in the system.
Right: The droplet volume per unit area increases with the rate $F = 0.13\mu$m/s.

their neighbors. Therefore there is an additional volume flux towards the biggest droplets. They gather the volume S deposited on an area which is bigger than their wetted substrate area by a gain factor γ

$$S = cR^3 \equiv \gamma Ft\pi R^2. \tag{2.35}$$

Dividing by R^2 and taking the time derivative gives

$$c\dot{R} = \gamma\pi F. \tag{2.36}$$

Hence we can calculate the gain factor γ from the measured growth rate of the biggest radii and the volume flux on the substrate

$$\gamma = \frac{\dot{R}c}{F\pi}. \tag{2.37}$$

Alternatively, it can be interpreted as the ratio between the growth rate of the characteristic droplet radius $\dot{R}$ and the individual growth rate $\dot{r}$. For the experiment, we find $\gamma = 2.11 \pm 0.03$, while in the numerical simulations we find a somewhat smaller value, $\gamma = 1.714 \pm 0.002$. Can we understand where this factor of about 2 is coming from?

Beysens and coworkers [17, 51] observed that the wetted fraction in the intermediate time regime (ii) reaches a saturation value of about 55% (see section 2.2.2 for the definition of regimes). Considering equation (2.35) and keeping in mind that the flux on the *whole* substrate leads to the growth of droplets with radii $r \approx R$ that wet only 55% of the substrate, the gain factor γ can be expected to be

$$\gamma = \frac{1}{w(r \approx R)} \approx \frac{1}{0.55} = 1.8\,. \tag{2.38}$$

In this case, the scaling argument of Family and Meakin [46] (2.25) for a constant wetted fraction works and the size distribution is indeed described well by equation (2.19) with $\theta = 5/3$. Rescaling of the size distribution in regime (iii) according to (2.19) works perfectly for the "bump" in the size distribution, as we will show in section 2.5.1.7. This implies that the "bump" in the size distribution of regime (iii) is nothing but a continuation of the distribution forming in regime (ii). Hence the "bump" droplets still occupy about 55% of the substrate and the argument above leading to (2.38) is also valid for regime (iii). The difference in the values obtained for γ in the experiment and in the numerics is probably associated with the slightly different form of the "bump" in the experimental and numeric droplet size distributions, respectively (compare figure 2.15).

2.5.1.3 Comparing Breath Figures to Fractal Packings

In section 2.2.2.3 the scaling analysis of the droplet size distribution with the approach

$$n(s,t) = s^{-\theta} f\left(\frac{s}{S(t)}\right) \tag{2.39}$$

with $\theta = 5/3$ by Family and Meakin [46] was discussed. We pointed out that it is essential to include the physics of the smallest droplets into the analysis of the size distribution. We aim to get an expression for the shape of $f(s/S)$ for $s \ll S$. To get an idea for the behavior of $f(x)$ we look at the way the droplets are "packed" together. To that end, we regard breath figures as a natural example for a fractal packing (confer section 2.2.3) and find an alternative way for the calculation of the wetted fraction. We use $R = (S/c)^{1/3}$ as our unit length scale. Hence the scale of the of the smallest droplets decreases in time like $s_0/S(\tau)$ in this unit.

We consider the volume $V(s^*)$ of all the droplets on an area R^2 smaller than some size $s^* \ll S$

$$V(s^*) = \left(\frac{S}{c}\right)^{2/3} \int_0^{s^*} n(s,t) s \,\mathrm{d}s. \tag{2.40}$$

Within the time dt the volume of these droplets increases to

$$V(s^* + \dot{s}\mathrm{dt}) = \left(\frac{\mathrm{S}}{\mathrm{c}}\right)^{2/3} \int_0^{\mathrm{s}^*+\dot{\mathrm{s}}\mathrm{dt}} \mathrm{n(s,t)s\,ds}. \tag{2.41}$$

Hence the growth in volume of these droplets amounts to

$$\mathit{\Delta} V = \left(\frac{S}{c}\right)^{2/3} n(s^*,t) s^* \, \dot{s} \mathrm{d}t. \tag{2.42}$$

Considering the droplet distribution as a fractal packing, the area $A(s^*)$ covered by the droplets smaller than s^* amounts to

$$A(s^*) = \left(\frac{S}{s^*}\right)^{d_f/3} \left(\frac{s^*}{c}\right)^{2/3}. \tag{2.43}$$

The volume $\mathit{\Delta} V$ deposited on the area $A(s^*)$ within the time $\mathrm{d}t$ is then

$$\mathit{\Delta} V = \left(\frac{S}{s^*}\right)^{d_f/3} \left(\frac{s^*}{c}\right)^{2/3} F \mathrm{d}t. \tag{2.44}$$

Comparing (2.42) and (2.44) yields an expression for the droplet size distributions for $s^* \ll S$

$$n(s^*,t) = \frac{F}{\dot{s}} \cdot \frac{1}{s^*} \cdot \left(\frac{S}{s^*}\right)^{\frac{d_f - 2}{3}}. \tag{2.45}$$

2.5.1.4 Growth Rate of Smallest Droplets

As we discussed in section 2.5.1.2, the radius of big droplets grows on average linear in time, hence

$$\dot{s} \sim F s^{2/3}. \tag{2.46}$$

For droplets smaller than some size s_1 however, the growth rate may be different.

Experimental Setting In section 2.2.2.1 we presented two types of droplet growth that have been observed in experiments. Our experimental data is consistent with the assumption (as we will show later with figure 2.16(a)), that the growth of small droplets $r \sim t^{1/4}$ is limited by diffusion (type I growth), leading to a growth law

$$\dot{s} \sim F s^{-1/3}. \tag{2.47}$$

Hence the full equation for the droplet growth rate is the sum of (2.46) and (2.47), yielding

$$\dot{s} \sim F s^{2/3} \left(1 + \frac{s_1}{s}\right). \tag{2.48}$$

At the size s_1 the growth law changes from (2.46) to (2.47). Later, in section 2.5.1.8, we will use it as a fit parameter to rescale our data for the droplet size distribution. The growth law (2.48) is inserted into (2.45) yielding an expression for the lower cutoff of the droplet size distribution

$$n(s) \sim \frac{1}{1+\frac{s_1}{s}} s^{-5/3} \left(\frac{S}{s}\right)^{\frac{d_f-2}{3}} . \tag{2.49}$$

Numerical Setting In the numerical simulations of Blaschke [23] the growth of the smallest droplets can be approximated by

$$\dot{s} \sim F \left(s^{1/3} + s_1^{1/3}\right)^2 = F s^{2/3} \left(1 + \left(\frac{s_1}{s}\right)^{1/3}\right)^2 . \tag{2.50}$$

Each droplet gathers the volume flux on a substrate area that is slightly bigger than the area it wets. The flux on a ring with a width of about $s_1^{1/3}$ contributes to the droplet growth. Big droplets, however, are surrounded by a dense packing of smaller droplets and the effective width of the ring goes to zero with increasing droplet size. As for the experimental setting before, the growth law (2.50) is inserted into (2.45) yielding

$$n(s) \sim \frac{1}{\left(1+\left(\frac{s_1}{s}\right)^{1/3}\right)^2} s^{-5/3} \left(\frac{S}{s}\right)^{\frac{d_f-2}{3}} . \tag{2.51}$$

Note that the model for the growth rate of small droplets in the *numerical* data is preliminary and still a matter of ongoing work.

2.5.1.5 Total Droplet Volume

In the following, we check the applicability of the predictions for the tail of the droplet size distribution in the experiment and in the numerics. We start with a consistency check for the total droplet volume. In section 2.2.2.3 it was pointed out that the lower end of the size distribution has to fulfill the condition

$$sn(s) \to 0 \text{ for } s \to 0 \tag{2.52}$$

in order to get a finite volume per area of the full droplet size distribution. The fractal dimension of a packing is always smaller than the embedding dimension $d_f < 2$. Therefore (2.52) is fulfilled for both the experimental (2.49) and the numerical (2.51) expression for the size distribution.

2.5.1.6 Decreasing Porosity

The fraction of the substrate wetted by droplets cannot be expected to be constant in regime (iii) (confer section 2.2.2.3). We investigate the evolution of the wetted fraction in order to determine the fractal dimension of breath figures. The fraction of the substrate that is wetted by droplets smaller than s_1 may be neglected. We therefore focus on the scaling part of the size distribution

$$n(s,t) \sim s^{-5/3} \left(\frac{S(t)}{s}\right)^{\frac{d_f-2}{3}} . \tag{2.53}$$

By definition, the surface is covered by a fractal packing completely, when the size of the smallest particles approaches zero. Hence for the porosity $p(t) \equiv 1-w(t)$, the area fraction *not* covered by droplets, we can write

$$\begin{aligned} t^{-\sigma} \sim p(\tau) &= 1-w \sim \int_0^{s^*} s^{2/3} n(s,t)\mathrm{d}s \\ &\sim \int_0^{s^*} s^{2/3} s^{-5/3} \left(\frac{S(t)}{s}\right)^{\frac{d_f-2}{3}} \mathrm{d}s \\ &\sim S(t)^{\frac{d_f-2}{3}} \int_0^{s^*} s^{\frac{d_f-2}{3}-1} \mathrm{d}s \\ &\sim S(t)^{\frac{d_f-2}{3}} s^{*\frac{d_f-2}{3}} . \end{aligned} \tag{2.54}$$

Comparing this result to the scaling of the size of the biggest droplets $S \sim t^3$ (2.25), we find a scaling relation for the porosity exponent σ

$$\sigma = 2 - d_f . \tag{2.55}$$

This result means that from the time evolution of the porosity the fractial dimension of the packing can be determined. In figure 2.14, we show how porosity decreases in time. To improve statistics, five measurements are analyzed and averaged subsequently. For all measurements, the heating power and the top plate temperature is the same, however different volume fluxes are observed. This is due to the fact that the volume flux on the substrate is not perfectly homogeneous and the measurements at the small scales are taken at different positions of the substrate. To average over several measurements, it is therefore essential to introduce a time scale indirectly proportional to the volume flux on the substrate.

In the experiment, a decay of the porosity in time can be observed finding an exponent $\sigma = 0.16 \pm 0.01$ In the numerics, however, a different slope is found $\sigma = -0.30 \pm 0.01$. The origin of the difference will be discussed in section 2.6.

2.5.1.7 Scaling of the Droplet Size Distribution

Equation (2.55) implies that the breath figures in the experiment have a fractal dimension of $d_f = 1.84$. For the numerically simulated breath figures we find a slightly smaller fractal dimension $d_f = 1.70$. Comparing (2.39) to (2.53) we predict that the tail of $f(s/S)$

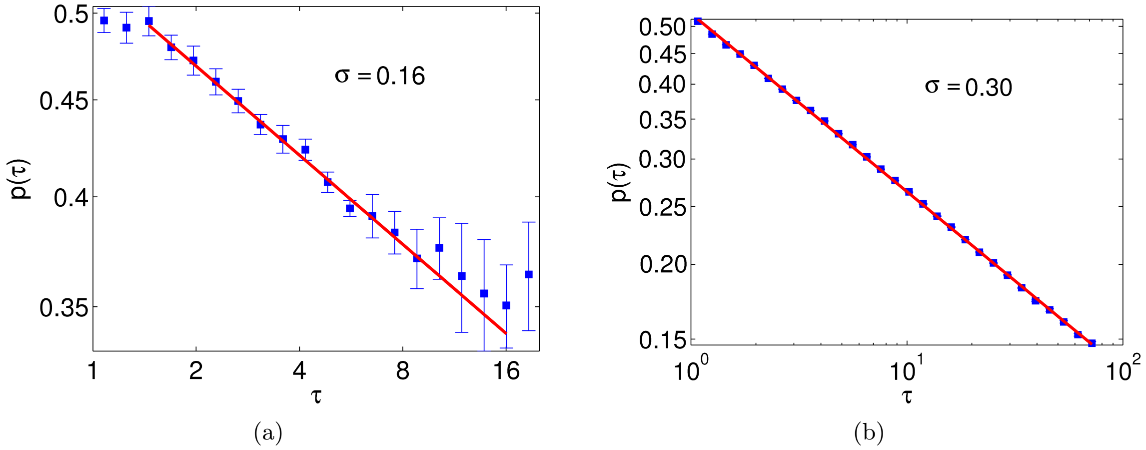

(a) (b)

Figure 2.14: The free fraction of the substrate p decays with a power law $p \sim \tau^{-\sigma}$. In the experiment (left), a decay of the porosity in time can be observed with an exponent $\sigma = 0.16 \pm 0.01$. In the numerics (right), however, a decay of the porosity with $\sigma = 0.30 \pm 0.01$ is observed. To compare the experimental to the numerical data, time is expressed in units of t_0 (2.32).

scales with $(s/S)^{-0.10}$ for the numerical data. This is indeed very close to the scaling correction $(s/S)^{-0.13}$ observed in the simulations of Family and Meakin [46] (confer figure 2.7). It also fits well to the scaling of the droplet size distribution simulated by Blaschke (figure 2.15(b)). In figure 2.15(a) we show the experimental data for the droplet radius distribution in regime (iii). It is consistent with an exponent -0.05 ± 0.05. However, the error in the experimental data is too big to judge the exact value of the scaling with size.

2.5.1.8 Lower Cutoff for the Self-Similar Regime

In sections 2.5.1.3 and 2.5.1.4 we derived equations for the tail of the droplet size distribution. To compare the predictions to the measured droplet size distribution, we rescale the distribution accordingly. To test (2.49), we rescale the distribution by $(1 + \frac{s_1}{s}) s^{5/3} \left(\frac{s}{S}\right)^{0.05}$. The crossover size s_1 is used as a fit parameter. In figure 2.16(a), the rescaled distribution is shown. The tail of the distribution is flat, in agreement with our prediction (2.49). The best fit of the data we find for $s_1 = 1.5 \cdot 10^3 \mu\text{m}^3$ ($r_1 = 9\mu$m).

The numerical droplet size distribution is rescaled by $\left(1 + \left(\frac{s_1}{s}\right)^{1/3}\right)^2 s^{5/3} \left(\frac{s}{S}\right)^{0.10}$ following (2.51), again using s_1 as a fit parameter. The rescaled distribution is shown in figure 2.16(b). Again we observe a flat tail in agreement with our prediction (2.51) for $s_1 = 0.1$ ($r_1 = 1/3$). Note, that the scaling of the lower cutoff in the *numerical* data is preliminary.

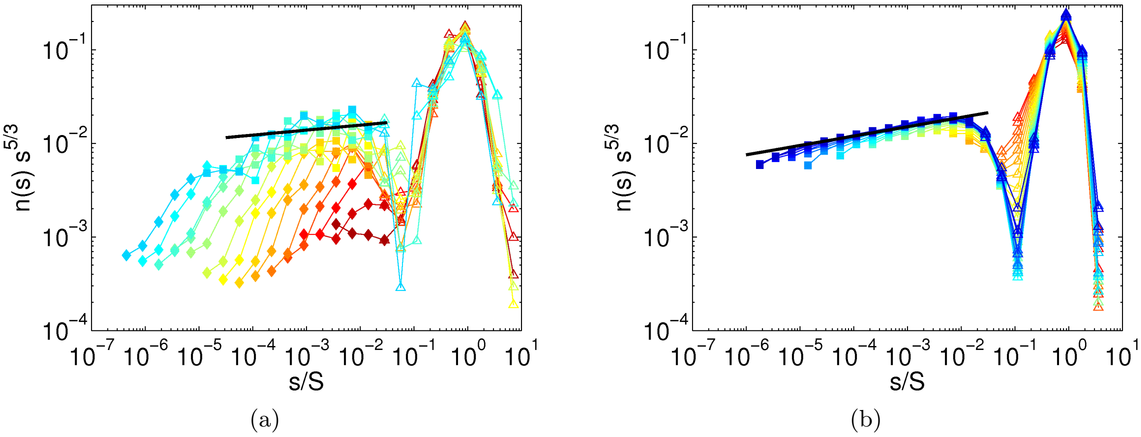

Figure 2.15: The droplet size distribution is calculated from experimental (a) and numerical (b) data. It is rescaled by the exponent $\theta = 5/3$ following (2.39), the droplet sizes are normalized by the size S of the biggest droplets. The "bump" is found in the evolving size distribution, originating from the first generation of droplets. The gap separating the bump from the tail comes from the time delay between first (regime (i)) and secondary (regime (iii)) nucleation. A scaling regime (filled squares) is easily seen in the numerical data (a), in the experimental data (b) it just starts to develop. The scaling is consistent with the prediction of the fractal dimension based on the porosity decay. The black line indicates a scaling exponent -0.05 for the experimental data and -0.10 for the numerical data. In the experimental data, a transition in the distribution is observed for droplets with $r \approx r_1 = 9\mu$m. The color encodes different times τ distributed logarithmically from 1.1 to 20.9 for the experimental data and from 1.1 to 83.5 for the numerical data.

2.5.2 Steady-State Droplet Size Distribution

In the previous section, we described the coarsening of the self-similar droplet size distribution in regime (iii). Of course, the mean droplet size cannot grow indefinitely in a physical experiment. Once, the radii of the largest droplets reach about 20% of the capillary length (equation 2.4), gravity cannot be neglected and the droplet shape is distorted (confer section 2.2.1). After about two hours (for typical heating rates) the radii almost reach the capillary length ($0.87 l_c$) and the droplets drip off. In the study of the steady-state droplet size distribution, all length scales are expressed in terms of the capillary length. For the analysis of the steady-state distribution in this section and in the following we refer to radii rather than sizes, because the actual size of droplets with $r \gtrsim 0.2 l_c$ is not known.

In figure 2.17(a) we show the experimental data for the steady-state droplet radius distribution. We find a scaling of the droplet radius distribution

$$n(r) \sim r^{-\theta_r} \tag{2.56}$$

consistent with $\theta_r = 3.0 \pm 0.1$, which is different to our prediction $\theta_r = d_f + 1 = 2.84$.

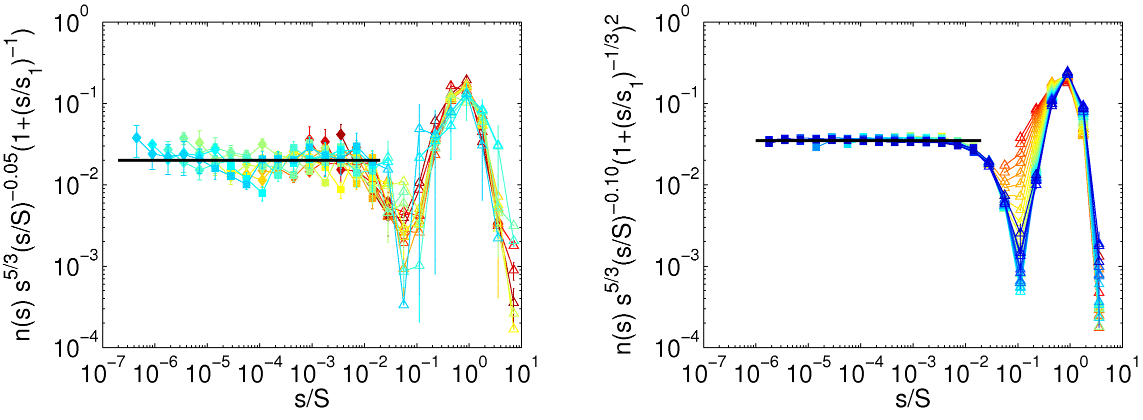

(a)

(b)

Figure 2.16: The droplet size distribution is calculated from experimental (a) and numerical (b) data. The experimental data is rescaled according to our prediction (2.49), and the numerical data is rescaled according to (2.51). In both cases, we find flat tails, i.e. excellent agreement of the data with the predicted scaling. For the experimental data, we get the best fit with $s_1 = 1.5\mu\mathrm{m}^3$ ($r_1 = 9\mu\mathrm{m}$), for the numerical data we find $s_1 = 0.1$ ($r_1 = 1/3$). The color encodes different times τ distributed logarithmically from 1.1 to 20.9 for the experimental data and from 1.1 to 83.5 for the numerical data.

However, one may expect the exponent $\theta_r = 3.0$ from the scaling argument of Family and Meakin [46], presented in section 2.2.2.3, since the wetted fraction *is* constant in the steady-state regime.

For the range of droplet radii from $0.2 l_c < r < l_c$ we find a second scaling regime with a different scaling exponent. In this radius range, the shape of the droplets deviates significantly from a spherical cap. This has also been observed for droplets on vertical substrates [104]. We find a sharp cutoff in the radius distribution at $r_c = 0.87 l_c$. Blaschke also performed simulations where droplets bigger than a certain size are taken from the system [23]. To compare the numerical to the experimental results, we express the numerical data on a length scale such that the droplets drip off at the same radius $r_c = 0.87$. The radius distribution for the numerical data is shown in figure 2.17(b). The numerical data is consistent with a scaling exponent $\theta_r = 2.70 \pm 0.1$. However, due to the fact, that the range of sizes in the simulations is very restricted, the scaling regime is very small.

2.5.3 Coalescence Kernel

In the previous section we showed that a modified scaling analysis of the droplet size distribution is suitable for describing the droplet size distribution of breath figures. A second approach to describe the evolution of the droplet size distribution is to study a

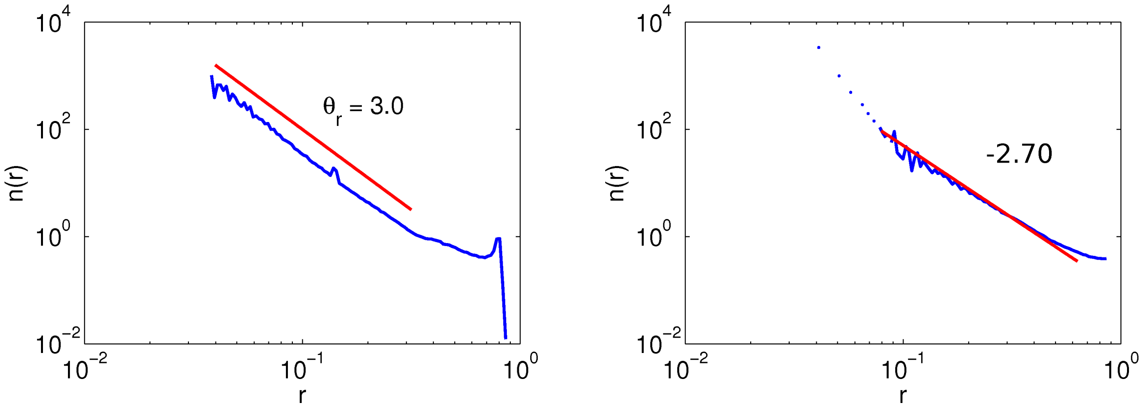

(a) (b)

Figure 2.17: Steady-state droplet radius distribution in experimental (a) and numerical data (b). The radius r is determined from images as shown in section 2.4.
(a) The number of drops of radius r per area $n(r)$ is given in units of the capillary length (2.4). For $r \lesssim 0.2 l_c$ the radius distribution scales with $r^{-3.0\pm0.1}$. This is slightly different to the scaling predicted with the fractal dimension $r^{-2.84}$. For $0.2 l_c < r < 0.87 l_c$ a different scaling is observed.
(b) For the numerical data, the length scale is chosen such that the droplets drip off at $r = 0.87$. The radius distribution is consistent with a scaling of the form $r^{-2.70}$, however due to the limited range of radii that could be simulated the scaling regime is very small.

Smoluchowski type kinetic equation, which was introduced in section 2.2.4. In order to apply the Smoluchowski equation, the coalescence kernel κ (2.30) for pairwise coalescences has to be known. In many cases of coarsening phenomena, the size dependence of the coalescence probability of particles cannot be measured. It must be estimated from theory. One example is gravitational collection, that will be discussed in section 3.6.2.3.

For breath figures however, we are able to infer the coalescence probability from the pair correlation of neighboring droplets. To that end, we measure the probability of finding a droplet of radius r within a distance l of a droplet with radius r' (section 2.5.3.1). In section 2.5.3.2 we find that the coalescence kernel scales with the sum of the radii $r + r'$. However, we find an increased coalescence probability for droplets of similar size (section 2.5.3.3) compared to the relation (2.29) given by [95] for uncorrelated droplet distributions. This can be understood by seeing the steady-state distribution (iv) as a superposition of self-similar distributions (iii). To this end, we analyze the distribution of droplet ages in section 2.5.3.4. Altogether, this allows us to derive the form of the coalescence kernel (section 2.5.3.5).

2.5.3.1 Pair Correlation

By condensation, each droplet grows on average with the rate $\dot{r}$.When two droplets overlap, they coalesce and form a bigger droplet. The volume is conserved, i.e. $r_{new} = \left(r^3 + r'^3\right)^{1/3}$. The coalescence rate $\Gamma(r,r')$ of droplets with radii r and r' per area is

$$\Gamma(r,r') = 2\dot{r}\kappa(r,r')n(r)n(r'). \tag{2.57}$$

To determine the coalescence kernel $\kappa(r,r')$ experimentally, we measure the number of droplet pairs per area $p(r,r',l)$ with an edge to edge distance smaller than the distance $l = 2\Delta r$ (see figure 2.18).

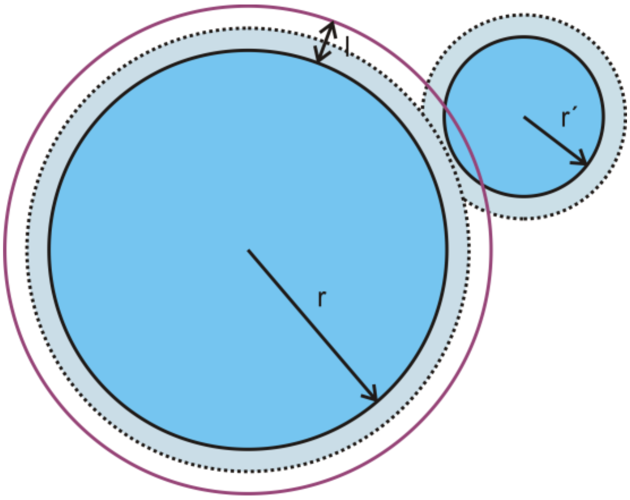

Figure 2.18: Sketch for coalescence of two droplets with radii r and r'. Within the time $\Delta t = l/2\dot{r}$ all droplets with an edge to edge distance $\leq l$ coalesce.

The droplet pair density $p(r,r',l)$ for $l = 0.25$ (in units of capillary length) is shown in figure 2.19. We find a qualitatively similar picture both for the experimental (panel (a)) and the numerical (panel (b)) data. Most of the droplet pairs involve at least one small droplet. Pairs of two big droplets are extremely rare. Surprisingly, the number of droplets pairs with similar radii seems to be relatively high. The big number of droplet pairs involving small droplets is simply due to the fact, that most of the droplets in the system are small (see figure 2.17).

The collision rate Γ is related to the droplet pair density p by

$$\frac{\partial p}{\partial l}(r,r',l=0)2\dot{r} = \Gamma(r,r') = \kappa(r,r')2\dot{r}n(r)n(r'). \tag{2.58}$$

Note that

$$p(r,r',l=0) = 0 \tag{2.59}$$

since all overlapping droplets coalesce immediately. Thus to leading order, the number of droplet pairs is proportional to l

$$p(r{,}r'{,}l) \approx l\frac{\partial p}{\partial l}(r{,}r'{,}l=0). \tag{2.60}$$

The applicability of this approximation will be checked in the next subsection. We therefore write

$$\frac{\partial p}{\partial l}(r{,}r'{,}l=0) = \frac{p(r{,}r'{,}l)}{l} = \kappa(r{,}r')n(r)n(r') \tag{2.61}$$

which leads to

$$\kappa(r{,}r') = \frac{p(r{,}r'{,}l)}{ln(r)n(r')}. \tag{2.62}$$

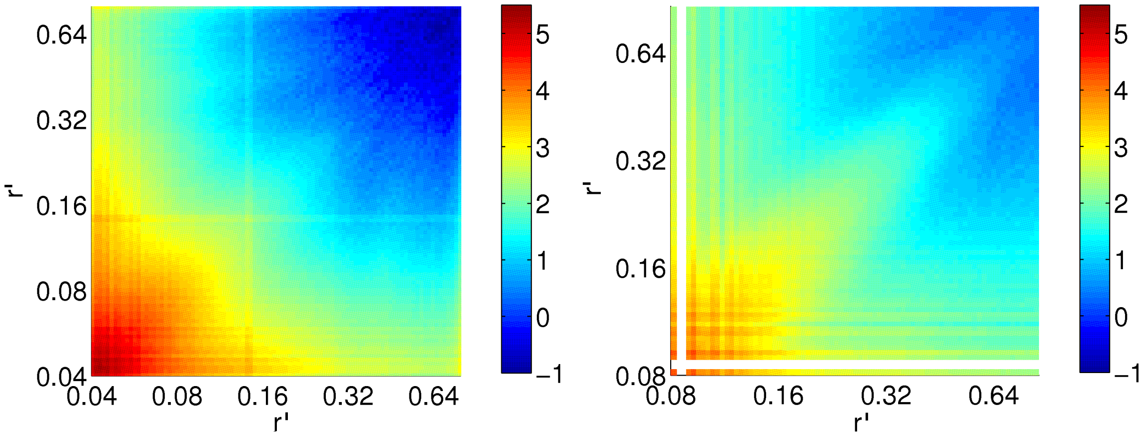

(a)

(b)

Figure 2.19: The color denotes the decadic logarithm of the number density of droplet pairs $p(r{,}r'{,}l)$ with radii r, r' per unit area l_c^2 within a distance of $l = 0.25$. Note that a ring around a droplet with width $l = 0.25$ is a large area. The number of droplet pairs in this area is $O(n^2)$. Most of the droplet pairs involve at least one small droplet. Pairs of two big droplets are extremely rare. The numerical data (right) has the same qualitative features as the experimental data (left). Quantitatively, the numerical data deviate though, what we attribute to a limited range of radii simulated in the numerics. The white line in the numerical data is a consequence of the construction of the algorithm: The droplet size takes multiple values of the monomer size s_0. The stripe in the experimental data is an artifact of the image processing, also seen in the steady-state size distribution in figure 2.17(a).

2.5.3.2 Scaling of Coalescence Kernel

The coalescence kernel κ is shown in figure (2.20). Two features of the kernel can be observed. In the first place, the kernel increases with the radii of the coalescing droplets.

In the second place, a peak on the diagonal of the kernel is prominent. This means that droplets of similar size are more likely to coalesce.

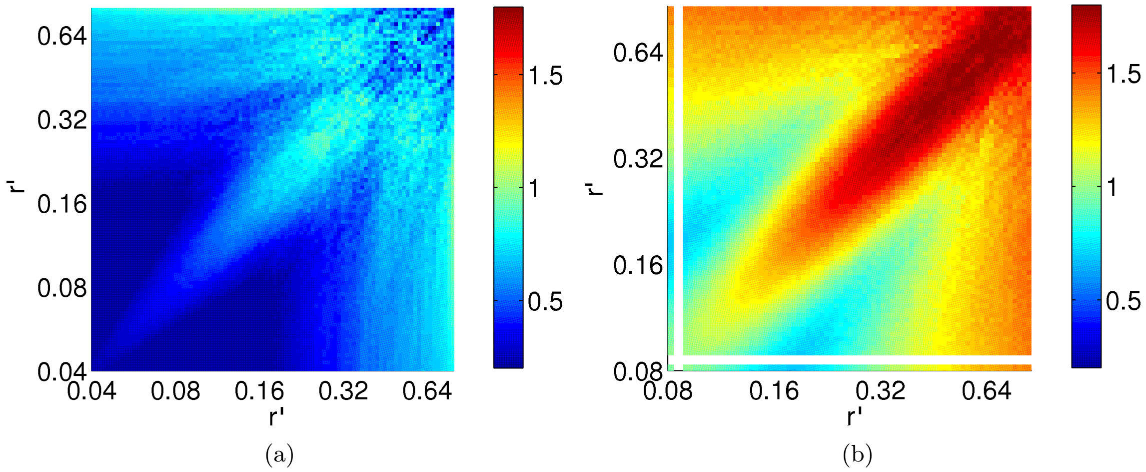

(a)

(b)

Figure 2.20: The decadic logarithm of the coalescence kernel $\kappa(r,r')$ is encoded by the color. The coalescence probability of a droplet increases with the radius. the kernel displays a peak on the diagonal: There is an increased probability that coalescing droplets are of similar size. The coalescence kernel is calculated by equation (2.62) for $l = 0.25$. Experimental data is shown on the left, the numerical data on the right.

With figure 2.18 it can be seen why the coalescence probability increases with the radius of a droplet. If a droplet grows within the time Δt by $\Delta r = \dot{r}\Delta t$, it coalesces with the droplets touching the ring with width Δr around it. The area of this ring is $A_{\text{ring}} \approx 2\pi r \Delta r$ for small Δr. However, the coalescence partner will also grow by Δr, forming a ring with the area $2\pi r' \Delta r$. The kernel is proportional to the sum of the ring areas

$$\kappa(r,r')2\dot{r} \sim 2\pi(r+r')\frac{2\Delta r}{\Delta t} \quad \text{for} \quad r \sim r'. \tag{2.63}$$

As no droplet is distinguished, the coalescence kernel has to be symmetrical in r,r'. Hence we define

$$\kappa(r,r') \equiv k(r,r') \cdot 2\pi(r+r') \tag{2.64}$$

with the proportionality factor k. For $k(r,r') \equiv 1$ this coalescence kernel is equivalent to the one guessed by Rogers et al. [95].

Family and Meakin [46] provide a scaling argument why the coalescence kernel can be expected to scale linear with the radius. To test this prediction we plot $\kappa(r,r')$ as a function of $r+r'$ (see figure 2.21(a)). Each point corresponds to one bin of droplet pairs with radii r,r' in figure 2.20. Most of the points fall on a line with slope 1. It is revealing to exclude droplet pairs with $1/3 < r/r' < 3$ from the plot (see figure 2.21(b)). Now all points are close to a curve with slope 1.

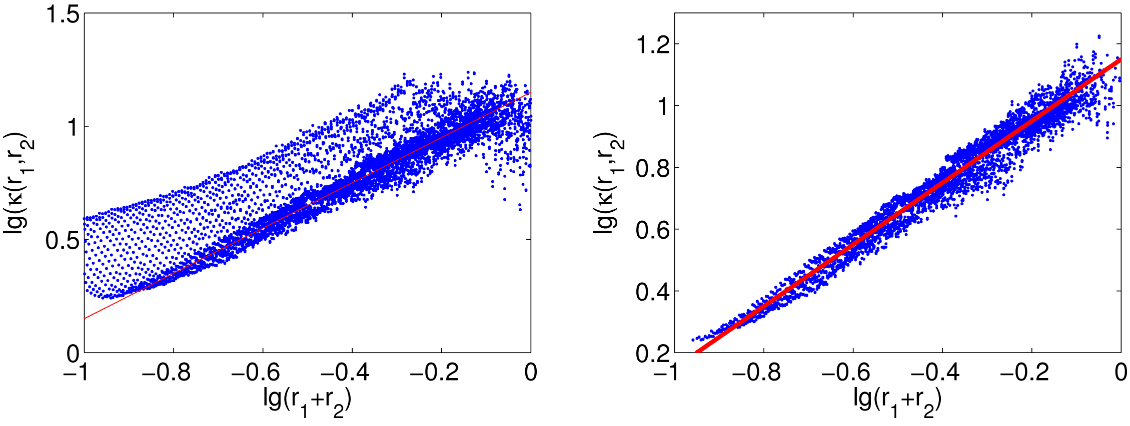

(a) (b)

Figure 2.21: Left: $\kappa(r,r')$ is proportional to $r + r'$. The solid line is a guide to the eye with slope 1. The coalescence kernel κ is calculated with equation (2.62) for the distance $l = 0.25$.
Right: The same plot for droplets with non-similar droplet radii ($1/3 \geq r/r'$ or $3 \leq r/r'$).

As a second test, we calculate the rescaled coalescence kernel k. Combining equations (2.62) and (2.64), it is given by

$$k(r,r') = \frac{p(r,r',l)}{2\pi(r + r')ln(r)n(r')}. \tag{2.65}$$

In figure 2.22, the rescaled coalescence kernel k is shown. The rescaled coalescence kernel $k(r,r')$ does not show a scaling dependence on r,r' anymore, except for the peak at the diagonal which can clearly be seen now.

We are now in the position to check the approximation (2.60). We calculate $k(r,r')$ for a range of distances l and calculate the mean

$$k_0(l) \equiv \langle k(r,r',l) \rangle_{r/r'<1/3\,,\,r/r'>3} \tag{2.66}$$

of all points with $r/r' < 1/3$ or $r/r' > 3$. Figure 2.23 shows that k_0 is roughly constant for a range of distances l. For very small droplet distances, the statistics gets bad. For large distances, equation (2.60) does not hold anymore. We find $k_0 = 1.1 \pm 0.1$ in agreement with Rogers et al [95].

The proportionality factor k_0 is determined by the condition that for a steady size distribution, the released area by coalescence and dripping has to balance the increase in wetted area due to condensation and nucleation. Note that k is intrinsically dimensionless. In

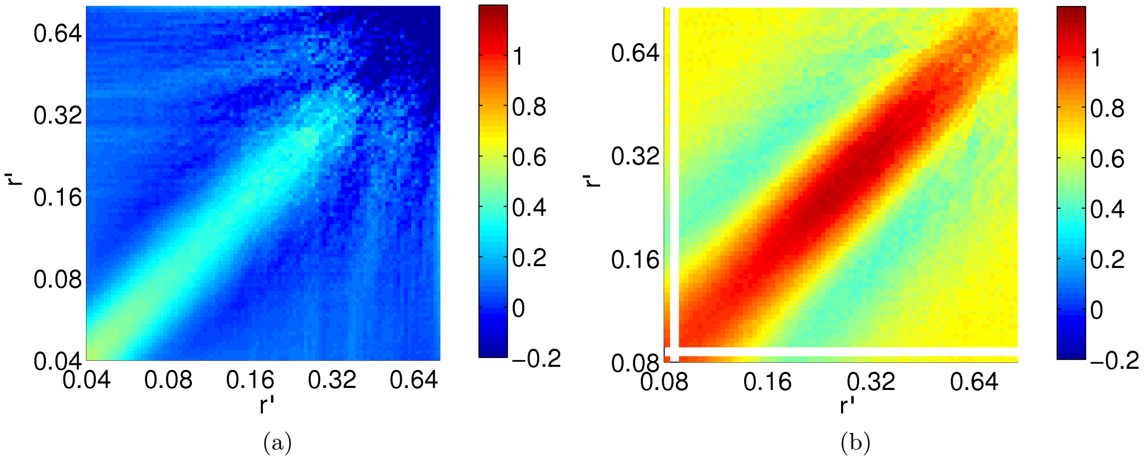

(a) (b)

Figure 2.22: The coalescence kernel is divided by the sum of the radii. The rescaled coalescence kernel $k(r,r')$ equation (2.65) does not show any scaling dependence on r,r' anymore. However, the peak at the diagonal can clearly be seen. For very big droplets, the rescaled coalescence kernel is smaller in the experimental data. This may be an effect of dripping and of the droplet distortion due to gravity. Experimental data is shown on the left, the numerical data on the right, $l = 0.25$.

particular, it does not depend on the choice of the length scale.

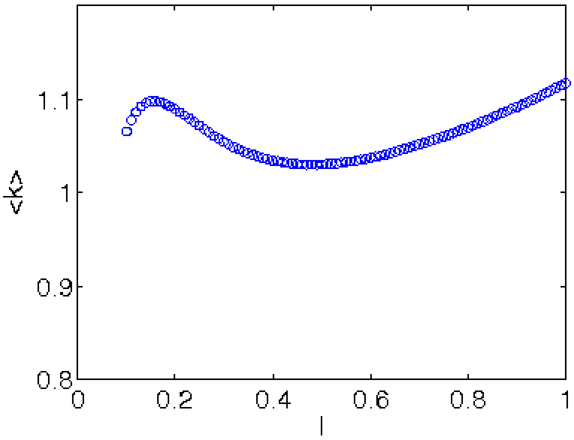

Figure 2.23: The mean value of the rescaled coalescence kernel k (away from the diagonal) is plotted as a function of the distance l. The value of k does not depend much on the distance l (beware the scale of the abscissa!). This observation justifies the usage of the approximation (2.60).

2.5.3.3 Peak on Diagonal

The diagonal values of the rescaled coalescence kernel $k_1(r) \equiv k(r,r)$ exhibit only a minor dependence on r for $r \lesssim 0.2 l_c$. For big droplets, where the effect of gravity and dripping cannot be neglected, the coalescence kernel decreases. For the droplet radii in the scaling regime, we find $k_1(r) \approx 2.3 \pm 0.2$ for the experimental data.

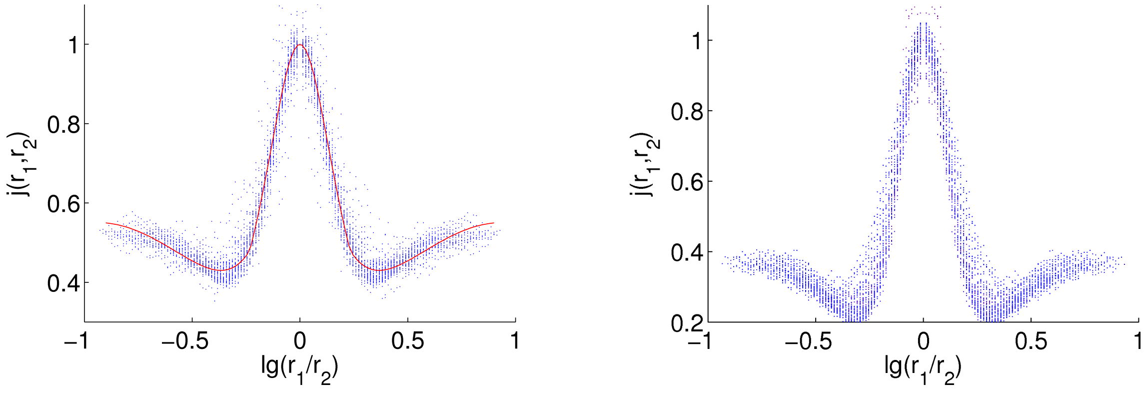

(a) (b)

Figure 2.24: Off-diagonal contribution of rescaled coalescence kernel. Note the peak for equal radii and the minimum for $\lg(r/r') \approx \pm 0.35$. Left: experimental data, right: numerical data, both evaluated for edge droplet distance $l = 0.25$. The parametrization given by (2.70) is plotted as a red line on top of the experimental data.

To account for this minor drift we normalize the rescaled coalescence kernel k by the corresponding diagonal value, thus defining

$$j(r,r') \equiv \frac{k(r,r')}{k(\sqrt{rr'},\sqrt{rr'})}. \tag{2.67}$$

which is plotted in figure 2.24. It turns out that j only depends on the ratio of the two radii. As a variable we therefore choose

$$x \equiv \log_{10}\left(\frac{r}{r'}\right). \tag{2.68}$$

We aim to find a simple parametrization of the off-diagonal contribution of the coalescence kernel. The peak at $x = 0$ can be well described by a Lorentz curve

$$j(x) \approx \frac{0.05}{x^2 + 0.05} \text{ for } x \lesssim 0.2. \tag{2.69}$$

To parametrize the tail for $x \to \pm 1$ we add a term of second order in $1 - |x|$ which is truncated to be positive

$$j(x) \approx \frac{0.05}{x^2 + 0.05} + \max\left(0\,;\ 0.5 - 0.85(1 - |x|)^2\right). \tag{2.70}$$

Putting equations (2.64) and (2.67) together, we can parametrize the coalescence kernel

$$\kappa(r,r') = \kappa_1 2\pi(r + r')j\left(\log_{10}(r/r')\right). \tag{2.71}$$

This parametrization will be used in section 2.5.4 to model the evolution of the droplet size distribution. We now move on to uncover the cause for the peak on the diagonal.

2.5.3.4 Age Distribution

The arising of the peak in both in the experimental and in the numerical data means, that droplets have an increased probability of coalescing with droplets of similar size. Studying an image of a breath figure (see fig 2.25) reveals the origin of that finding: The distribution of droplets is not homogeneous. In the image we find several regions. In each region, droplets of a certain size are dominant. This typical size is increasing with time in each region. This is in line with the coarsening of the droplet distribution due to droplet growth and coalescence, as discussed in section 2.5.1. Each region has a certain age being the time since it was released by coalescence or dripping of larger droplets. We thus conclude that the radii of adjacent droplets are not independent of each other.

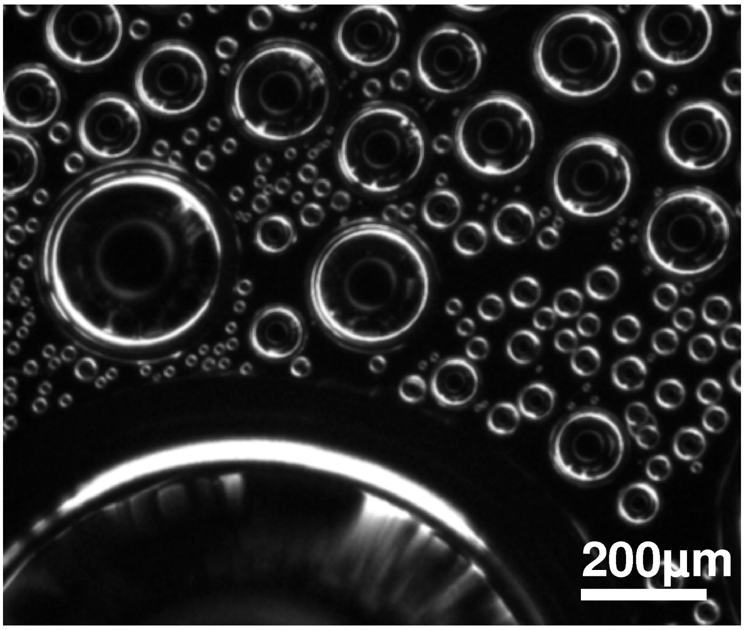

Figure 2.25: Several generations of droplets can be seen. The image can be split into a number of regions each characterized by a typical droplet size. As a result there is a preference for droplets to be surrounded by other droplets of similar size.

We now quantify these correlations by considering the variation of ages since regions were previously freed by coalescence or dripping events. We suppose that the radius distribution in regime (iii) can be described by

$$n(r,t) = n_0 r^{-\theta_r} f_r\left(\frac{r}{R(t)}\right). \tag{2.72}$$

In the steady-state case, we find that the radius distribution is a superposition of self-similar distributions of regime (iii). By $g(R)\mathrm{d}R$ we denote the probability of finding a region with the typical radius R. Hence we can write the droplet radius distribution as a weighted average over these regions

$$\begin{aligned} n(r) &= \int_{R_0}^{R_{\max}} n_0 r^{-\theta_r} f_r\left(\frac{r}{R}\right) g(R)\mathrm{d}R \\ &= n_0 r^{-\theta_r} \int_{R_0}^{R_{\max}} f_r\left(\frac{r}{R}\right) g(R)\mathrm{d}R. \end{aligned} \tag{2.73}$$

In order to test this prediction, we measure the distribution of region ages. The detection of big droplets by the image processing algorithm presented in section 2.4.1 works very reliable: All coalescence and dripping events above a certain threshold can be detected by droplet tracking. If droplets which were found in the previous image $n-1$, are not detected in the present image n, the released area is dilated and combined to regions. The regions are filled and made convex. Then the areas wetted by droplets in the neighborhood which are detected in the present image n are subtracted from the regions. Finally the regions are slightly rounded by opening and closing [55, pp 347]. After finding the released ares, we define an "age image". It has the same size as the original image. We initialize all pixels with $-\infty$. All pixels belonging to released regions in the image n are set to zero age.

Going to the next image $n+1$, all age values are incremented by one. Released areas are set to zero again. After several hours ($\approx$ 1000 images), the complete area has been released at least once and we can assign an age to each pixel. A plot of the age of regions is shown in figure 2.26(a). Comparing it to the actual photo (figure 2.26(b)) shows that the typical droplet radius of a region is highly correlated to the age of the region the droplet resides in. In section 2.5.1 we showed that the radius R grows linear in time. Having detected the released areas, we can measure their size distribution (see figure 2.27).

We find that the area distribution exhibits a scaling regime of the form

$$n(A) \sim A^{-\theta_A} \tag{2.74}$$

with $\theta_A = 2.2$. Note that the biggest released regions are several times larger than the area wetted by a large, almost dripping droplet. This can be explained by the observation that typically not isolated pairwise coalescences take place but multi-droplet-coalescences. However, these multi-coalescence events may be decomposed into a number of subsequent pairwise coalescences. From the "age images" (like the one shown in figure 2.26(a)) we

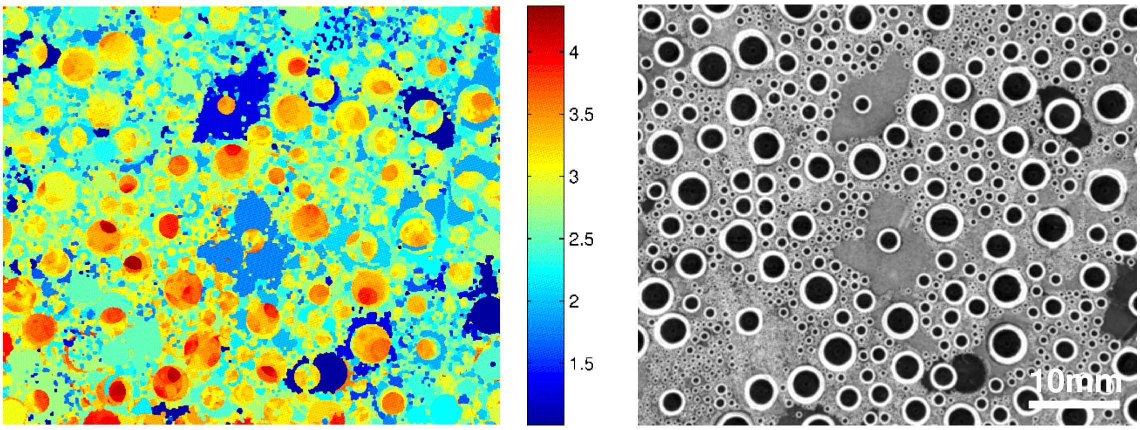

(a) (b)

Figure 2.26: The age of regions is indicated by color (left, decadic logarithm of age in seconds). The corresponding real image is shown for comparison on the right. Areas which were released recently are shown in dark blue, they are populated by tiny droplets. Note that the area released by a multi-coalescence and dripping event can be several times the area wetted by a big droplet (compare blue region in the center).

calculate the distribution of ages g(t) (see figure 2.28). This distribution can be approximated by a power law, too. We find that the age distribution scales $g(t) \sim t^{-1.0}$ and hence $g(R) \sim R^{-1.0}$, since $R \sim t$ in any of these regions.

2.5.3.5 Model of Coalescence Kernel

It is instructive to relate the superposition (2.73) to the coalescence probability. In section 2.5.3.2 we showed that the coalescence kernel could be well approximated by

$$\kappa(r,r') = k_0 2\pi (r + r') \tag{2.75}$$

if the droplets were distributed randomly, as suggested by Rogers et al. [95]. The probability that two droplets of radius r and r' coalesce, is proportional to $n(r)n(r')\kappa(r,r')$. Given, that the first droplet has the radius r, the probability of finding a coalescence partner with radius r' is not independent. With some probability h, both droplets belong to the same region and have to be chosen from a distribution of the form (2.72) with typical radius R. With the probability $1 - h$, droplets of two different regions with different R

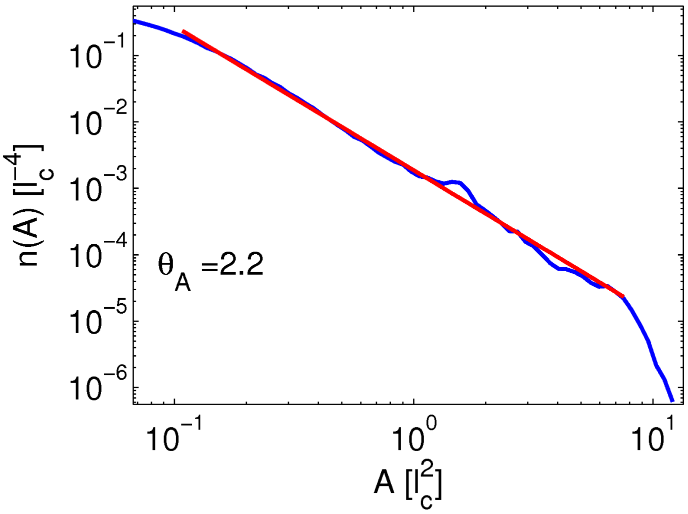

Figure 2.27: The size distribution of released areas follows a power law with slope $\theta_A = 2.2$ (experimental data). Note that the biggest released areas cover several of the biggest droplets.

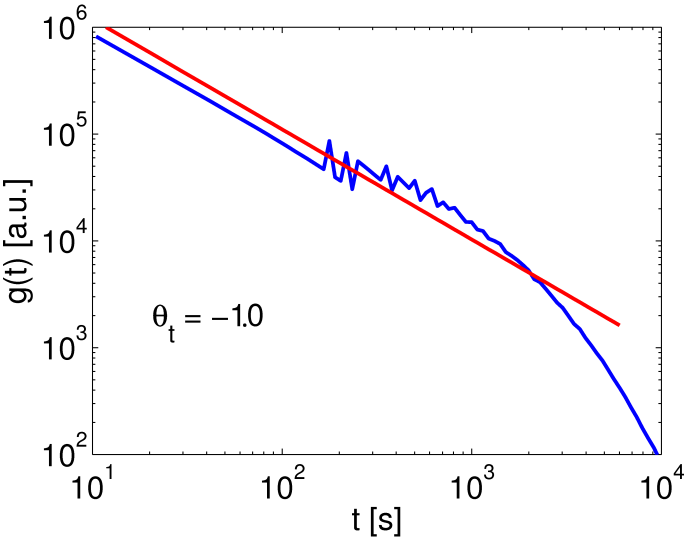

Figure 2.28: The distribution of droplet ages scales with $t^{-1.0}$ (experimental data).

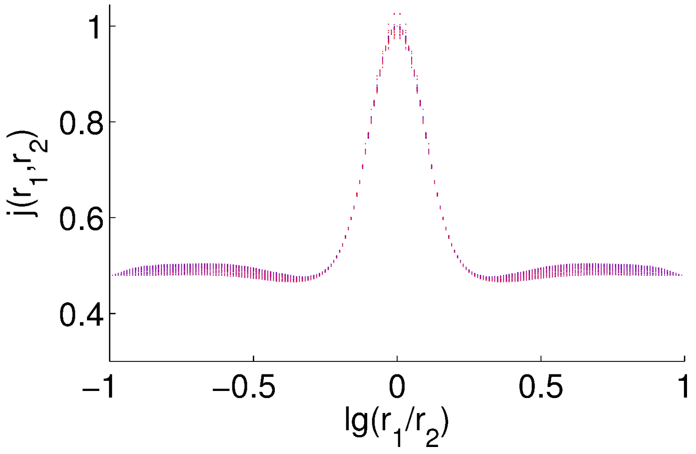

Figure 2.29: Prediction for off diagonal contribution of rescaled coalescence kernel. It is based on equation (2.71) using the rescaled radius distribution (fig 2.15(b)).

coalesce. Hence we can model the coalescence kernel by

$$\begin{aligned}\frac{\kappa(r,r')}{k_0 2\pi(r+r')} &\approx (1-h)+h\frac{\int_{R_0}^{R_{max}} n_0 r^{-\theta_r} f_r(\frac{r}{R}) n_0 r^{-\theta} f_r(\frac{r'}{R}) g(R)\mathrm{d}R}{n(r)n(r')} \\ &\approx (1-h)+h\frac{\int_{R_0}^{R_{max}} f_r(\frac{r}{R}) f_r(\frac{r'}{R}) g(R)\mathrm{d}R}{\int_{R_0}^{R_{max}} f_r(\frac{r}{R}) g(R)\mathrm{d}R \int_{R_0}^{R_{max}} f_r(\frac{r'}{R}) g(R)\mathrm{d}R} \qquad (2.76)\end{aligned}$$

Using the measured rescaled radius distribution $f(r/R)$ and the distribution of typical droplet radii $g(R)$, the off-diagonal contribution $j(r/r')$ can be modeled, using h as a free parameter. For $h = 0.13$ the prediction (figure 2.29) matches the measured curve (figure 2.24) fairly well.

2.5.4 Kinetic Equation

To describe the evolution of the droplet size distribution, we formulate a kinetic equation for the growth of droplets. It is based on a coagulation equation proposed by Smoluchowski [108]. In section 2.5.4.1 we extend this equation by additional terms for growth by vapor absorption, nucleation and dripping. we continue by transferring the kinetic equation for the size distribution into an equation for the radius distribution in section 2.5.4.2. This equation is easier to integrate numerically, which is done in section 2.5.4.3.

2.5.4.1 Model for the Evolution of the Size Distribution

The coagulation equation proposed by Smoluchowski [108] was introduced in section 2.2.4. We extend it by terms for condensational growth, nucleation and dripping in the spirit of the simulation scheme of Blaschke [23] (confer the beginning of section 2.5): The number of droplets growing from size $s - s_0$ to s is the product of the volume flux F in units of s_0

per droplet area $\pi \left(\frac{s-s_0}{c}\right)^{2/3}$ and the number density $n(s-s_0,t)$. Note that the combination $\left(\frac{s}{c}\right)^{1/3}$ is the droplet radius r. A similar term arises for droplets growing from size s to $s+s_0$. Finally, boundary conditions have to be implemented for the smallest and the biggest droplet size in the system. We model nucleation by a "rain" of droplets of size s_0 on the free fraction of the substrate. Dripping is modeled by a constant dripping rate d for droplets larger than some critical size s_c. Putting these terms together, we arrive at an explicit kinetic equation for the droplet size distribution.

$$\begin{aligned}\frac{\partial n(s,t)}{\partial t} &= \int_{s_0}^{s/2} \kappa(s',s-s')2\dot{r}n(s',t)n(s-s',t)ds' \\ &- n(s,t)\int_{s_0}^{s_c} \kappa(s',s)2\dot{r}n(s',t)ds' \\ &+ \frac{F}{s_0}\pi\left(\frac{s-s_0}{c}\right)^{2/3} n(s-s_0,t) - \frac{F}{s_0}\pi\left(\frac{s}{c}\right)^{2/3} n(s,t) \\ &+ \frac{F}{s_0}\left(1-\int_{s_0}^{s_c}\pi\left(\frac{s'}{c}\right)^{2/3} n(s',t)ds'\right)\delta_{s,s_0} - dn(s,t)\Theta(s-s_c).\end{aligned} \tag{2.77}$$

The dripping rate d is assumed to be very high, such that in each time step virtually all droplets of size $s \geq s_c$ are removed.

2.5.4.2 Conversion to Radii

To convert the equation for the evolution of the size distribution into an equation for the radius distribution, we use

$$n(s) = \frac{n(r)}{3cr^2}. \tag{2.78}$$

The volume increase due to condensation is proportional to the area wetted by the droplet beyond the cutoff due to the tail of the distribution

$$\frac{ds}{dt} = F\pi\left(\frac{s}{c}\right)^{2/3} \tag{2.79}$$

where F is the volume flux on the surface. Inserting (2.2) gives the growth rate

$$\dot{r} = \frac{F\pi}{3c}. \tag{2.80}$$

Thus we can eliminate the flux in equation (2.78)and arrive at

$$\begin{aligned}
\frac{\partial n(r,t)}{\partial t}\frac{1}{3cr^2} &= \int_{r_0}^{2^{-1/3}r} \kappa(r',(r^3-r'^3)^{1/3}) 2\dot{r} n(r',t) n((r^3-r'^3)^{1/3},t) \frac{1}{3c\left(r^3-r'^3\right)^{2/3}} dr' \\
&- n(r,t)\frac{1}{3cr^2}\int_{r_0}^{r_c} \kappa(r',r) 2\dot{r} n(r',t) dr' \qquad (2.81)\\
&+ \frac{\dot{r}}{cr_0^3} n\left(\left(r^3-r_0^3\right)^{1/3},t\right) - \frac{\dot{r}}{cr_0^3} n(r,t) \\
&+ \frac{\dot{r}}{\pi r_0^3}\left(1-\int_{r_0}^{r_c} \pi r'^2 n(r',t) dr'\right)\frac{1}{cr^2}\delta_{r,r_0} - dn(r,t)\frac{1}{3cr^2}\Theta(r-r_c).
\end{aligned}$$

We express time $t = \tau t_0$ in units of t_0

$$t_0 \equiv \frac{cr_0}{F\pi} = \frac{r_0}{3\dot{r}} \tag{2.82}$$

(confer section 2.5.1), giving

$$\frac{\partial n(r,t)}{\partial t}\cdot\frac{1}{3cr^2} = \frac{\partial n(r,\tau)}{\partial \tau}\cdot\frac{\dot{r}}{cr_0r^2} \tag{2.83}$$

for the left hand side of equation (2.82). For simplification we define a nondimensional dripping rate $\tilde{d} \equiv \frac{dr_0}{3\dot{r}}$. Multipyling by $\frac{cr_0r^2}{\dot{r}}$ and using the nondimensional time τ yields

$$\begin{aligned}
\frac{\partial n(r,\tau)}{\partial \tau} &= \int_{r_0}^{2^{-1/3}r} 2\kappa(r',(r^3-r'^3)^{1/3}) n(r',\tau) n((r^3-r'^3)^{1/3},\tau) \frac{r^2}{\left(r^3-r'^3\right)^{2/3}} dr' \frac{r_0}{3} \\
&- n(r,\tau)\int_{r_0}^{r_c} 2\kappa(r',r) n(r',\tau) dr' \frac{r_0}{3} \qquad (2.84)\\
&+ \frac{r^2}{r_0^2} n\left(\left(r^3-r_0^3\right)^{1/3},\tau\right) - \frac{r^2}{r_0^2} n(r,\tau) \\
&+ \frac{1}{\pi r_0^2}\left(1-\int_{r_0}^{r_c} \pi r'^2 n(r',\tau) dr'\right)\delta_{r,r_0} - \tilde{d} n(r,\tau)\Theta(r-r_c).
\end{aligned}$$

The growth due to condensation can be interpreted as a constant drift in the radius giving

$$\begin{aligned}
\left[\frac{\partial n(r,\tau)}{\partial \tau} + \frac{\partial n(r,\tau)}{\partial r}\frac{r_0}{3}\right] &= \int_{r_0}^{2^{-1/3}r} 2\kappa(r',(r^3-r'^3)^{1/3}) n(r',\tau) n((r^3-r'^3)^{1/3},\tau) \frac{r^2}{\left(r^3-r'^3\right)^{2/3}} dr' \frac{r_0}{3} \\
&- n(r,\tau)\int_{r_0}^{r_c} 2\kappa(r',r) n(r',\tau) dr' \frac{r_0}{3} \qquad (2.85)\\
&+ \frac{1}{\pi r_0^2}\left(1-\int_{r_0}^{r_c} \pi r'^2 n(r',\tau) dr'\right)\delta_{r,r_0} - \tilde{d} n(r,\tau)\Theta(r-r_c).
\end{aligned}$$

Note that this equation does not depend on the shape factor c anymore, implying that the contact angle does not matter for the evolution of the radius distribution (except for its influence on the dripping - i.e. the cutoff scale for large droplets).

2.5.4.3 Numerical Integration of Model Equation

Model equation (2.86) is integrated for a range of radii. The smallest radius r_0 is set to 1, the largest radius to $r_c = 1000$. This range of radii is comparable to the one observed in the experiment. For the integration of (2.86), the dripping rate $\tilde{d}$ is set to infinity. So the number of droplets with $r > r_c$ is taken to be zero for all times.
The integration is worked out for two different coalescence kernels. In the first run, a mean field coalescence kernel (2.29) is used. In the second run, a kernel of the form (2.71) is used. Figure 2.30 shows the result of the integration: The evolution of the size distribution predicted by equation (2.86) does not match the measured distributions at all. After a short time $\tau = 2.8$ the wetted fraction approaches 1 with a nonzero slope (compare figure 2.30(b)). This means that the decrease of the wetted fraction due to the pairwise coalescence kernel (2.29) does not balance the increase of w due to the condensational growth of droplets. Using the parametrization (2.71) of the experimentally measured coalescence kernel does not show a significant difference. Apparently the Smoluchowski equation does *not* properly describe the evolution of the droplet distribution. Possible origins of this deviation are addressed in the discussion.

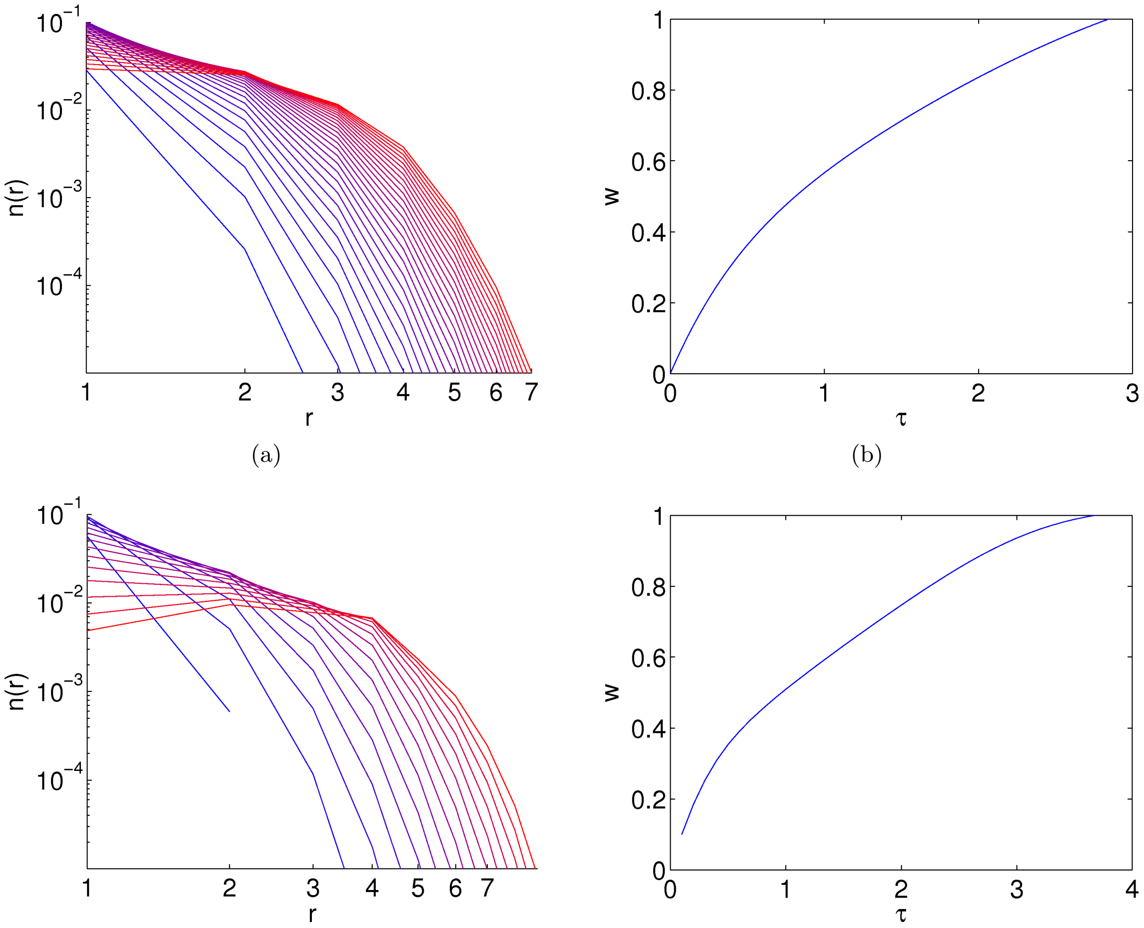

(a) (b)

(c) (d)

Figure 2.30: The kinetic equation (2.86) for the evolution of the droplet radius is integrated in time. In case one (upper panel), the mean field kernel (2.29) is used for the integration. In the second case (lower panel), the parametrization (2.71) of the experimentally measured coalescence kernel is taken. The distributions obtained for different times are displayed in the left panel. The wetted fraction (right) approaches one with a nonzero slope. The decrease of the wetted fraction due to the pairwise coalescence kernel does not balance the increase of w due to the condensational growth of droplets in both cases.

2.6 Discussion

In this section we summarize and discuss our results for the droplet distribution of breath figures.

- **Droplet Growth Rates:** In agreement with the literature [46] we find in section 2.5.1.2 that the typical radius R grows linearly in time (compare figure 2.13(a)), both for the experimental and the numerical case. A linear increase of the total droplet volume on the imaged part of the substrate (about 1mm^2) is observed (see figure 2.13(b)). The droplets forming the "bump" of the distribution gain 2.1 times the volume flux on the fraction of the substrate wetted by the "bump" droplets. We explain this finding in section 2.5.1.2 with means of equation (2.38).
- **Scaling of Size Distribution:** The "bump" of the size distribution can be rescaled perfectly by measuring droplet sizes s in units of the typical droplet size $S(t)$ and by rescaling the size distribution with $s^{5/3}$, as can be seen in figure 2.15, section 2.5.1.7. In variance with Family and Meakin's [46] assumption of a constant wetted fraction for the *whole* distribution in regime (iii) we show in section 2.5.1.6 that the porosity of the system is not constant but decreases with $p(t) \sim t^{-0.16}$ for the experimental and $p(t) \sim t^{-0.30}$ for the numerical data (confer figure 2.14). Regarding breath figures as a physical example for a fractal packing in section 2.5.1.3 leads to the conclusion, that the packing of droplets has a fractal dimension of $d_f = 1.84$ for the experimental breath figures and $d_f = 1.70$ for the numerically simulated ones. This gives a correction factor (confer equations (2.49) and (2.51)) for the scaling of the size distribution, fitting perfectly to the presented data in figure 2.15. The difference in the packing of the numerical and the experimental breath figures may be due to differences in the physics involved in the nucleation and growth of small droplets, e.g. the depletion zones around small droplets (confer section 2.2.2.1).
- **Lower Cutoff of Scaling Regime:** Both in the experimental data and in the numerical data of Blaschke [23] a lower cutoff for the scaling regime can be seen (figure 2.15). We explain the observed cutoff in section 2.5.1.3 by relating the droplet size distribution to the growth rate of the smallest droplets (2.45). In the experimental data, the cutoff for small droplets is very prominent: The scaling regime of the size distribution develops only at late times, just before the biggest droplets start to be influenced by gravity (confer section 2.2.1). We observe a scaling correction for the smallest droplets (2.49) consistent with the growth rate expected for diffusion limited growth (confer section 2.2.2.1). We can rescale the experimental and the numerical droplet size distribution each to a distribution with a flat horizontal tail. This result is shown in figure 2.16(a).
- **Steady-State Size Distribution:** We observe the effect of gravity on the droplet size distribution for droplet radii close to the capillary length $r \gtrsim 0.2 l_c$ in figure

2.17(a). Remarkably, the scaling of the steady-state distribution (regime (iv), sections 2.2.2.4 and 2.5.2) differs from the scaling of the self-similar distribution described above. The experimental data shows the scaling exponent $\theta_r = 3.0 \pm 0.1$ predicted for constant wetted fraction [46]. It is different to the scaling exponent $\theta_r = 2.7$ observed for breath figures on vertical substrates [117] and in the numerics of Blaschke [23] (see figure 2.17(b)). For the numerical simulations, this may be due to the limited range of droplet radii that can be simulated. Clearly more work is required here.

- **Coalescence Kernel:** The distribution of droplet pairs in a neighborhood shows a pronounced peak for droplets of similar sizes (see figure 2.19). We explain this observation in sections 2.5.3.4 and 2.5.3.5 by the assertion that adjacent droplets have a high probability of both belonging to the same local distribution with the characteristic radius R (equation (2.76)). Hence the "bump" in the size distribution of regime (iii) causes the peak on the diagonal of the pair correlation function. After division of the various factors contributing to the correlation function, even analogous to the dip in the rescaled size distribution (figure 2.15), we observe local minima of the correlation function in figure 2.24. We demonstrate in section 2.5.3.5, that the correction to the mean field coalescence kernel (2.29) can be calculated (2.76) from the size distribution in regime (iii). We need only a single fit parameter - the probability of neighboring droplets to belong to the same distribution.
- **Kinetic Equation:** In section 2.5.4 we extend the Smoluchowski equation (2.28) introduced in section 2.2.4 by explicit terms for condensational growth, diffusion and dripping (2.78). By transferring it into an equation for the evolution of the droplet radius distribution (2.86) we show that the radius distribution is independent of the contact angle, provided the droplets form spherical caps on the substrate. This matches our observation that we get comparable data in the experiment and the numerics. Integrating the evolution equation for the droplet radius (2.86) we find in section 2.5.4.3 that it does not properly describe the evolution of the distribution. The fraction of the substrate released by pairwise coalescences does not balance the increase in the wetted fraction due to condensational growth and nucleation (see figure 2.30). Probably, multi-coalescences [53] are much more effective in releasing substrate area than pairwise coalescences. When two rather big droplets coalesce, many other droplets that happen to be in the way of the new forming droplet get involved in the coalescence event. In figure 2.26 one can easily see, that multi-coalescences actually dominate the dynamics. Often, regions are released that are bigger than the area wetted by two of the largest droplets in the system (confer also figure 2.27).

2.A Droplet Reflection Patterns

The image processing algorithm that was described in section 2.4 relies on a detailed study of the droplet reflection patterns. We first define three different droplet radii in section 2.A.1, which characterize the reflection patterns and relate it to the physical droplet radius. We then measure the radial intensity distribution as a function of the radius in section 2.A.2. The radial intensity distribution is parametrized in section 2.A.3. On this basis, we define two match functions in section 2.A.4 to compare droplet detections to the image. These match function form the backbone of our image processing algorithm.

2.A.1 Definition of Characteristic Radii

For practical purposes three characteristic radii (compare figure 2.31) are defined. The three of them can only be measured for $r \gtrsim 15\mu\text{m}$ (check!). We find fixed relations between the radii that can be extrapolated to small droplets where the resolution is limited by diffraction. As three characteristic radii we distinguish

- a thin inner reflection ring at radius r_i with thickness $2\sigma_\text{i}$,
- a thick outer reflection ring with the outer edge radius r_o and thickness $2\sigma_\text{o}$ and
- a coalesce radius r_c.

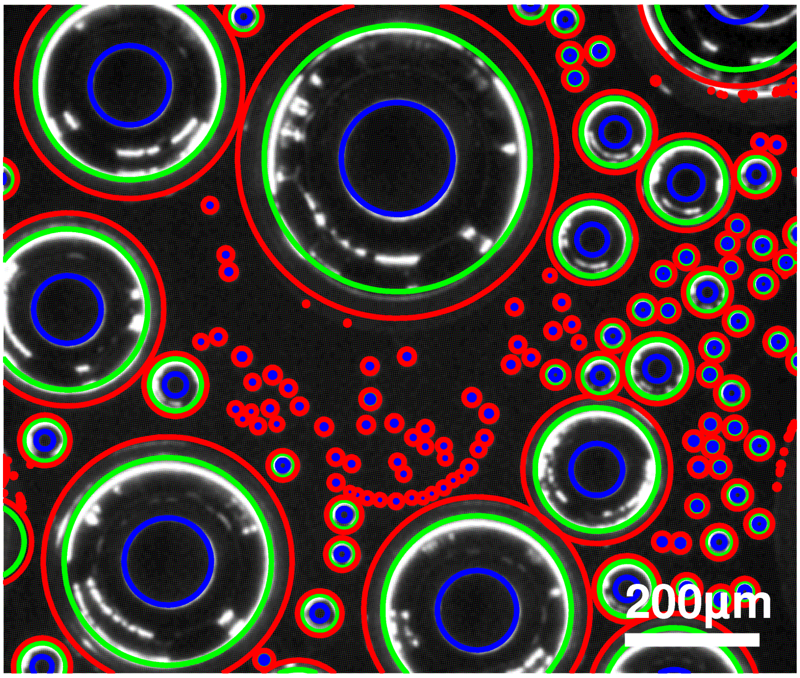

Figure 2.31: The image shows three droplet radii encoded by the color: The inner reflection ring r_i (blue), the outer reflection ring r_o (green) and the coalesce radius r_c (red).

The radii r_i and r_o can be directly determined by image processing. We are however most interested in the coalescence radius r_c, which can not be seen in the images. We observe, that droplets coalesce rapidly when the distance of their centroids is equal to the sum of their coalescence radii. By image processing, we determine the edge of the outer ring. By careful comparison of the detected radius r_o with the distance of droplets in images just before a coalescence event, we find that the coalescence radius amounts to $r_\mathrm{c} = 1.20 \cdot r_\mathrm{o}$ (compare figure 2.31). If the image processing algorithm detects several overlapping droplets, one of them (usually the smaller droplet) is considered to be an artifact. Therefore the radius r_c is vital for removing artifacts in the image analysis (see 2.4.2.3). We now move on to the calculation of radial intensity profiles, forming a basis for the droplet detection algorithm. In the analysis of our data in section 2.5, we refer to the coalescence radius as the droplet radius.

2.A.2 Radial Intensity Profiles

To accurately measure the droplet size distribution, a consistent criterion is needed to check the validity of droplet detections and to define the droplet radius. As a preparatory step, the radial intensity profile of droplet images is studied. In section 2.A.4 a parametrization of the profile will be used to define a single smooth function which calculates the match between the droplet detection and the image for all droplets. Radial intensity profiles of several hundred sample droplets were calculated and averaged for 20 radius bins (see figure 2.32). The profile is plotted as a function of $\hat{r}$, the radial distance from the centroid normalized by the outer reflection radius r_o.

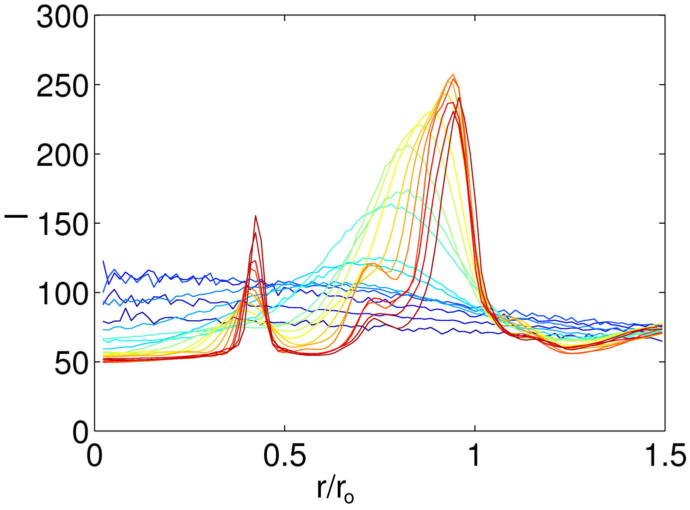

Figure 2.32: Radial intensity profile of droplets. The colors correspond to the radius of the droplets. For small droplets (dark blue), a Gaussian centered at the droplet center is observed. The width is determined by blurring effects. For slightly bigger droplets (light blue to green), one reflection ring is observed. We attribute this ring to reflections close to the contact line. For large droplets (yellow to red), a second inner reflection ring is visible. It arises due to double reflections on the droplet surface.

The form of the reflection pattern of the droplets depends on the droplet radius, as can be seen in figure 2.12 (rather refer to figure in section 3.1 with stages of droplet growth).

There are three types of droplet images which have to be distinguished. Tiny droplets only have one bright maximum in the center, the radial intensity distribution can be approximated by a Gaussian function (see dark blue curves in figure 2.32). For small droplets, one bright ring is visible with a dark core (light blue to green curves). The light is reflected close to the contact line. For big droplets (yellow to red curves), an inner rather sharp ring appears at $\hat{r} \approx 0.42$ and a bigger bright ring at $\hat{r} \approx r_\mathrm{o} - \sigma_\mathrm{o}$. Double reflections on the droplet surface cause the inner reflection ring.

The peaks in the radial intensity profile are fitted with Gaussian functions. The position of the inner ring r_i scales with the outer edge of the outer ring r_o. While the width of the inner ring $2\sigma_\mathrm{i}$ is constant (in units of r_o), the width of the outer ring $2\sigma_\mathrm{o}$ changes. The relations can be parametrized by

$$\begin{aligned} r_\mathrm{i}(r) &= 0.42r && (2.86)\\ \sigma_\mathrm{i}(r) &= 3.7 && (2.87)\\ \sigma_\mathrm{o}(r) &= \sqrt{4.0^2 + (0.050r)^2} && (2.88)\\ r_\mathrm{o}(r) &\equiv r. && (2.89) \end{aligned}$$

2.A.3 Parametrization of the Profile

Going from the droplet center outwards, a sequence of dark and bright regions is observed. For big droplets, we find an inner dark core in the center for $\hat{r} \leq r_\mathrm{core,in}$. It is surrounded by the inner reflection ring at $r_\mathrm{core,in} \leq \hat{r} \leq r_\mathrm{ring,in}$. Then a relatively dark regions follows for $r_\mathrm{ring,in} \leq \hat{r} \leq r_\mathrm{core,out}$. It is surrounded by a thick bright reflection ring in the range $r_\mathrm{core,out} \leq \hat{r} \leq r_\mathrm{ring,out}$. The direct environment of the outer ring $r_\mathrm{ring,out} \leq \hat{r} \leq r_\mathrm{env}$ is relatively dark again. Using the radii r_i, r_o and the ring half widths σ_i, σ_o the radii denoting the edges between dark and bright regions are defined. They correspond to extrema in the gradient of the intensity profile. The definitions of $r_\mathrm{core,in}$ and $r_\mathrm{core,out}$ have to ensure that the result is always positive, though being calculated by a difference of positive numbers. Special care has to be taken in defining $r_\mathrm{core,in}$ and $r_\mathrm{ring,in}$, as the inner reflection ring is only present on images of big droplets. To get a consistent description for all droplet radii, the values of $r_\mathrm{core,in}$ and $r_\mathrm{ring,in}$ have to be limited by the inner edge of the outer reflection ring $r_\mathrm{core,out}$.

$$\begin{aligned} r_\mathrm{core,in}(r) &\equiv \min(\max(0, r_\mathrm{i}(r) - \sigma_\mathrm{i}(r)), r_\mathrm{core,out}) && (2.90)\\ r_\mathrm{ring,in}(r) &\equiv \min(r_\mathrm{i}(r) + \sigma_\mathrm{i}(r), r_\mathrm{core,out}) && (2.91)\\ r_\mathrm{core,out}(r) &\equiv \max(0, r_\mathrm{o}(r) - 2\sigma_\mathrm{o}(r)) && (2.92)\\ r_\mathrm{ring,out}(r) &\equiv r_\mathrm{o} && (2.93)\\ r_\mathrm{env}(r) &\equiv r_\mathrm{o}(r) + \sigma_\mathrm{o}(r) && (2.94) \end{aligned}$$

Having defined the radii for the edges of the core, ring and environment regions, it is possible to calculate the mean intensities of the regions. It is also worthwhile to calculate the variation of the intensity in the inner core and the outer ring, because a low intensity variation of these two regions is characteristic. The result is shown in figure 2.33, which shows that the intensity of the inner core $I_{\text{core,in}}$, the rings $I_{\text{ring,in}}$, $I_{\text{ring,out}}$ and the droplet environment I_{env} depend on the droplet radius. The radius dependence of the mean intensities and the intensity variations can be well described by a combination of power laws and saturation values (see fitted lines in figure 2.33). We use the following parametrization for the radius dependence of the intensities

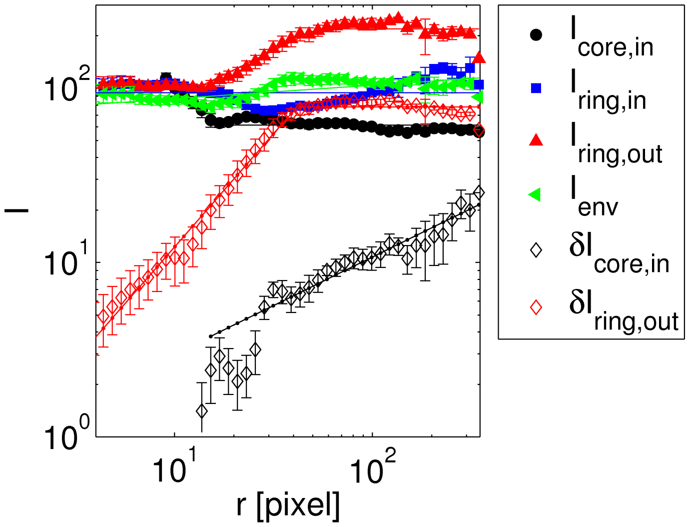

Figure 2.33: The intensity of the inner core $I_{\text{core,in}}$, the rings $I_{\text{ring,in}}$, $I_{\text{ring,out}}$ and the droplet environment I_{env} depend on the droplet radius. Also the variation of the intensity in the inner core $\delta I_{\text{core,in}}$ and at the outer ring $\delta I_{\text{ring,out}}$ is measured. The radius dependence can be well described by power laws and saturation values (fitted lines). The fit parameters are summarized in equations (2.95)-(2.100).

$$
\begin{aligned}
I^*_{\text{core,in}}(r) &= 61 && (2.95)\\
I^*_{\text{ring,in}}(r) &= 94 && (2.96)\\
I^*_{\text{ring,out}}(r) &= \max\left(104, \min\left(24 \cdot r^{0.55}, 200\right)\right) && (2.97)\\
I^*_{env}(r) &= 7.3 \cdot r^{0.08} && (2.98)\\
\delta I^*_{\text{core,in}}(r) &= 0.83 \cdot r^{0.56} && (2.99)\\
\delta I^*_{\text{ring,out}}(r) &= \min\left(78, 0.62 \cdot r^{1.30}\right). && (2.100)
\end{aligned}
$$

We also calculated the standard deviations of the mean intensities and the intensity variations. The standard deviations don't exhibit a consistent radius dependence (not shown).

Therefore, it is enough to compute the averages

$$\begin{aligned}
\mathit{\Delta} I_{\text{core,in}} &= 2.3 && (2.101)\\
\mathit{\Delta} I_{\text{ring,in}} &= 7.6 && (2.102)\\
\mathit{\Delta} I_{\text{ring,out}} &= 13 && (2.103)\\
\mathit{\Delta} I_{env} &= 8.0 && (2.104)\\
\mathit{\Delta} \delta I_{\text{core,in}} &= 1.2 && (2.105)\\
\mathit{\Delta} \delta I_{\text{ring,out}} &= 3.4. && (2.106)
\end{aligned}$$

2.A.4 Match Functions

For comparison of the detected droplets with the preprocessed images, two different match functions are used. The first match function is based on the intensity gradient at the outer edge of the outer reflection ring only. The second function is constructed from the parametrization of the averaged radial intensity profile.

On the one hand, the match of droplets is a good criterion to sort out erroneously detected droplets. On the other hand, the match functions can be applied for the improvement of the estimate of the droplet radius and position. For this purpose, radius and position are varied until a local maximum of the match is found.

Both match functions are used where appropriate, as they have different advantages and shortcomings. The gradient based match function gives reliable results for the determination of the droplet radius, provided that the prior estimates of the droplet radius and position are very good. Dark regions between droplets, which can be easily mistaken for droplets, are distinguishable by a small value of the gradient based match function. The match function based on the radial intensity profile has a bigger convergence radius for the optimization of the radius and the position estimate. It gives reasonable results even when the preliminary estimate of radius and position are not very accurate. However, the optimization of the profile based match can also give a good match for erroneously detected droplets. Often they can be distinguished from real droplets by posterior calculation of the gradient based match.

2.A.4.1 Gradient Based Match Function

The gradient based match function is used to detect the edge of the outer reflection ring r_{o}. It compares the average intensity of two rings $r_{\text{o}} \leq r \leq r_{\text{o}} + \mathit{\Delta} r$ (just outside of the outer reflection ring) and $r_{\text{o}} - \mathit{\Delta} r \leq r \leq r_{\text{o}}$ (part of the outer reflection ring), as

$$m_{\text{gradient}} = I(r_0 \leq r \leq r_0 + \mathit{\Delta} r) - I(r_0 - \mathit{\Delta} r \leq r \leq r_0) \qquad (2.107)$$

where $\mathit{\Delta} r = 3$pixel.

2.A.4.2 Radial Profile Based Match Function

For the definition of the intensity profile based match function we rely on the parametrization of the profile outlined in section 2.A.3. To the droplets shall be assigned a good (positive) match if they have a dark core, a dark environment and bright rings. The challenge is to interpolate smoothly between the cases of small droplets, where only the outer ring is visible and the case of big droplets where the inner ring is significant, too. For small droplets with $r < r_\mathrm{c} = 30$ we expect the pixels between $r_\text{core,in}$ and $r_\text{ring,in}$ to be relatively dark (negative sign in match function), for $r > r_\mathrm{c}$ we expect to see a relatively high intensity (positive sign). To interpolate smoothly between the two regimes, we define a prefactor α ranging from $\alpha(r_\mathrm{c} - 20) = -1$ to $\alpha(r_\mathrm{c} + 20) = +1$

$$\alpha(r) = -1 \,\text{for}\, r < r_\mathrm{c} - 20, \frac{r - r_\mathrm{c}}{20} \,\text{for}\, r_\mathrm{c} - 20 < r < r_\mathrm{c} + 20, +1 \,\text{for}\, r > r_\mathrm{c} + 20. \tag{2.108}$$

Each region of the droplet image (cores, rings, environment) contributes to the match weighted according to its area. We define the areas A_x as the intersection of a disc with radius $_\mathrm{x}$ and the image, where the index x denotes ring, core or environment regions. Note that $A_\mathrm{x} < \pi r_\mathrm{x}^2$ for droplets touching the edge. We are now in the position to define the match function

$$\begin{aligned} m_\text{profile} = & - \frac{A_\text{core,in}}{A_\text{env}} \cdot \frac{I_\text{core,in} - I^*_\text{core,in}}{\mathit{\Delta} I_\text{core,in}} \\ & - \frac{A_\text{core,in}}{A_\text{env}} \cdot \frac{\delta I_\text{core,in} - \delta I^*_\text{core,in}}{\mathit{\Delta}\delta I_\text{core,in}} \\ & + \alpha \frac{A_\text{ring,in} - A_\text{core,in}}{A_\text{env}} \cdot \frac{I_\text{ring,in} - I^*_\text{ring,in}}{\mathit{\Delta} I_\text{ring,in}} \\ & + \frac{A_\text{ring,out} - A_\text{core,out}}{A_\text{env}} \cdot \frac{I_\text{ring,out} - I^*_\text{ring,out}}{\mathit{\Delta} I_\text{ring,out}} \\ & - \frac{A_\text{ring,out} - A_\text{core,out}}{A_\text{env}} \cdot \frac{\left|\delta I_\text{ring,out} - \delta I^*_\text{ring,out}\right|}{\mathit{\Delta}\delta I_\text{ring,out}} \\ & - \frac{A_{env} - A_\text{ring,out}}{A_\text{env}} \cdot \frac{I_{env} - I^*_{env}}{\mathit{\Delta} I_{env}} \\ & - \frac{1}{r^2}. \end{aligned} \tag{2.109}$$

The first two contributions to the match are worked out from the core of the droplet. It should have a low density (i.e. negative sign in match function) and a small variation of the intensity. The third contribution corresponds to the inner ring of the droplet. This region either belongs to the dark core of small droplets ($\alpha < 0$) or to a bright reflection ring of large droplets ($\alpha > 0$). The fourth term represents the most prominent feature of the droplets, the bright (outer) reflection ring. It is expected to have a high intensity and an intensity variation close to the typical value $\delta I^*_{\mathrm{ring,out}}$. In contrast to the reflection ring the direct environment of it is expected to be relatively dark (negative sign). The magnitude of each contribution depends on its relative deviation from the typical values for droplets of their size. The intensity $I_{\mathrm{core,in}}$ denotes the mean intensity of a droplet's core in a certain image. The intensities $I^*_{\mathrm{core,in}}$ and $\mathit{\Delta} I^*_{\mathrm{core,in}}$ correspond to the mean value and its variation for an ensemble of droplets with the radius r. The intensities $I_{\mathrm{ring,in}}, I_{\mathrm{ring,out}}$ and I_{env} denote the mean intensities of the inner, outer ring and the droplet's environment, accordingly. The prefactors of the form $\frac{A_1 - A_2}{A_{\mathrm{env}}}$ give the weight of the relative area to each contribution which is covered by the feature (core, ring, environment). This makes the match function also well defined for non-existing droplet cores ($A_{\mathrm{core,in}} = 0$) or non-existing inner rings ($A_{\mathrm{core,in}} = A_{\mathrm{ring,in}}$).

3 Phase Separation

3.1 Introduction

A second experimental system, where the interplay of several droplet mechanisms can be studied is the phase separation of binary fluids. When the temperture of a binary mixture is slowly changed, droplets are nucleated. They grow, coalesce and sediment, showing an oscillatory behaviour during phase separation. They form a full precipitation cycle, which can be studied in the laboratory. The precipitation cycle at the demixing of binary fluids has important analogies to the precipitation cycle leading to rain formation in clouds. We therefore look at the formation of rain focussing on the open question of a bottleneck in the growth of droplets. With our investigations on the evolution of the droplet size distribution in demixing binary systems, we aim to shed light on this bottleneck in rain droplet growth.

3.1.1 Oscillatory Phase Separation of Binary Fluids

Droplets can be present in mixtures of several liquid components. Binary, ternary or even more complex systems are found in magma [110], alloys [63], cosmetics, pharmacy, food, oil reservoirs or paint [40]. The form of the phase diagram depends on the contributions of intermolecular attractive forces and entropy to the free energy of the system [133]. A binary fluid demixes into two phases, when the composition is in the unstable part of the phase diagram, inside the so called miscibility gap. This penomenon will be explained by a simple model in section 3.2. Most binary systems have an upper critical temperature and demix under cooling. Examples include methanol/hexane [1], cyclohexane/polystyrene [139] and raw spirit/vegetable oil [130]. Some systems, however, demix under heating, like water/butoxyethanol [84] or water/lutidine [59].

In many situations, the fluid is subject to a slow temperature change. On the one hand, this can drive convection [33, 100]. On the other hand, the system demixes, if temperature is moving into the regime of the miscibility gap. The demixing behavior of binary fluids subject to a slow temperature ramp has been investigated for a variety of systems, where oscillations in the heat capacity and in turbidity have been observed [8, 33, 60, 126, 128, 132]. The oscillations originate from a complex interplay between nucleation, diffusion, coagulation and sedimentation.

In figure 3.1, a series of snapshots of a video showing the phase separation of a mixture of water and butoxyethanol from [128] is reproduced. The mixture is continuously heated

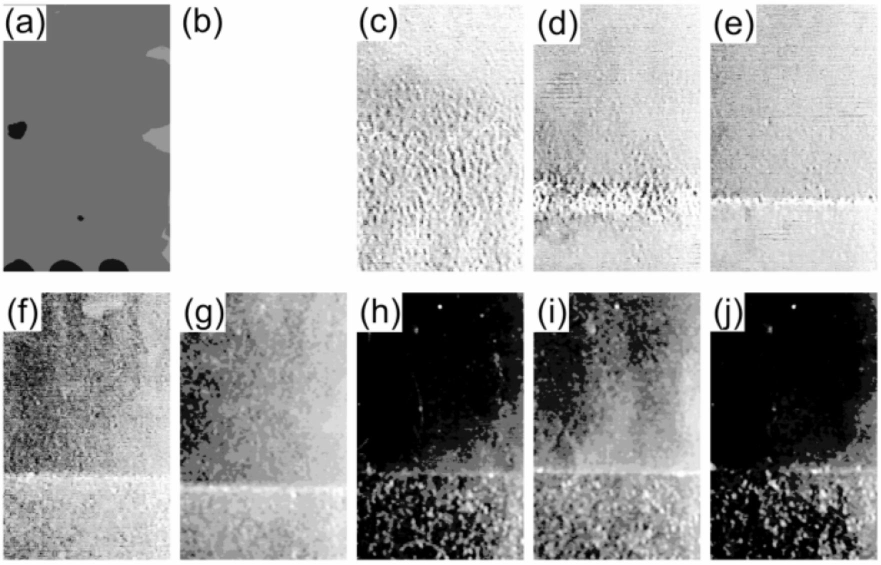

Figure 3.1: The series of photographs reproduced from [128] shows a mixture of water and 32% butoxyethanol, heated with 10k/h for different times. At the beginning of the temperature ramp, the sample is in one phase (a). When the critical temperature of the mixture is crossed, many droplets are nucleated (b), yielding a high turbidity of the sample. The droplets coalesce (c) and two layers with a meniscus inbetween are forming (d). The droplets sediment towards the interface (e) and the sample clears up. Subsequently, a new nucleation wave sets in (f), the droplets coalesce and sediment again (g,h). A third cycle is observed in (i,j).

with 10K/h from the one phase regime (a) into the miscibility gap. Once the critical temperature is reached, many droplets are nucleated and the sample gets turbid (b). The droplets coalesce (c) and a meniscus forms with a water-rich laxer at the bottom and a butoxyethanol-rich layer in the top (d). The droplets sediment towards the interface (e) and the sample clears up. Then a second nucleation wave is observed (f) with subsequent coarsening and sedimentation (g,h). A third cycle can be seen in (i) and (j).

Note that these repeated cycles in the evolution of the droplet distribution are similar to the steady-state regime observed in breath figures (confer section 2.2.2.4). Droplets are nucleated, grow, coalesce and are removed by gravity, yielding space for new generations of droplets. In breath figures, these cycles are run through by almost independent distributions in different regions of the substrate simultaneously. In the phase separation experiment, however, the cycles in the distribution of droplets are synchronized by a convective flow in each layer of the sample.

By keeping the mass flux in the system constant, more than 20 oscillations during one experimental run can be observed [8]. The amplitude of the oscillation decreases rapidly, also the period is decreasing during the temperature ramp. The origin of this drift was unclear up to now. Also a dependence of the oscillation period on the driving rate has been observed [60]. However, as the period changes in each ramp significantly (easily by a factor of 5, see figure 3.17), it is difficult to determine the driving dependence on the amplitude. On the one hand, measurements in different geometries suggest that the oscillation period is not affected significantly by the geometry [130]. This excludes the convective flow or interface effects to be the dominant mechanisms determining the time scale of the oscillations. On the other hand, a coupling of the oscillations in the two layers has been suggested [60].

In this thesis, we aim to clarify the parameter dependence of the oscillation period. Therefore, we build a fully automated experimental setup and scan the parameter space for the oscillations in more than 200 measurements. Heating rates are varied over almost three orders in magnitude and the reduced temperature θ

$$\theta \equiv \frac{|T - T_c|}{T_c} \tag{3.1}$$

is varied over two decades, where T is the absolute temperature and T_c is the critical temperature of the mixture (see section 3.2). Measurements are taken in both layers. Also the influence of the height, the width of the sample and the starting composition is tested. The results for the parameter dependence of the oscillation period are presented in sections 3.6.1.3, 3.6.3.4 and 3.6.4.

We now move on to clouds, where a precipitation cycle of nucleation, diffusional growth, collisions and sedimentation is described for the formation of so called "warm rain" [66, pp. 310].

3.1.2 Rain Formation

Clouds Since clouds can enhance or diminish the green house effect of the earth's atmosphere, a better understanding of cloud physics is important to improve climate models. This is a challanging enterprise because the micro-physics of clouds is fairly complex [90]: chemical reactions, thermodynamic coupling of phase transitions between liquid water, vapor and ice at the presence of a variety of cloud condensation nuclei as well as particle-flow interactions are at work. On the other hand, clouds are a multi-scale phenomenon with turbulence involved [24]. Here we focus on the droplet growth in warm clouds where all layers have temperatures above the freezing point. Hence the complex interplay of cloud droplets with ice crystals [66] does not have to be considered. Similar to breath figures, one encounters a broad distribution of droplet sizes in clouds [29, 34, 35, 140]. The droplet size distribution determines the optical properties of clouds and couples to the motion and the thermodynamics of clouds.

Laboratory Experiments A key issue to understand warm rain formation is detailed knowledge about the droplet size distribution and its evolution in time. Theoretical de-

scriptions based on diffusional droplet growth predict narrow distributions [90], whereas growth by collisions may introduce bimodal distributions [66, 103]. Field data are available from aircraft flight campaigns [14, 140] or helicopter flights with the measurement equipment immersed into the cloud hanging on a rope [105]. An alternative option is to do measurements on mountain tops [87]. Field data shows broad mono-modal distributions [29, 34, 35, 140]. It remains unclear however, whether this result is just due to averaging over large regions within the cloud during measurements and a correct interpretation of field data remains challenging [140].
Several aspects of droplet growth have been studied in laboratory experiments with well controlled conditions. Among these are

- Mixing of cloud and clear air [64],
- Collision rates of droplets in wind tunnel experiments [124],
- Droplets in Rayleigh-Bénard convection [141] and
- Nucleation in cloud chambers [109].

These experiments have isolated different mechanisms of cloud droplet growth and try to mimic typical cloud conditions relevant for the specific mechanism in their experiment. However, to our knowledge there has not been a single experiment yet where a full precipitation cycle (nucleation, diffusional growth, collisional growth, sedimentation) as a whole can be studied. By investigating the precipitation cycle observed in the phase separation of binary fluids, we aim to shed light on the cycle leading to the production of warm rain.

Precipitation Cycle A sketch of the described precipitation cycle is shown in figure 3.2. Upwinds lift warm humid air parcels to colder layers in the atmosphere. The temperature is decreasing roughly with the adiabatic lapse rate of 1K/100m [114, p. 109] and the relative humidity increases. Once the water vapor is supersaturated, droplets are nucleated on cloud condensation nuclei (CCN), such as salt, ammonium sulfate, hydrogen peroxide, sulfuric acid or nitric acid [114, p. 161]. The supersaturation diffuses to the droplets and triggers growth to a radius of up to 10μm within $\mathcal{O}(100\text{s})$ [90, p. 511]. Droplets continue to grow by coalescing with other droplets. At a droplet radius of about 50μm sedimentation velocities of droplets get significant. Sedimenting through layers with smaller droplets, they collide with smaller droplets on their path, called gravitational collection [90, pp. 617]. Eventually when the droplets have grown to about 2mm radius, the settling velocity exceeds typical convection velocities in the cloud and the droplets fall down, observed as rain. If bigger droplets are formed, they break up because the air resistance is bigger than the surface tension [122].
3.2.

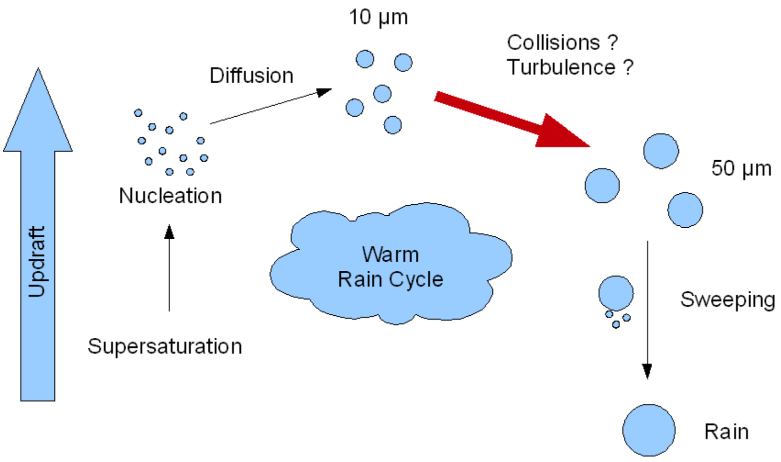

Figure 3.2: Upwinds raise cooling air parcels increasing supersaturation. Droplets are nucleated and grow by diffusion to about 10 μm. The continue to grow by coalescences, which may be enhanced by turbulence. For droplets of 50μm or larger sedimentation is dominating and the droplets grow by gravitational collection of smaller droplets in their path.

Bottleneck in Droplet Growth In the described precipitation cycle a bottleneck in droplet growth is asserted [103, 137]. For droplets smaller than 10μm, growth by condensation of water vapor is effective. Droplets bigger than 50μm easily grow by gravitational collection. However, in the range between 10 and 50μm (the exact values may depend on the details of the setting) neither diffusional nor gravitational growth seems to be effective [90]. Nevertheless, full precipitation cycles within 15 min are observed in nature, raising the question how the apparent bottleneck is passed on the timescale of minutes. It has been proposed that the turbulence present in clouds enhances collision rates of droplets and therefore speeds up droplet growth [24, 38, 44, 99, 103, 120]. Several mechanisms how turbulence can accelerate droplet growth have been suggested:

- **Air Entrainment:** Since the water vapor pressure curve is not linear in temperature but convex, entrainment of cold dry air and mixing with relatively warm humid air increases the relative humidity [75, 114, p 148].

- **Preferential Concentration:** Maxey [78] suggested a centrifuge mechanism: Heavy particles are expelled from high vorticity regions by centrifugal forces. Hence the particles preferentially concentrate on regions of low vorticity and high shear rates. Locally increased droplet number concentrations would enhance collision rates [56].

- **Collision Efficiency:** If the particle response time to the flow τ_p is of the same order than the time scale of fluid velocity fluctuations τ_f, the fluctuations can enhance relative velocities of particles and therefore increase the number of collisions. This effect has been studied in great detail by numerical simulations [10, 11, 44, 99] as a function of the Stokes number $\mathrm{St} = \tau_p/\tau_f$.

However, it is difficult to judge the relevance of the suggested mechanisms to the broad range of cloud conditions observed in nature. Air entrainment and preferential concentration are acting on very large scales compared to the scale relevant for the micro-physics of droplet growth (nucleation and diffusion). An increase of the collision efficiency is probably also relevant on the droplet size scale.

Here we focus on the micro-physics that determines the evolution of the droplet size distribution. We are looking at the processes which are at work below the Kolmogorov length ($\mathcal{O}(1cm)$ for cloud turbulence). Typical Stokes numbers in the experiment are smaller than 10^{-6} [67]. Even for a flow with high turbulence intensity with a Kolmogorov time scale of the order of microseconds, the Stokes number in a binary fluid would not exceed 10^{-3}. Due to the small density differences of fluids, kinematic particle-turbulence interactions [120] can hence be ruled out for droplets, even in a turbulent flow.

How do the droplets pass the bottleneck when turbulence effects can be neglected? Can a bottleneck in droplet growth be seen in the evolution of the droplet size distribution? Are broad distributions due to averaging or is the distribution at a certain time and location broad itself?

We aim to shed light on these questions by studying the precipitation cycle that can be observed in well controlled phase separation experiments with binary fluids. To this end, we design and construct an experimental setup, which is optimized to image droplets in the size range of the possible bottleneck. We develop an image processing algorithm to detect and to track droplets. In contrast to existing droplet tracking algorithms, we explicitly keep track of the droplet radius and include an assumption for the sedimentation velocity of droplets. The evolution of the droplet size distribution that we measure is presented in section 3.6.1.2. We analyze the bottleneck in droplet growth that we find in section 3.6.2.4. In the following, we give an outline of the chapter.

3.1.3 Outline of Chapter

We introduce the main concepts of phase separation in binary fluids starting with a simple model for the free energy of binary fluids (section 3.2). Then in section 3.3 we present the model system which we used to study the precipitation cycles. In section 3.4 the experimental setup is described and the experimental protocol is explained. In the next section 3.5, we explain the image processing and droplet tracking algorithm that we developed in order to measure droplet size distributions and velocities simultaneously. In section 3.6, our results for the droplet size distribution, droplet volume fraction and droplet number density are presented. We look at the bottleneck in droplet growth and derive a simple model for the parameter dependence of the oscillation period and amplitude. The results are discussed in section 3.7 in light of the questions raised above. Some important material parameters of our model system are summarized in the appendix 3.A.

3.2 Binary Fluids: The Φ^4-Model

3.2.1 Free Energy Model

A basic physical description of binary fluids can be derived from density functional theory for the free energy F of binary fluids [28].

$$F = \int \left[F_0(\Phi) + \frac{K}{2} (\nabla \Phi)^2 \right] \mathrm{d}V. \tag{3.2}$$

The composition Φ denotes the mass, volume or molar fraction of one component and serves as the order parameter in the transition from a disordered to an ordered phase. A prefactor K is introduced for the energy associated with composition gradients. The potential energy of the homogeneous solution is described by $F_0(\Phi)$. A simple prototype will be discussed below to describe the essential concepts of binary fluids.

Interfacial Energy The energy of the composition gradient is modeled by the contribution $K/2(\nabla\Phi)^2$ to equation (3.2). It costs a lot of energy to form an interface of a sharp composition gradient. Assuming that the thickness of an interface is constant, it directly follows from (3.2) that the energy associated with the formation of an interface is proportional to its area. Therefore, physical systems always seek to minimize interfaces between different phases. This effect was already mentioned in the discussion of the wetting of substrates in section 2.2.1. The surface energy depends on the strength of attractive forces between the molecules. As the molecule interactions are temperature dependent, so is the surface energy. This is the origin of the Marangoni effect [102], where temperature gradients in the system drive a flow induced by surface tension gradients. It can already be seen from (3.2) that the interfacial tension may increase linearly in leading order with the composition difference $\Delta\Phi$ of two phases.

Potential Energy A simple prototype for the potential F_0 of a binary fluid is the Φ^4-model [28], providing an approximation for $F_0(\Phi)$:

$$F = \int \left[F_0(\Phi) + \frac{K}{2} (\nabla \Phi)^2 \right] \mathrm{d}V = \int \left[\frac{A}{2} \left(\Phi - \frac{1}{2} \right)^2 + \frac{B}{4} \left(\Phi - \frac{1}{2} \right)^4 + \frac{K}{2} (\nabla \Phi)^2 \right] \mathrm{d}V. \tag{3.3}$$

The prefactors A and B are temperature dependent constants and define the shape of the potential $F_0(\Phi)$. In equilibrium, the system is in the global minimum of the free energy. To ensure that such a minimum exists, the factor B has to be always positive. When A is also positive, the potential has only one minimum at $\Phi = 1/2$ which is illustrated in figure 3.3(a) (top). The system is in one disordered phase once it reaches equilibrium. In case A is negative, two minima are present at $\Phi_{\mathrm{binodal}} = 0.5 \pm \Phi_0$ with $\Phi_0 \equiv \sqrt{|A|/B}$, shown in figure 3.3(a) (bottom). In equilibrium, the phases of the system have the compositions

Φ_{binodal} separated by the so called miscibility gap of the width $2\Phi_0$. A sketch of the phase diagram is shown in figure 3.3(b). We plot it for the case of A being a monotonously falling function of temperature, resulting in a lower critical solution temperature (LCST) T_c. Most binary fluids show upper critical solution temperatures (UCST), as mentioned in section 3.1.1. The model system that we chose for our experimental investigations (see section 3.3), however, also has a LCST.

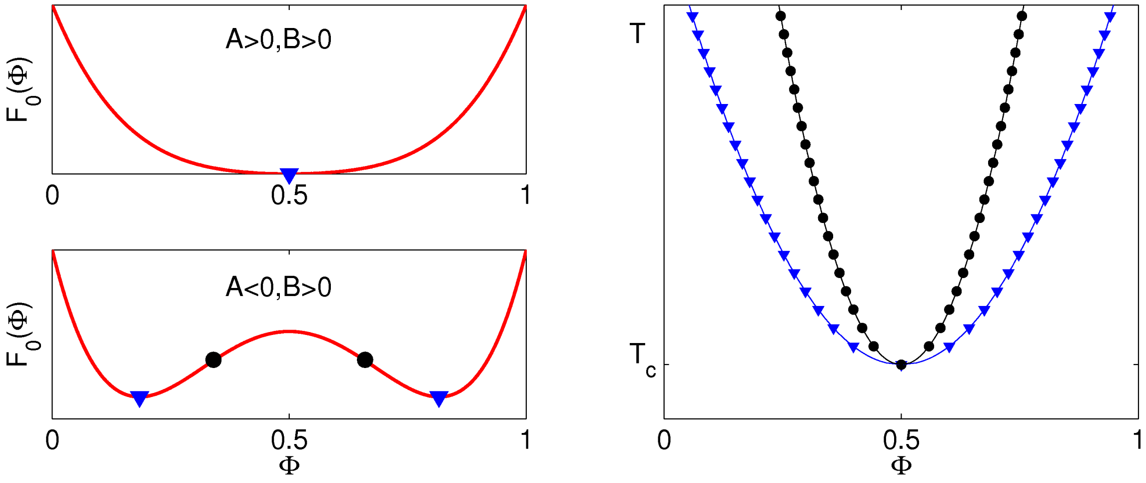

(a) (b)

Figure 3.3: (a) The Φ^4-model for the free energy (3.3) is plotted for two sets of variables A,B. The composition Φ denotes the fraction of one component in the system. If A and B are both positive (top), the energy potential $F_0(\Phi)$ has only one minimum at $\Phi = 0.5$ (blue triangle). If $A < 0$ and $B > 0$ (bottom), the energy potential has two minima (blue triangles) at $\Phi_{\text{binodal}} = 0.5 \pm \Phi_0$. The composition Φ_0 is defined by $\Phi_0 \equiv \sqrt{|A|/B}$. Two inflection points (black disks) are present at $\Phi_{\text{spinodal}} = 0.5 \pm \sqrt{|A|/3B}$.
(b) Sketch of a phase diagram for the case of A being a monotonously falling function of temperature. For low temperature, the two components form a stable mixture for any composition. This corresponds to the case ((a), top) where the free energy potential has only one minimum. At the critical temperature T_c, the sign of A changes and two minima in the energy appear. The binodal (blue triangles) corresponds to the compositions of the minima of the free energy potential ((a),bottom) for a given temperature. The spinodal (black disks) is defined by the inflection points of the free energy for a given temperature. Outside the binodal the mixture is stable. Between binodal and spinodal it is metastable and inside the spinodal it is unstable.

3.2.2 Evolution of Composition

Phase transitions are described by the evolution of a so called order parameter. In phase separation, the composition serves as an order parameter. When the order parameter is conserved, as it is the case for phase separation, an appropriate equation of motion for the order parameter in the absence of a center of mass flow is of the form [28]

$$\begin{aligned}
\frac{\partial \Phi}{\partial t} &= \lambda \nabla^2 \frac{\delta F}{\delta \Phi} \\
&= \lambda \nabla^2 \left[\frac{\partial F_0}{\partial \Phi} - K \nabla^2 \Phi \right] \\
&= \lambda \nabla^2 \left[A \left(\Phi - \frac{1}{2} \right) + B \left(\Phi - \frac{1}{2} \right)^3 - K \nabla^2 \Phi \right].
\end{aligned} \tag{3.4}$$

Following [129] the normalized composition

$$\varphi \equiv \frac{\Phi - \frac{1}{2}}{\Phi_0} \tag{3.5}$$

is introduced and the time derivative is computed to be

$$\frac{\partial \varphi}{\partial t} = \frac{1}{\Phi_0} \frac{\partial \Phi}{\partial t} - \varphi \frac{1}{\Phi_0} \frac{\partial \Phi_0}{\partial t}. \tag{3.6}$$

For the first term, equation (3.5) can be inserted. In the second term, a driving parameter is identified

$$\xi_0 \equiv \frac{1}{\Phi_0} \frac{\partial \Phi_0}{\partial t}. \tag{3.7}$$

It accounts for the change of the miscibility gap width with temperature and acts as a source of supersaturation $\sigma \equiv 1 - |\varphi|$. The evolution equation for the normalized composition follows

$$\frac{\partial \varphi}{\partial t} = \lambda \nabla^2 \left[A\varphi + B\Phi_0^2 \varphi^3 - K \nabla^2 \varphi \right] - \xi_0 \varphi. \tag{3.8}$$

Recalling $A < 0$, $\Phi_0^2 = |A|/B$ and introducing an equilibrium diffusion coefficient $D \equiv 2\lambda|A|$ and the interface thickness $\delta \equiv \sqrt{K/|A|}$, we arrive at a nonlinear diffusion equation [129]

$$\frac{\partial \varphi}{\partial t} = \nabla \left[\frac{D}{2} (3\varphi^2 - 1) \nabla \varphi \right] - \frac{D}{2} \delta^2 \nabla^4 \varphi - \xi_0 \varphi. \tag{3.9}$$

It is important to note that the diffusion coefficient $D(3\varphi^2 - 1)/2$ depends on the normalized composition. If the system is close to equilibrium, $\varphi \approx \pm 1$ everywhere, then the diffusion coefficient simplifies to the equilibrium coefficient D. If the system is far from equilibrium, in the so called spinodal range

$$-\varphi_s \equiv -1/\sqrt{3} < \varphi < 1/\sqrt{3} \equiv \varphi_s, \tag{3.10}$$

the diffusion coefficient is even negative. This has been referred to as "uphill" diffusion. Thus, in this regime, small fluctuations are amplified by diffusion until other terms take over. The composition where the diffusion changes sign is called the spinodal in the phase diagram. More generally, the spinodal is defined by the inflection points of the free energy potential

$$\frac{\partial^2 F_0(\Phi)}{\partial \Phi^2} \equiv 0. \tag{3.11}$$

3.2.3 Phase Separation Scenarios

For the phase separation of binary fluids, three different regimes have to be distinguished [129], sketched in figure 3.4. They differ by the type of the temperature protocol and by the way the system reacts to the temperature change.

3.2.3.1 Very Slow Temperature Change

We consider the already phase separated system. When the change in temperature is *very* slow [129], as illustrated in figure 3.4(a) (top)

$$\frac{\xi \Lambda^2}{D} \ll 1, \tag{3.12}$$

where Λ is the system size, the diffusion term in (3.9) balances the driving term $\xi_0 \varphi$. The sketch in figure 3.4(a) (bottom) indicates, that the composition follows the binodal closely. Typical values for our experiment are ξ=$1 \cdot 10^{-5}\text{s}^{-1}$, Λ=$1 \cdot 10^{-2}\text{m}$ and D=$1 \cdot 10^{-10}\text{m}^2/\text{s}$, so we are usually not in this regime with our experiments.

3.2.3.2 Quench in Temperature or Pressure

The next simplest, certainly more interesting way one can drive the system is to do a quench experiment, as sketched in figure 3.4(c). Either temperature or pressure are changed very fast compared to the time scale of the system's response. After the quench, temperature (and pressure) are carefully kept constant and the response of the system is monitored. Considering (3.7) and the diffusion equation (3.9), this implies that the driving term is zero after the quench. The evolution of the normalized composition is determined by diffusion and the formation of interfaces. Depending on how much the system is driven into the miscibility gap, the system reacts by two distinguished mechanisms. If the temperature changed very much, i.e. the composition is inside the spinodal range (3.10), the system demixes via so called spinodal decomposition. If the system was only slightly quenched and the composition is between the binodal and the spinodal, the system demixes via the formation of droplets.

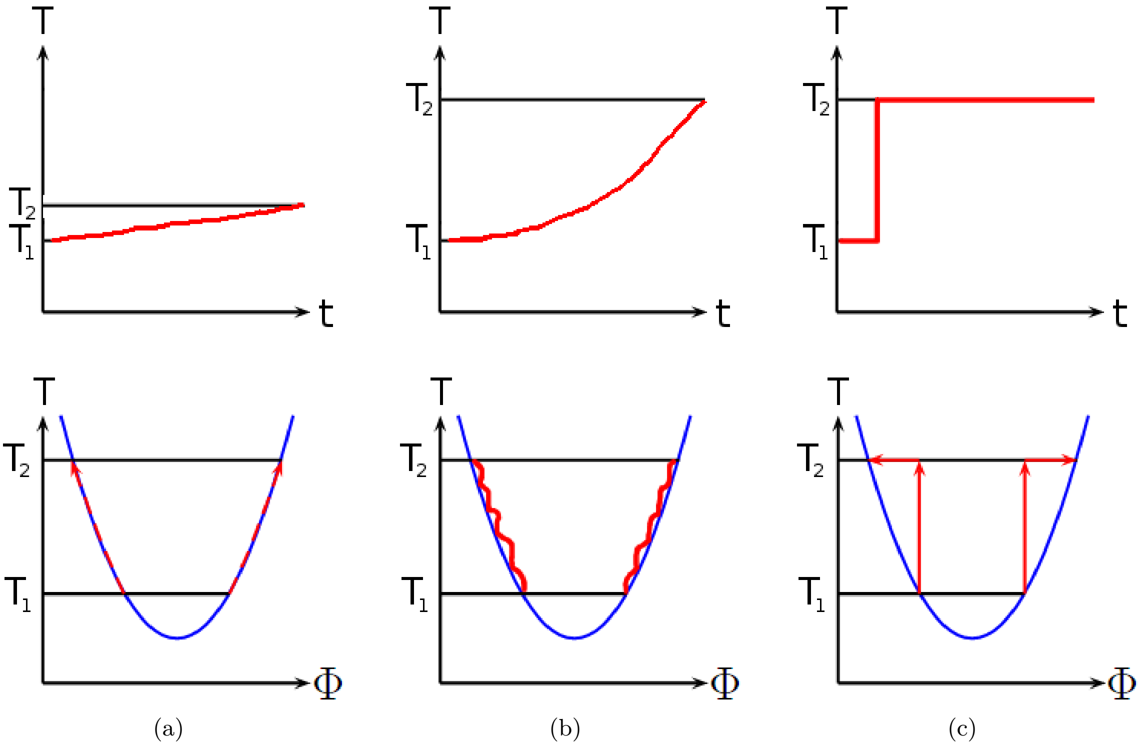

Figure 3.4: Depending on the temperature protocol (top), three different demixing scenarios (bottom) have to be distinguished.
(a) For very slow temperature changes, the compositions of the two phases follow the binodal by diffusion.
(b) At intermediate temperature changes, the separation occurs in an oscillatory manner.
(c) For fast temperature quenches, the nucleation of droplets or spinodal decomposition are observed.
The figure is adapted from Rohloff [96] and extended.

Droplet Formation Between the binodal and the spinodal, the system is in a metastable state. Gibbs [54] formulated two criteria for metastable phases. Metastable phases correspond to local minima of the free energy of the system, which are stable against small perturbations, i.e. in the convex region of $F_0(\Phi)$. This includes stability against small changes over a large area and stability against large changes over small areas. In the metastable phase, nucleation of droplets sets in at discrete nucleation sites (homogeneous or heterogeneous), the thermodynamics of fluctuations being important. Let us consider a system with a composition between binodal and spinodal, on the left hand side (i.e. rich in component A). As the system is not at the global minimum (i.e. the binodal), it is supersaturated in component B. The excess volume of component B diffuses to the droplets and is absorbed, whereas the component A diffuses from the droplets into the bulk. The composition of the droplets is determined by the right branch of the binodal, whereas the bulk gets to the left branch by expelling excess molecules of component B. The growth rate of droplets can be measured and used to determine the diffusion coefficient [111].

Spinodal Decomposition If the system is far inside the miscibility gap, the mean field free energy is concave, and the system is unstable to all perturbations. The system separates by spinodal decomposition, which is uniformly in space and has no thermodynamic barrier [21]. As discussed above, it is characterized by a negative diffusion coefficient. Small variations of the composition are enhanced, and domains with different compositions develop. The length scale of the domains grow rapidly in time, showing a self-similar growth comparable to the regime (ii) described in breath figures (confer section 2.2.2.2).

3.2.3.3 Slow Temperature Change

In most realistic scenarios, the temperature change of binary fluids is in an intermediate regime between the very slow temperature change and a temperature quench (figure 3.4(b)). The simplest way to keep the system in this intermediate regime is to set the driving parameter ξ_0 in the diffusion equation (3.9) to a constant. It is this regime, where an oscillatory demixing process is observed, as described in section 3.1.1. As illustrated in figure 3.4(b) (bottom), the composition evolves almost stepwise in time. First, the composition stays roughly constant while the temperature is increasing. When the system is far enough inside the miscibility gap, droplets are nucleated and diffusion on the scale of droplet distances brings the composition back to the binodal. After the droplets have disappeared (by coalescences or sedimentation or a combination of both), diffusion acts on the length scale of the system size again, so the composition cannot follow the bimodal again. Vollmer et al. [130] suggest a minimal model for oscillation cycles in phase separation. It is based on the diffusion equation (3.9) and approximates the composition profile around droplets due to diffusion to get an evolution equation for the supersaturation, which depends on the droplet number density n. The second ingredient is a simple model equation for the evolution of the droplet number density

$$\frac{\mathrm{d}n}{\mathrm{d}d} = \nu\mathcal{N}(\Sigma) - \gamma n^2. \tag{3.13}$$

Here Σ denotes the supersaturation far off the droplets, $\nu\mathcal{N}(\Sigma)$ is a supersaturation dependent nucleation rate and γ is a collision probability. Integration of the evolution equation for the supersaturation based on (3.9) together with (3.13) yields a limit cycle in the phase separation dynamics. Vollmer et al. [130] show that a nucleation rate depending on the supersaturation, removing of droplets by coalescences and a coupling of the droplet number density to the supersaturation are the essential ingredients for the oscillations. Benczik and Vollmer [15] considered a reactive flow model with continuously ramped temperature and a chaotic advection field to investigate oscillatory phase separation numerically. Both models are too simplified to predict the time scale for the oscillation period observed in the experiments [8, 128, 130]. In the experiment, a convective flow is observed, so the diffusion equation (3.9) is coupled to the Navier-Stokes-Equations, which was discussed by Cates et al. [33]. We now move on to the description of real binary fluids, focussing on the model system that we chose for our experimental investigations.

3.3 Binary Fluids: Real Systems

Oscillations in the demixing process of binary mixtures have been observed in a variety of systems like methanol/hexane, polystyrene/cyclohexane, water/lutidine and water/butoxyethanol (confer section 3.1.1). They all differ in their exact physical and chemical properties, especially in the form of their phase diagram. The free energy of a binary fluid has several contributions, including binding energy, mixing entropy and rotational entropy [133]. Each of these terms has a different temperature dependence. In real physical systems, the free energy is therefore more complicated than assumed in the Φ^4-model. Both upper or lower critical temperatures can be observed in binary fluids. In figure 3.5 we show the phase diagram of the system water/butoxyethanol, which was studied in the experiment described in section 3.1.1. It shows a miscibility gap which forms above 48°C, gets wider up to about 80°C and then closes again. The phase diagrams of binary fluids are in general not symmetric in Φ, so more terms have to be added to describe the phase diagram than in the Φ^4-model. We now introduce the model system that we chose for our experimental studies.

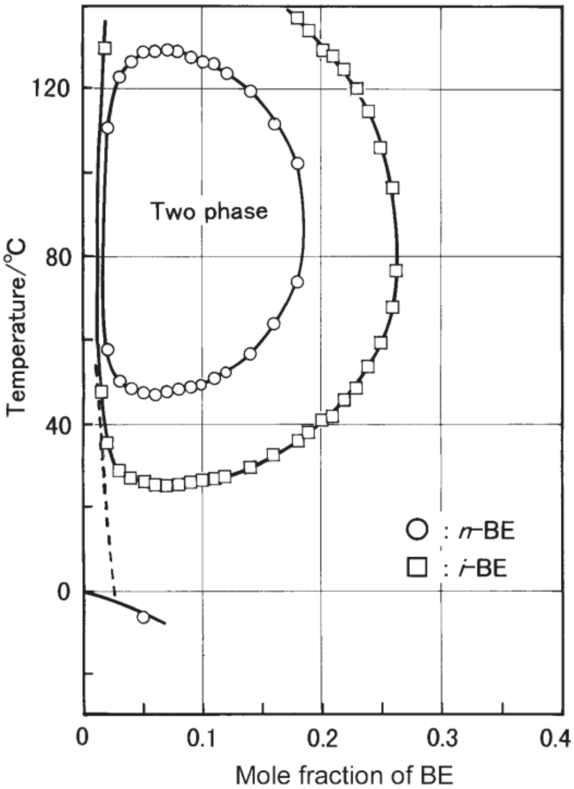

Figure 3.5: Phase diagram of water/butoxyethanol, taken from [84]. The lower critical temperature of aqueous solutions of isobutoxyethanol is slightly above room temperature, being very convenient for experimental procedures. The lower critical temperature of the water/n-butoxyethanol mixture is higher (at 48°C). The system also shows an upper critical solution temperature. When plotting in terms of the mole fraction, the phase diagram is quite asymmetric.

3.3.1 Model System: Water/Isobutoxyethanol

For visualizing the droplets in the experiment, we decided to use fluorescence after preliminary tests on visualization based on droplet reflection patterns were not promising. Most fluorescent dyes solve in organic phases. Therefore it is the easiest to use a binary fluid with an organic and a polar liquid. One example is the water/butoxyethanol system already used by Vollmer et al. [128], which is cheap and easy to handle. We find that the fluorescent dye nile red solves in butoxyethanol but not in water. Additionally the fluorescence is quenched by the water molecules [50]. Hence we get a good contrast in the fluorescence images of water/butoxyethanol mixtures. The only shortcoming is the relatively high critical temperature of 48℃. By choosing the derivate isobutoxyethanol instead (see figure 3.5 from [84]), the experiments can be performed close to room temperature. This allows for unattended automated operation without significant evaporation of cooling water. Using a system with an upper miscibility gap has the advantage that the sample can be prepared and stored at room temperature without danger of demixing before the experiment starts.

The phase diagram of a water/isobutoxyethanol mixture was carefully measured (cf. figure 3.6) by Rohloff with my supervision, analyzing turbidity changes during fast linear temperature ramps. A detailed description can be found in Martin Rohloff's diploma thesis [96, pp 16]. The compositions of the left (Φ_l) and right branch (Φ_r) were fitted by sixth and fourth order polynomials, respectively. The mean composition and the composition

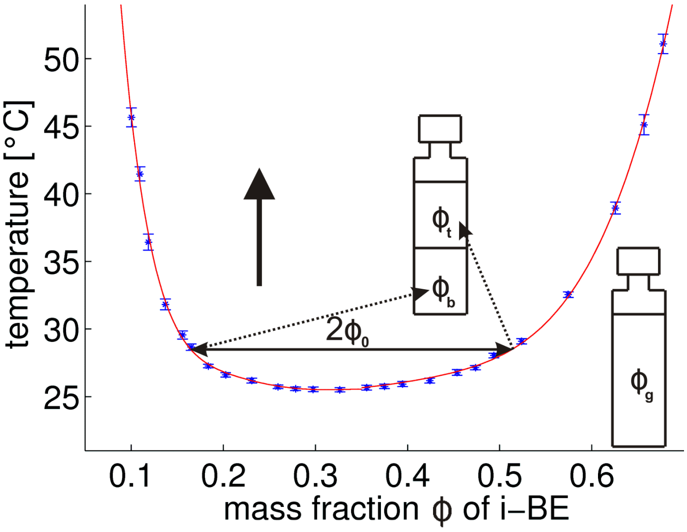

Figure 3.6: Phase diagram of water/isobutoxyethanol. The critical temperature was measured to be 25.51 ± 0.03℃, the critical mass composition is 0.310 ± 0.004 [96, p 19]. The left branch of the binodal is fitted by a sixth order polynomial, the right one by a fourth order polynomial. For temperatures below the binodal, the system is in one single phase with composition Φ_g. For slow temperature changes, the compositions of the bottom Φ_b and the top phase Φ_t follow the left and the right branch of the binodal, respectively.

difference are defined by

$$\bar{\Phi} = \frac{\Phi_r + \Phi_l}{2} \quad \text{and} \tag{3.14}$$

$$\Phi_0 = \frac{\Phi_r - \Phi_l}{2}. \tag{3.15}$$

The phase diagram (figure 3.6) is measured for mass fractions. Using the temperature and composition dependent density of the two phases (see section 3.A.2), mass fractions are converted into volume fractions [96, p. 61].

3.3.2 Driving the System

3.3.2.1 Driving Parameters

For real phase diagrams characterized by the compositions Φ_l and Φ_r of the left and the right branch, respectively, the definition of the normalized composition (3.5) has to be replaced by

$$\varphi \equiv \frac{\Phi - \bar{\Phi}(T)}{\Phi_0(T)}. \tag{3.16}$$

In the calculation of the time derivative of the normalized composition, a second driving term ζ appears due to the shift in the average composition $\bar{\Phi}$ [8]

$$\zeta \equiv \frac{1}{\Phi_0(T)} \frac{\partial \bar{\Phi}(T(t))}{\partial t}. \tag{3.17}$$

The diffusion equation (3.9) is extended to

$$\frac{\partial \varphi}{\partial t} = \nabla \left[\frac{D}{2}(3\varphi^2 - 1)\nabla\varphi \right] - \frac{D}{2}\delta^2 \nabla^4 \varphi - [\zeta + \xi_0 \varphi]. \tag{3.18}$$

Having chosen a binary system with an approximately symmetric phase diagram for volume or mass compositions (see figure 3.6), the driving due to the increasing width of the miscibility gap is the dominant term. In section 3.6.2.2 we show that the driving parameter ξ_0 (3.7) can be interpreted as the rate of droplet volume production in the whole sample. There we identify

$$\xi_l \equiv \frac{1}{2\Phi_0} \frac{\partial \Phi_l}{\partial t} \tag{3.19}$$

$$\xi_r \equiv \frac{1}{2\Phi_0} \frac{\partial \Phi_r}{\partial t} \tag{3.20}$$

as the rate of droplet volume production in the bottom and in the top layer, respectively.

3.3.2.2 Temperature Ramp

For the temperature protocol in the experiment, we calculate three different temperature ramps. They are defined by keeping either ξ_0, ξ_l or ξ_r constant. Auernhammer et al. [8] showed that this type of temperature ramps is a good choice for observing a large number of oscillations during one temperature ramp. In figure 3.7(b) we show that keeping ξ_0 constant implies only a small drift in the other two driving parameters ξ_l and ξ_r. To calculate the temperature ramp, we apply the chain rule of differentiation to equation (3.7)

$$\xi_0 = \frac{1}{\Phi_0}\frac{\partial \Phi_0(T(t))}{\partial t} = \frac{1}{\Phi_0}\frac{\partial \Phi_0(T)}{\partial T}\frac{\partial T}{\partial t}. \tag{3.21}$$

Inversion of (3.21) with finite differences for $\frac{\partial T}{\partial t}$ yields

$$T(t+\delta t) = T(t) + \frac{\xi_0 \Phi_0(T(t))}{\frac{\partial \Phi_0(T)}{\partial T}(t)}\delta t. \tag{3.22}$$

Equation (3.22) is integrated with 10000 uniformly distributed time steps in the range $[t_0, t_{\mathrm{end}}]$ chosen such that $T(t_0) = 25.8°\mathrm{C}$ and $T(t_{\mathrm{end}}) = 50.0°\mathrm{C}$ [96]. The result is plotted in figure 3.7(a). Note that for two thirds of the ramp the temperature does not change by more than 2 K. The raise of the temperature is faster than an exponential. In fact, a phase diagram with the form of a parabola or a scaling with a higher even power in Φ_0 would give exponential temperature ramps. To compare measurements with different driving rates we express time in units of the ramp duration t_{end}

$$\tau \equiv \frac{t}{t_{\mathrm{end}}}. \tag{3.23}$$

To conduct measurements in both layers of the sample, the position of the meniscus separating the layers has to be known.

3.3.3 Position of the Meniscus

In general, the two equilibrium phases have different densities. The phase with the lower density forms a top layer, the other one a bottom layer separated by a meniscus. The volume flux between the phases leads to a change of the position of the meniscus between the two layers. For the relative height of the bottom layer we define

$$\lambda \equiv \frac{\Lambda_{\mathrm{bot}}}{\Lambda_{\mathrm{bot}} + \Lambda_{\mathrm{top}}} \tag{3.24}$$

where Λ_{bot} and Λ_{top} denote the absolute height of the bottom and the top layer, respectively. According to the lever rule of binary fluids, the material that is put into the sample

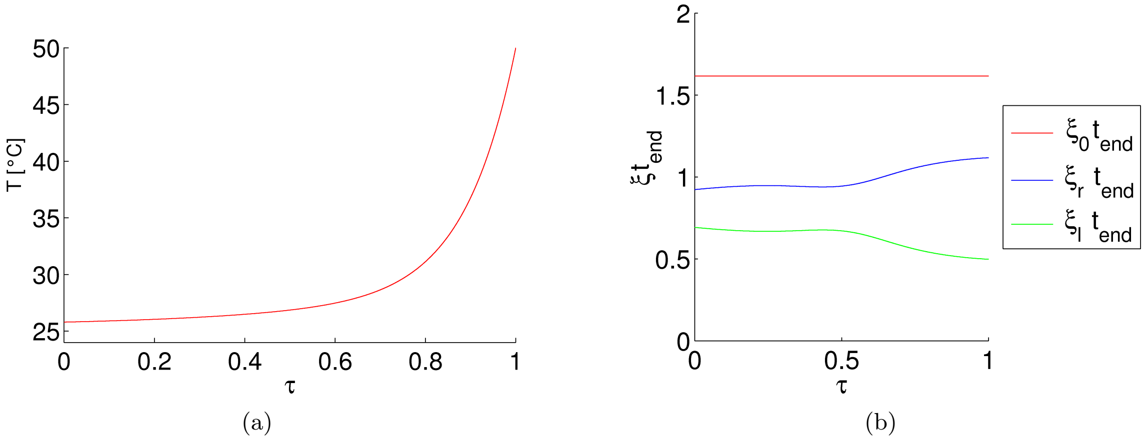

Figure 3.7: (a) Temperature ramp for the water/isobutoxyethanol system. The temperature is varied between 25.8°C and 50°C. The time scale is expressed in units of the ramp duration t_{end}. The driving ξ_0 is kept constant. Note that for two thirds of the ramp the temperature does not change by more than 2 K. (b) For the temperature ramp shown in (a) the time evolution of the driving parameters is shown. The driving parameter ξ_0 is chosen to be kept constant. Due to the small asymmetry of the phase diagram, $\xi_{\mathrm{r,l}}$ is changing slowly with time. The figure is adapted from [96].

with the global composition $\varPhi_{\mathrm{g}}$ is divided between the two layers (compare figure 3.6)

$$(\varLambda_{\mathrm{bot}} + \varLambda_{\mathrm{top}})\varPhi_{\mathrm{g}} = \varLambda_{\mathrm{bot}}\varPhi_{\mathrm{bot}} + \varLambda_{\mathrm{top}}\varPhi_{\mathrm{top}} \tag{3.25}$$

where $\varPhi_{\mathrm{bot}}$ and $\varPhi_{\mathrm{top}}$ denote the compositions of the bottom and the top phase, respectively. Equation (3.25) can be rearranged to

$$(\varLambda_{\mathrm{top}} + \varLambda_{\mathrm{bot}})(\varPhi_{\mathrm{g}} - \varPhi_{\mathrm{top}}) = \varLambda_{\mathrm{bot}}(\varPhi_{\mathrm{bot}} - \varPhi_{\mathrm{top}}). \tag{3.26}$$

The compositions of the two layers depend on temperature T. The position of the meniscus can be related to the volume compositions of the two phases

$$\lambda(T) = \frac{\varPhi_{\mathrm{g}} - \varPhi_{\mathrm{top}}(T)}{\varPhi_{\mathrm{bot}}(T) - \varPhi_{\mathrm{top}}(T)}. \tag{3.27}$$

In the measurements, it is advantageous to run the experiments with global compositions $\varPhi_{\mathrm{g}}$ where the change of λ, the position of the interface, is minimal. At each run of the experiment, we want to look at only one of the two layers. If the interface moves through the field of view of the camera, the analysis of the image data is made even more difficult.

3.3.4 Material Properties of Binary Fluids

For the physical description of phase separation, a number of material properties is important. They all depend on temperature and on the position of the system within the phase diagram. For the case of slow temperature ramps, the system closely follows the binodal, so the properties at the binodal are most relevant for our data analysis. The temperature dependence of the material properties of our model system water/isobutoxyethanol is collected from literature [6, 39, 41, 43, 81, 111, 134] and interpolated. A detailed description is given in the appendix 3.A. In the following, we summarize the typical temperature dependence of some material properties of binary fluids, that are relevant for the understanding of the phase separation dynamics.

- **Density:** The density difference of the two phases is to leading order proportional to the composition difference of the two phases. A linear interpolation of the densities of the components hast to be corrected by the molar excess volume (order of 20% for the density difference). The molar excess volume denotes the difference between the sum of the volumes of the two single components and the total volume of the mixture. Also the thermal expansion of the two components has to be taken into account.

- **Viscosity:** The viscosity of liquids depends roughly exponentially on temperature [7]. However, there are corrections to the exponential dependence. Most strikingly, there is a significant excess viscosity for binary mixtures close to the critical point. Typically the viscosity of binary mixtures is about 15 to 20% higher than the interpolation between the component viscosities for a considerable range of compositions [32]. This can be explained by an analogy to colloid solutions: Inhomogeneities of composition, density and local viscosity result in an enhanced shear viscosity [48].

- **Interfacial Tension:** As we discussed in section 3.2, the interfacial tension increases with the difference of the compositions of the two phases and vanishes at the critical point.

- **Diffusion:** The diffusion coefficient (see section 3.2.2) for the two phases converges to the same value at the critical point. It is decreasing, when a mixture of a given composition approaches the binodal (see equation (3.9)), and it also decreases on the binodal towards the critical point [111].

3.4 Experiment

3.4.1 Experimental Setup

Measurement Cell and Temperature Control The sample is contained in a fluorescence cell $(10 \times 10 \times 33)$mm 117.100F-QS made by Hellma GmbH. For studying the influence of the geometry, also cells with $(4 \times 10 \times 33)$mm and $(1 \times 10 \times 33)$mm as well as $(10 \times 10 \times 110)$mm were ordered. The measurement cell is mounted with micrometer srew adjusted shift meachanisms to controll the position in all three directions. It is immersed into a water bath with controlled temperature (see Fig. 3.8). An immersion cooler Haake EK20 is cooling with constant power, and a temperature control module Haake DC30 is heating the water bath to a preset temperature. Additionally the temperature of the water near the sample is measured with a PT100 temperature sensor. The temperature is controlled with an accuracy of 15mK (standard deviation of PT100 signal). Using a magnetic stirrer the sample is mixed before each experimental run.

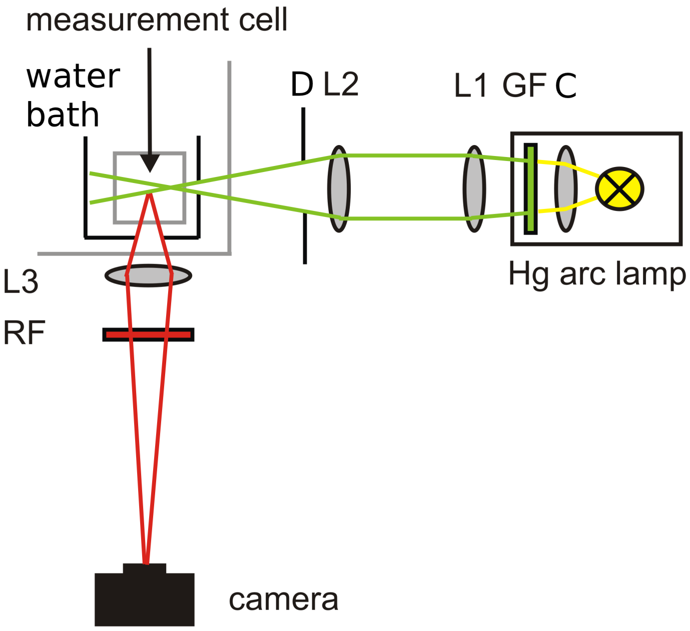

Figure 3.8: Sketch of the experimental setup, top view. The light of a short arc Hg vapor lamp is collected by a collimator lens (C) and parallelized by a spherical lens (L1). A cylindrical lens (L2) forms a light sheet which is cut by a diaphragm (D) and a line aperture (300 μm width) directly in front of the sample cell. The light sheet illuminates a plane of the binary mixture, a green filter (GF) selects the wavelength range suitable for excitation of the dye. The emission of the fluorescently labeled phase passes a red filter (RF) and is projected onto a 5 MP CCD camera chip. The sample cell is mounted in a water bath with controlled temperature.

Light Source Finding a proper light source for the illumination of the sample turned out to be quite difficult. A laser light sheet is not suitable for illumination since it is unidirectional and the two phases are not index-matched. Each droplet acts as a little lens which focuses and diffracts the parallel laser light sheet. After passing a short distance of the sample, the droplets have transformed the uniform light sheet into a pronounced stripe pattern, which illuminates the droplets very inhomogeneously. The stripe pattern is difficult to filter because it evolves in time and the stripe widths are equal to the diameters of the droplets that shall be detected. Secondly, a reliable light source is required which can be operated safely without human supervision, as some measurements take more than 30h nonstop. This criterion disqualifies powerful laser systems.

However, to get a good signal from the fluorescently labeled phase, a very bright light source is required. Also, the light has to be focussed on a small measurement volume (less than a cube millimeter). Additionally, the illumination must be quite homogeneous and the divergence of the light sheet should not be very large.

Basic optical principles tell that the luminance of a light source is at best a conserved quantity in geometrical optics and cannot be increased. It is the power that an area emmits at a certain angle. If the desired divergence angle is small but the light intensity shall be high, a light source with a bright but small light emmitting region has to be chosen. This request disqualifies LEDs and cold light sources, which we used successfully for the illumination of the breath figures. Last but not least, the light source must have a high intensity at one of the maxima of the absorption spectrum of the fluorescent dye.

Finally, a mercury short arc lamp (LOT-Oriel, 100W) with a bright light emitting spot (less than a cube millimeter) gives the best results. It provides a high light intensity, which is diffuse enough to avoid pronounced stripes (figure 3.9(a)). With a careful chosen set of lenses, the light can be focussed on the measurement volume with a quite homogeneous light intensity.

Illumination Optics A sketch of the optical components is given in figure 3.8. The light is collected by the collimator lens (C) and a bandpass filter (GF) selects the green emission lines (546 and 577/579nm) for the excitation of the fluorescent dye. The spherical lens (L1, f=200mm) forms a parallel light beam. The cylindrical lens (L2, f=80mm) focuses the light normal to the focal plane of the camera increasing the intensity even further. A spherical diaphragm (D) allows to adjust the amount of light manually. With a narrow slit of 300μm width directly in front of the measurement cell a vertical light sheet is formed. The measurement cell is covered by black apertures to shield stray light. The positions of the light bulb and the lenses has to be adjusted in all three directions to achieve a homogeneous illumination with maximum intensity in the full measurement volume.

Imaging The fluorescent light from the illuminated plane of the sample is projected by a f=35mm objective (L3) to the chip of a BM-500CL monochrome progressive scan CCD camera. Choosing a long tube (about 20cm) between camera and objective enables a high magnification of the field of view. The camera takes 2058×2448 pixel images with a maximum frame rate of 15Hz, covering 1.3mm×1.5mm of the sample (1.6 pixel/μm). With a long-pass filter (RF, edge 594nm) the excitation light is filtered.

Control The camera, temperature control and magnetic stirrer are connected to a computer. Also the lamp can be switched on and of remotely. Measurements are fully automated using a LABVIEW program.

3.4.2 Experimental Procedure

After cleaning the measurement cell, it is filled with the binary mixture at a composition close to the critical composition. For having a small variation of the meniscus position, we use the composition $\Phi = 0.32$, where the change of the relative bottom layer height λ (3.24) has a minimum. The fluorescent dye is dissolved in isobutoxyethanol. A stirring bar is inserted and the cell is sealed with teflon. It is mounted in the temperature bath and stirred with 1500 rpm for one hour in the one phase regime at 24°C. It was checked visually that after one hour the sample is mixed completely if not more than 2ml are filled into the cell. The stirring bar does not fit into thin cells. For filling levels higher than 2cm the stirrer is not able to mix the sample completely. Hence in these cases, mixing is carried out by shaking manually before inserting it into the water bath.

After this preparation procedure the temperature is set 25.8°C, which is 0.3K above the critical point. While the sample is demixing and the layers with the meniscus in between are forming, the illumination and the camera are adjusted. We control the position of the camera to measure at a distance 0.3mm from the wall. The horizontal position is centered to the cell and the vertical position is measured. The sample is kept for four hours at constant temperature without stirring. In this condition almost all droplets are sedimented and the sample is at equilibrium.

The lamp is switched on and after 10 min we apply a precalculated temperature protocol (see section 3.3.2.2) where the thermodynamic driving rate ξ_0, ξ_l or ξ_r is kept constant. To implement the temperature scan, the temperature of the thermostat is set with a rate of 1 Hz according to the calculated temperature ramp. Once the end temperature is reached (50°C), the lamp is switched off, and the sample is cooled to 24°C and stirred for one hour. Then the next temperature ramp can be started. The measurement procedure is fully automated, up to 20 subsequent measurements have been taken with one sample. The total measurement time is limited by bleaching of the dye which is severe after about 20h exposure, depending on dye concentration and sample volume. The diaphragm and the line aperture (see figure 3.8) limit the exposure to a sheet which contains the measurement volume.

Having described our experimental setup and the measurement protocol, we move on to describe the image processing algorithm that we developed for the analysis of our data.

3.5 Image Processing and Droplet Tracking

3.5.1 Introduction

To analyze the data that we obtained with our experimental setup described above, we developed a particle tracking algorithm which uses the droplets as marker particles to measure the flow field. Droplet positions and radii are detected simultaneously. The radius can therefore be used as a criterion to identify droplets in subsequent images. Assuming Stokes law [13, p. 234] the sedimentation velocity can be calculated from the droplet radius. The droplet velocity is decomposed into sedimentation velocity and advection by the flow. By subtracting the sedimentation velocity from the droplet velocity, the advection of *all* droplets can be used to measure the flow field. With the advective flow field and the sedimentation velocity of each droplet, its position in the next frame can be predicted and compared to the image.

We could not simply use existing droplet detection or tracking algorithms. Image processing algorithms always have to be specifically adapted to the type of images and the structure that shall be detected. Insight about the properties of the studied system as well as the specific questions that shall be addressed by processing the data determine the bases for the development of the image processing algorithm. For example, peculiarities of the illumination that is used have to be accounted for. In our case, taking the sedimentation velocity of the droplets based on the detected droplet radius and the density difference and viscosity at the temperature present when taking the frame is essential for reliable droplet tracking even with low frame rates.

Previous studies have extensively used particle tracking velocimetry as a measurement technique to investigate turbulent flows carrying small particles ([65, 72, 74, 88]). To that end monodisperse tracer particles are added to the fluid whose position is detected by image processing of high speed camera data. While this procedure is followed successfully for monodisperse particles in single-phase flows, it is not easily applicable for measuring flow patterns in demixing binary systems.

Tracer particles cannot be added as they would act as nucleation centers, and therefore affect the droplet number density. Furthermore, colloidal particles aggregate on the interfaces and change the growth and coalescence rate, as [118] have shown. For a review of the stabilizing effect of colloidal particles in emulsions see [22] and [9].

There also is a broad range of acoustic/electro-acoustic and optical techniques for the measurement of droplet size distributions, an overview given by [73]. Several laser based techniques measure chord lengths that have to be transfered into droplet size distributions ([62]), e.g. focus beam reflectance measurement (FBRM, see e.g. [98]) or optical reflectance measurement (ORM, see e.g. [70]). However, [71] and [107] have shown that these techniques give inaccurate results for liquid/liquid dispersions in comparison to image analysis of in situ microscope imaging.

In the following we describe a particle detection and tracking algorithm for polydisperse

sedimenting particles [67] that was developed in the course of this thesis. Radii and positions of the droplets are detected simultaneously. The algorithm to process the single images was programmed by myself. The algorithm for the calculation of flow fields and the tracking of droplets was developed by Martin Rohloff in his diploma thesis under my supervision [96].
The first section 3.5.2 describes the image processing algorithm which detects droplets in separate images. In the next step the flow field is estimated, as described in section 3.5.3. Then the droplets are tracked through a series of images (section 3.5.4). Finally the velocity field is recalculated based on the droplet trajectories. This procedure allows us to sort out artifacts (caused e.g. by dirt or overlaps of droplet images) of the image processing, and to determine Lagrangian particle velocities. In the final section 3.5.5, we validate the applicability of the assumptions used in the algorithm and the analysis. The image processing is done with the MATLAB Image Processing Toolbox. The data (typically 20000 images per measurement) is processed on a computer cluster. For simplicity we restrict our description to the detection of the fluorescently labeled droplets in the bottom phase. By inverting the images and the direction of gravity the same algorithm can be used for the dark droplets detected in the top phase.

3.5.2 Processing of Single Images

3.5.2.1 Preprocessing

In a first step, dark spots caused by dirt on the camera chip are removed with a flat field correction. Further, the image is Fourier filtered and the contrast is optimized. To reduce the horizontal stripes (illumination from the right) produced by the light dispersion of the droplets a high pass filter (Gaussian filter with width 5 in horizontal and 200 in vertical direction) is applied. For reducing the noise, a low pass filter (isotropic Gaussian filter, $\sigma = 100$) is applied. In figure 3.9, a raw image and a preprocessed image of fluorescent i-BE-rich droplets in the denser water-rich bottom phase are shown. For high droplet densities, there is a significant number of overlaps of droplet images. Therefore we need special algorithms to take care of this for detection means.

3.5.2.2 Droplet Detection

The droplets are detected in the preprocessed image using two strategies. The first relies on thresholding the image, the other uses marker-controlled watershed segmentation. The first strategy is visualized in figure 3.10 giving an example. All pixels darker than a threshold level (Fig. 3.10(a)) are identified as background (Fig. 3.10(b)). Isolated background regions are deleted. Then, for each pixel the distance to the background is calculated (Fig. 3.10(c)). Local maxima in this distance map correspond to droplet centers, their distance to the background being their radius (Fig. 3.10(d)). This procedure is carried out twice with two thresholds, one being better for finding big droplets, the other for small droplets.

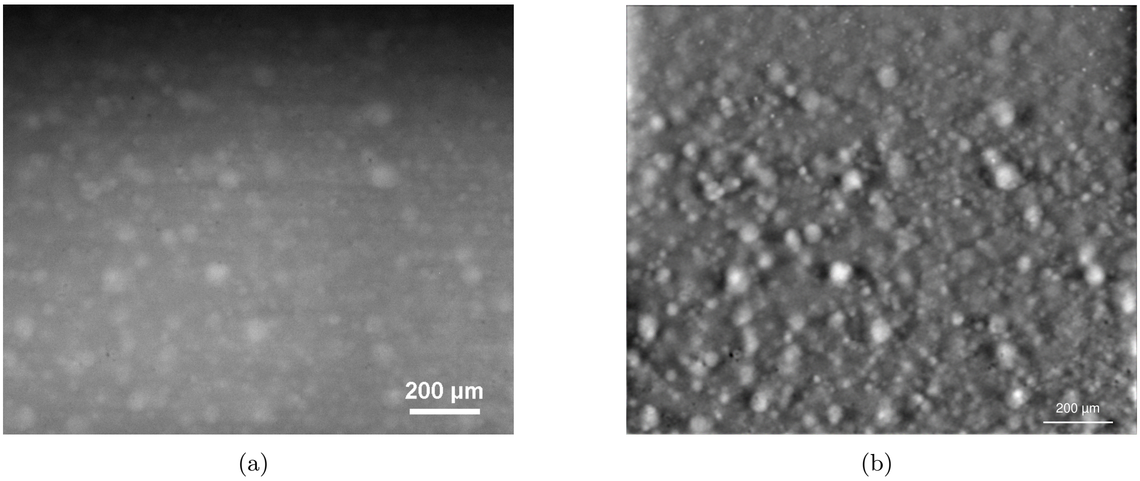

(a) (b)

Figure 3.9: (a) Raw image and (b) preprocessed image of i-BE-rich droplets in the water-rich bottom phase with $\xi = 1.05 \cdot 10^{-5}$s at 25.98 ± 0.02°C. Horizontal stripes and the vertical intensity gradient are removed by Fourier filtering.

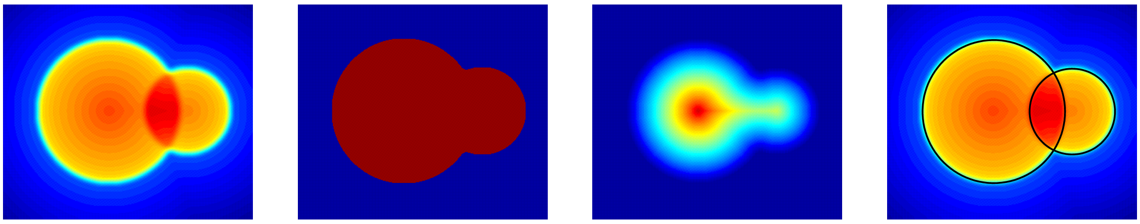

(a) (b) (c) (d)

Figure 3.10: Sketch of distance based image segmentation. (a) False color plot of two overlapping images of droplets. (b) Thresholded image. (c) Distance from background. (d) Detected droplets based on local maxima of distance.

The second strategy is based on the marker-controlled watershed segmentation algorithm proposed by [55] pp. 422. It is illustrated in figure 3.11. Extended maxima in the image (Fig. 3.11(a)) are used as marker for the droplets (Fig. 3.11(b)). Lines between these maxima as well as extended minima are markers for the background. With a sobel filter the intensity gradient in the image is calculated (Fig. 3.11(c)). The markers are imposed as minima on the gradient image upon which a watershed transform is operated. The watershed lines of the intensity gradient correspond to droplet edges. The markers are needed to avoid over-segmentation. Areas and centroids of the regions enclosed by the watershed lines are taken for the droplet radii and positions (Fig. 3.11(d)).
Using these two approaches, even small droplets on top of bigger ones and overlapping

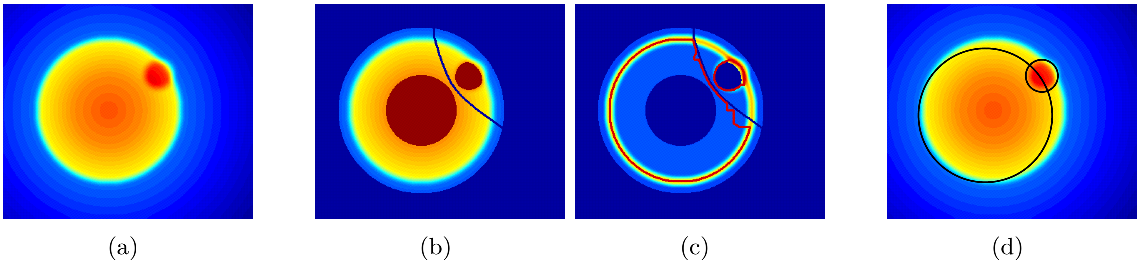

Figure 3.11: Sketch of watershed image segmentation. (a) False color plot of two overlapping images of droplets. (b) Bright extended maxima mark droplets, lines in between and dark regions mark background. (c) Markers are imposed as minima (blue) on gradient image. Watershed lines follow droplet edges (red). (d) Detected droplets (black) based on regions enclosed by watershed lines.

images of droplets can be resolved. On the other hand, some droplets are found multiple times and some imaging artifacts are taken for droplets. If two droplets with radii r_1,r_2 are detected close to each other (centroid distance less than one radius) with almost the same radius (ratio $0.7 < r_1/r_2 < 1.4$), they are considered as two detections of the same physical droplet.

3.5.2.3 Matching to Image

Not fully compensated dirt on the camera chip, overlaps of droplet images or unsharp droplet images can cause false detections. Hence, a second step is implemented to distinguish droplets from artifacts and the estimates of the droplet radius r and position (x,y) [pixels] are compared to the preprocessed image. As characteristics of droplets in the image, we consider them being brighter than their environment and having a circular intensity gradient at the edge (figure 3.12). A match function m is defined as

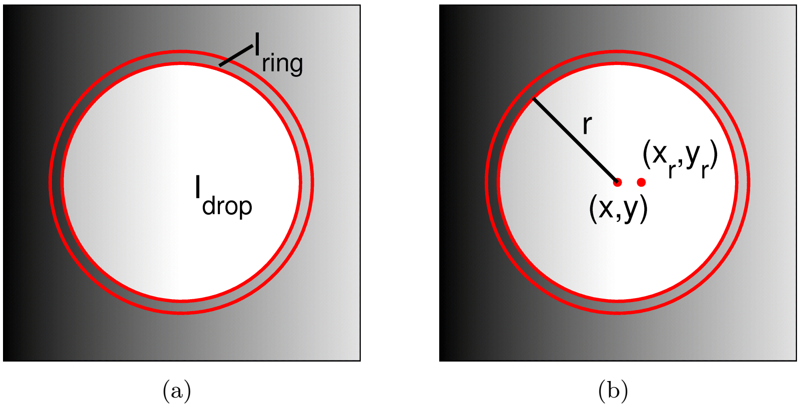

Figure 3.12: Definition sketch for the match function. (a) I_{drop} denotes the mean intensity of the droplet, I_{ring} the intensity of a ring around it. (b) (x,y) is the centroid of the droplet with radius r, (x_{r},y_{r} is the intensity weighted centroid of the ring.

$$m(x,y,r) = A(r)\left[I_{\text{drop}}(x,y,r) - I_{\text{ring}}(x,y,r)\right] \\ -B\frac{(x-x_{\text{r}})^2 + (y-y_{\text{r}})^2}{r^2} \tag{3.28}$$

where the radius r and the coordinates x, x_r, y and y_r are given in pixels. The difference between the mean intensity of the droplet $I_{\text{drop}}(x,y,r)$ and the mean intensity $I_{\text{ring}}(x,y,r)$ of a ring of 3 pixels width around it measures the intensity gradient at the droplet edge (figure 3.12(a)). By visual comparison of calculated droplet matches with the preprocessed images an empirical radius dependent prefactor $A(r) = 1/\left(30 + r^{1.3}\right)$ was determined. It ensures comparable matches for small and big droplets. Often small droplets are detected erroneously at the edge of big droplets. In this case, a little part of its halo is covering the dark background and the remaining part is covering the big droplet. The intensity weighted centroid of the halo (denoted as x_{r} and y_{r}) is calculated and compared to the droplet position (figure 3.12(b)). The deviation accounts for this asymmetry and reduces the value of the match. It is weighted with the empirical prefactor $B = 3$. For every droplet found in the droplet detection step, the match with the image is calculated. By varying radius and position of the droplet a local maximum of the match is found. All droplets with a match bigger than 0.08 are used for further analysis.

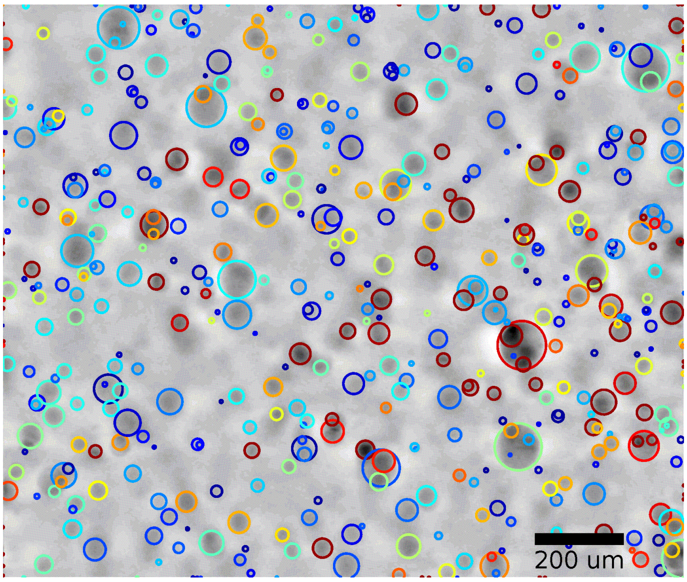

Figure 3.13: The droplets which are detected by processing the image (without tracking) are superimposed as circles on the preprocessed image. The color encodes the match of the detection to the image: red denotes a good match, blue a bad match.

For illustration the droplets detected by processing a single image are shown in figure 3.13. The color encodes the match of the detection to the image: red denotes a good match, blue a bad match. Many droplets are detected reliably. However, some droplets are missing and artefacts are taken for droplets. This motivates further processing of the data. A final step to increase the reliability of the measured size distribution takes advantage of the time information of image sequences. Tracking the droplets allows to sort out unphysical trajectories of artifacts and to find undetected droplets in the image using its past or future trajectory. To implement this information in section 3.5.4.3 we must evaluate the flow field and the droplet trajectories in the flow.

3.5.3 Calculation of Flow Field

3.5.3.1 Identification of Droplets in Consecutive Images

Typically droplets with radii $4\mu\text{m} < r < 40\mu\text{m}$ are detected. While small droplets ($r < 10\mu\text{m}$) closely follow the flow, large droplets ($r > 20\mu\text{m}$) are mainly driven by their buoyancy and do not qualify as tracers. They sediment towards the interface due to the density difference of the two phases. In a Lagrangian frame, co-moving with the surrounding fluid, the sedimentation velocity u_{sed} amounts to the Stokes velocity for a sphere of radius r, which is [13, p. 234]

$$u_{\text{sed}} = \frac{2}{9}\frac{\varDelta\rho\, g r^2}{\eta}. \tag{3.29}$$

Here $\varDelta\rho$ denotes the mass density difference between sphere and fluid, g the gravitational acceleration, and η the dynamic viscosity of the fluid. Hence, the droplet velocity u_{drop} can be split into a sedimentation and an advection term

$$u_{\text{drop}}(x,y,r,t) = u_{\text{sed}}(r) + u_{\text{flow}}(x,y,t). \tag{3.30}$$

We check the validity of this ansatz in section 3.6.2.3. To track droplets the corresponding images of droplets in consecutive frames must be identified. To this end, the velocity field of the previous time step $u_{\text{flow}}(x,y,t-\delta t)$ is taken as an initial guess for $u_{\text{flow}}(x,y,t)$. For each droplet found in one image the position in the next image is predicted using equation (3.30). The prediction is compared to the droplets found in the image, and the droplet pair with the closest distance between prediction and actual position and with similar radii is identified as one physical droplet. In figure 3.14 the droplets in the image are marked with red circles and the corresponding droplets in the next image with green circles. The procedure used to determine the flow field, which is indicated by the arrows, is lined out in section 3.5.3.2. Subsequently in section 3.5.4 we describe details of the scheme adopted for finding particle trajectories.

3.5.3.2 Determine the Flow Field

In order to calculate the Eulerian flow field $u_{\text{flow}}(x,y,t)$ the image is sampled by an equidistant mesh with 25×20 grid points. The grid distance is about $60\mu\text{m}$, which is in the order of the droplet distance. The correlation length of the flow field is about $200\mu\text{m}$, so the grid can resolve the flow structures. A flow correlation time of 30s allows for small frame rates (order of 1Hz). By subtracting the sedimentation velocity u_{sed} from the droplet velocity

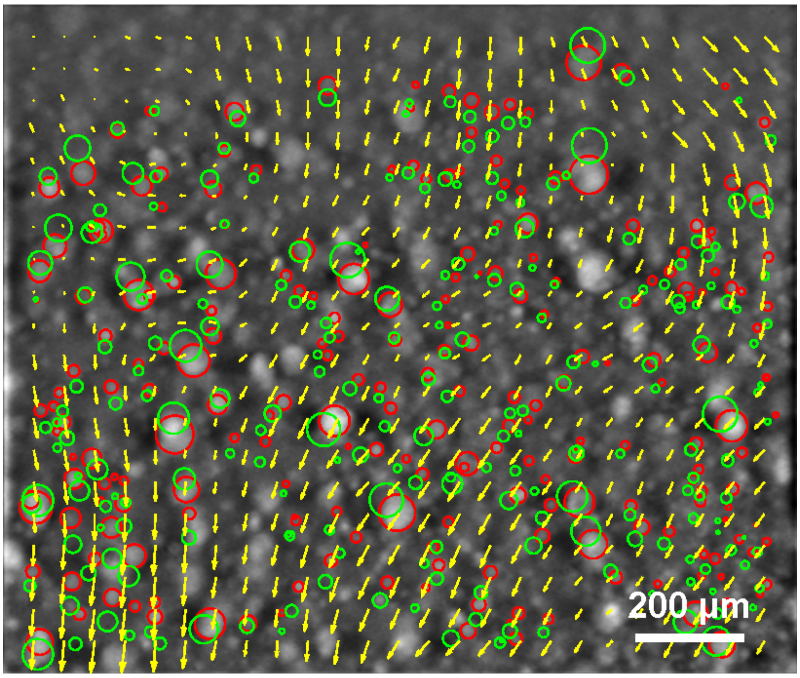

Figure 3.14: Fluorescently labeled droplets in the bottom phase (Fig. 3.9(b)). The arrows correspond to the flow field. Red circles mark the droplets found in the image and green circles their position and radius in the next image.

u_{drop} the flow contribution u_{flow} can be calculated: The advection of the N droplets k in each mesh cell (i) is averaged, incorporating with half weight the M droplets of neighboring cells (ij):

$$
\begin{aligned}
u^{(i)}_{\mathrm{flow}} = \frac{1}{N+M/2}[&\sum_{k=1}^{N}({}^k u^{(i)}_{\mathrm{drop}} -{}^k u^{(i)}_{\mathrm{sed}}) \\
&+\frac{1}{2}\sum_{k=1}^{M}\sum_{j=1}^{4}({}^k u^{(ij)}_{\mathrm{drop}} -{}^k u^{(ij)}_{\mathrm{sed}})]
\end{aligned}
\tag{3.31}
$$

3.5.3.3 Smoothing of Flow Field

The advection field $u^{(i)}_{\mathrm{flow}}$ is smoothed with a weighted average of next-nearest neighboring cells to eliminate unphysical discontinuities.

$$
\bar{u}^{(i)}_{\mathrm{flow}} = \frac{1}{4}u^{(i)}_{\mathrm{flow}} + \underbrace{\frac{1}{8}\sum_{j=1}^{4} u^{(ij)}_{\mathrm{flow}}}_{\text{next neighbours}} + \underbrace{\frac{1}{16}\sum_{j'=1}^{4} u^{(ij')}_{\mathrm{flow}}}_{\text{next-nearest neighbours}}
\tag{3.32}
$$

In figure 3.14 a smoothed advection field is shown together with the matched droplets. The Eulerian flow field is used to predict the droplet positions in the next image. Note that the spatial distribution of detected droplets is not homogeneous and some grid points can only be calculated by interpolation. For the subsequent analysis of the flow field only the grid points which are directly computed from droplet displacements are taken into account.

3.5.4 Particle Tracking

3.5.4.1 Forward Tracking

Now that the advection field and sedimentation velocities for each droplet found in the image at time t have been determined, the position at time $t + \delta t$ can be predicted. This prediction is matched to the image of $t+\delta t$ and a local maximum of the match is searched for. This procedure is illustrated in figure 3.15. Having determined the displacement from time t to $t + \delta t$, the advection field can be recalculated. In the next step, the positions of droplets tracked from image t to $t + \delta t$ plus all other droplets also detected in image $t + \delta t$ are predicted for the time step $t + 2\delta t$. They are compared to the droplets in image $t + 2\delta t$ and the procedure is repeated. The identified droplet pairs are sorted into trajectories, which contain the position and radius values for the different frames. Based on the trajectories, the flow field $u_{\text{flow}}(x,y,t)$ is recalculated according to the procedure described in section 3.5.3.2.

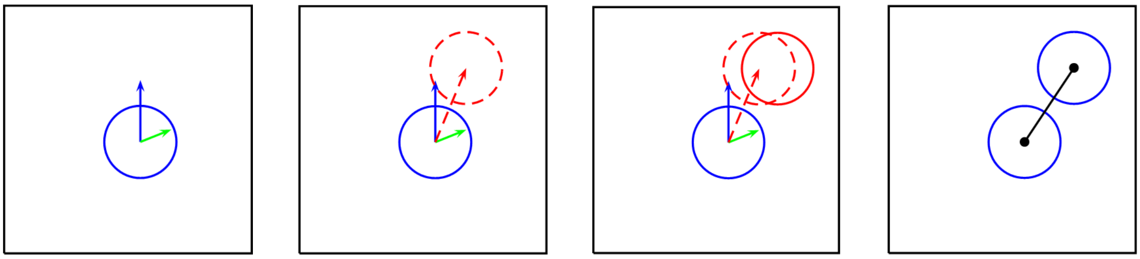
(a) (b) (c) (d)

Figure 3.15: Forward tracking: (a) Sedimentation velocity (blue, upward) and advection (green, 2 o'clock), (b) predict the next position (red dashed), (c) match the prediction to the next image (red solid) and (d) build trajectory (black).

3.5.4.2 Backward Tracking

The forward tracking result can be improved by subsequently tracking the droplets backwards in time. The positions of droplets at the beginning of the trajectories are predicted for the time step before and matched to the image (compare figure 3.16). The droplet is compared to the entries in the other trajectories to merge interrupted trajectories, and to suppress branching of trajectories. As yet, our tracking algorithm does not account for the collision of droplets.

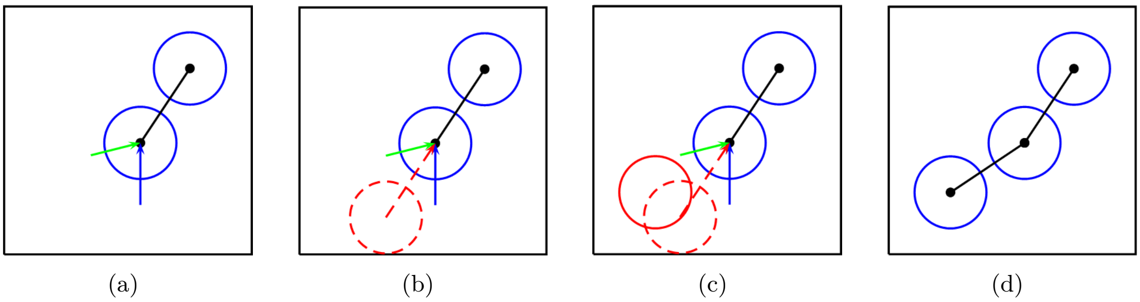
(a) (b) (c) (d)

Figure 3.16: Backward tracking: (a) Sedimentation velocity (blue,upward) and advection (green, 8 o'clock), (b) predict the previous position (red dashed), (c) match the prediction to the previous image (red solid) and (d) enlarge the trajectory (black).

3.5.4.3 Filtering of Trajectories

Trajectories shorter than three time steps are removed. Finally, all droplets which have moved by less than half the average advection velocity during the tracked time interval are deleted. Most likely, those spots are imaging artifacts. Eventually, the flow field is recalculated once more based on the enlarged and filtered trajectories in order to arrive at a consistent data set.

3.5.4.4 Depth of Measurement Volume

Having found the trajectories of droplets in the image plane, we need to now the depth of the measurement volume. To this end, a calibration pattern of black disk was printed with a laser printer on a transparency. It was glued at the front of the measurement cell, which was filled with a fluorescent mixture. The position of the camera was shifted in 50μm steps in the direction vertical to the image plane. We find that small patterns can only be seen when they are directly in the focal plane. Larger ones, however, can also bee seen when they are slightly off the plane. We therefore assume that the depth in which a droplet can be detected is to leading order proportional to the droplet diameter. The precise value of the proportionality prefactor is not known and may depend on the details of illumination or bleaching of the sample. For the analysis of the data, we use two times the diameter as the depth where a droplet can be detected. This is probably an upper limit for the measurement volume. With this assumption for the measurement volume, we get data for the droplet volume fraction which is consistent with the volume fraction expected to be created by the temperature drift. This is discussed in more detail in section 3.6.2.2 and shown in figure 3.20. Note that most of our results, namely the oscillation periods, the shape of the size distribution function and the scaling of droplet number and volume density do not depend on the precise value of the prefactor for the measurement depth.

3.5.5 Validation of the Algorithm

The accuracy and the limitations of the algorithm are discussed in great detail in the Diploma Thesis of Rohloff [96] and in [67]. Here we give only a short summary of the consistency checks that we performed in order to validate the performance of the tracking algorithm.

- **Visualisation of flow field:** The estimated flow field as well as the positions of droplets in the present and in the subsequent frame were plotted on top of the preprocessed image for different frames. One example is given in figure 3.14.

- **Visualisation of trajectories:** We created video sequences where the detected droplets and the trajectories are shown together with the preprocessed images. One example can be found in [96].

- **Visual comparison of images with size distribution:** We compared raw and preprocessed images with the droplet size distribution given by the algorithm. We checked that the features of the measured size distribution (e.g. the abrupt occurrence of droplets of about 9μm in the first few oscillations, broad distributions in the first few oscillations and narrow distributions in the end) can actually be identified in the raw data as well.

- **Droplet velocities:** We checked the validity of the assumption (3.30), that droplet velocities are the sum of the flow velocity and the Stokes velocity. This will be discussed in more detail in section 3.6.2.3.

- **Uncertainty in radius detection:** For each trajectory we calculated the standard deviation of the radius detected in the subsequent frames. Averaging over many trajectories we find that the error is about 20% for small droplets and saturates at 4μm for big droplets [67, 96].

- **Trajectory lengths:** We calculated the average duration of trajectories as a function of the radius, finding a roughly linear dependence [67, 96]. For droplets with a radius of 20μm we find typical trajectory durations of about 25s. Analysis of the flow fields gives typical horizontal velocities of about 3μm/s. Hence droplets may move $\mathcal{O}(75\mu\text{m})$ during their detection, which is consistent with our assumption for the depth of the measurement volume.

- **Velocity fluctuations:** We find a mean horizontal velocity of zero, whereas the mean vertical (negative in the bottom layer) and the root mean squared velocities in the horizontal and the vertical direction oscillate with the same periods as the size distribution does [67, 96].

- **Correlation length and time**: We checked that the typical correlation lengths (200μm) and times (30s) are well resolved by the grid for the flow field and the camera frame rate [96].

3.6 Evolution of the Droplet Size Distribution

In this section the results for our investigations of slowly demixing binary systems are presented. Some of the results were already presented in Martin Rohloff's diploma thesis [96] that was prepared under my supervision. Where appropriate, these results he presented are reproduced and discussed in a broader context. We analyze the evolution of the droplet size distribution, and reveal the mechanism which determines the oscillatory behavior of the system. An analytical model for the oscillation period is suggested and compared to the experimental findings.

3.6.1 Oscillatory Response of System on Driving

Oscillations of the specific heat capacity and the turbidity of binary mixtures under slow temperature ramps have been observed in many experimental works [8, 60, 130, 131]. Space-time plots of the turbidity indicate an oscillation of the droplet size distribution. To understand the origin of the oscillations, it is essential to investigate the evolution of the droplets size distribution.

3.6.1.1 Oscillation of Droplet Volume Density

Using the image processing algorithm described above we are able to measure the time dependence of the droplet size distribution. To visualize the oscillations we plot the volume fraction of droplets as a function of time (figure 3.17). The droplet volume fraction is proportional to the third moment of the droplet radius distribution

$$v \equiv \int_0^\infty n(r) \frac{4\pi}{3} r^3 \, \mathrm{d}r \tag{3.33}$$

with $n(r)$ denoting the density of droplets with radius r. It is a good quantity to measure as it does not strongly depend on the uncertainty in measuring small droplets.
The droplet volume fraction oscillates in both phases with slightly different oscillation periods. Both a remarkable increase of the oscillation frequency and a decrease of the oscillation amplitude can be observed in both phases. This was rather unexpected as the choice of the temperature ramp was intended to give a regular feedback of the system.

3.6.1.2 Oscillation of Droplet Size Distribution

To understand the origin of the oscillations, it is revealing to look at the evolution of the droplet size distribution. After tracking each individual droplet for at least three subsequent frames as described above, we get reliable data not only for big droplets but also for small ones with a radius bigger than 3μm. The evolution of the size distribution for the full measurement duration of 16h is shown in a false color plot in figure 3.18. In addition, figure 3.18 also shows the droplet volume distribution for 12 time bins per

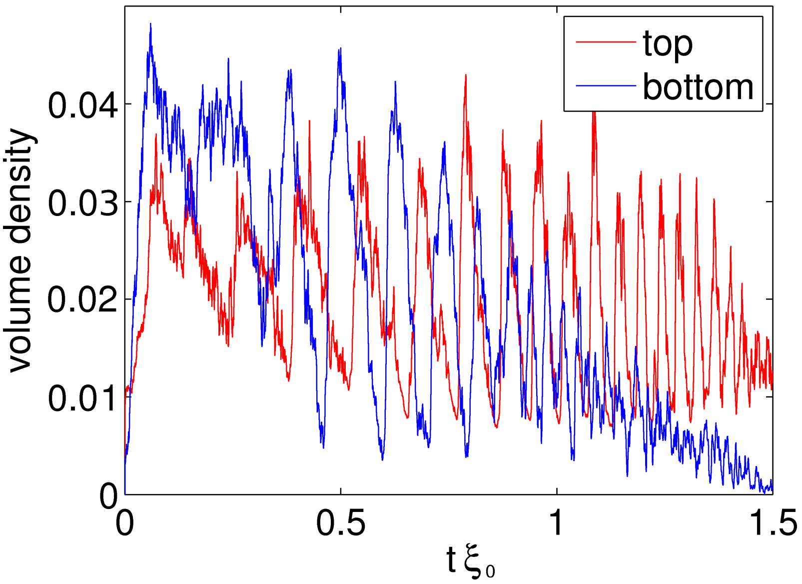

Figure 3.17: A sample of water/isobutoxyethanol is heated with a constant driving rate $\xi_0 = 0.1\mathrm{h}^{-1}$. The volume fraction of droplets oscillates in both phases as a function of time with different oscillation periods. We observe an increase of the oscillation frequency and a decrease of the amplitude.

oscillation for three very pronounced oscillations. A number of processes are involved in the evolution of the droplet size distribution (confer section 3.1.1). We drive the system in a way that supersaturation is created at a constant rate ξ. First droplets are nucleated on impurities in the system acting as condensation nuclei. Typical droplet distances measured in the experiment are $\lambda \approx 50 - 150\mu$m. On the length scale of droplet distances diffusion is quite fast (typical time scale 10 s). The created supersaturation diffuses to the droplets. At the beginning of the oscillation, we observe the abrupt appearance of a relatively narrow distribution of droplets with a typical radius of 9μm, which is well above the detection threshold (3μm). Droplets smaller than this typical radius can be detected, however they seem to grow very fast to this size. Once the droplets reach a critical radius, sedimentation becomes significant. Bigger droplets sediment faster than small ones and grow by collisions with small droplets present in their path. This leads to a broadening of the size distribution. The peak of the volume distribution gradually shifts to about 27μm radius. Droplets with radii bigger than 40μm can be detected but are rarely found in the experiment. The droplets sediment to the interface and the system is clearing up until a critical droplet density is reached and new droplets are nucleated.

Nice prototypes of the described precipitation cycle are usually observed for the first few oscillations of a measurement. At later times (i.e. higher reduced temperatures (3.1)) the number density of nucleated droplets is smaller and the droplets grow very fast to a radius of about 20μm. Also the sedimentation velocities are significantly higher because the density difference is larger. Therefore the range of observed droplet sizes is much smaller. Also the first oscillation cycle is usually different to the following ones. As the first cycle starts with almost no droplets, probably more droplets are nucleated than for

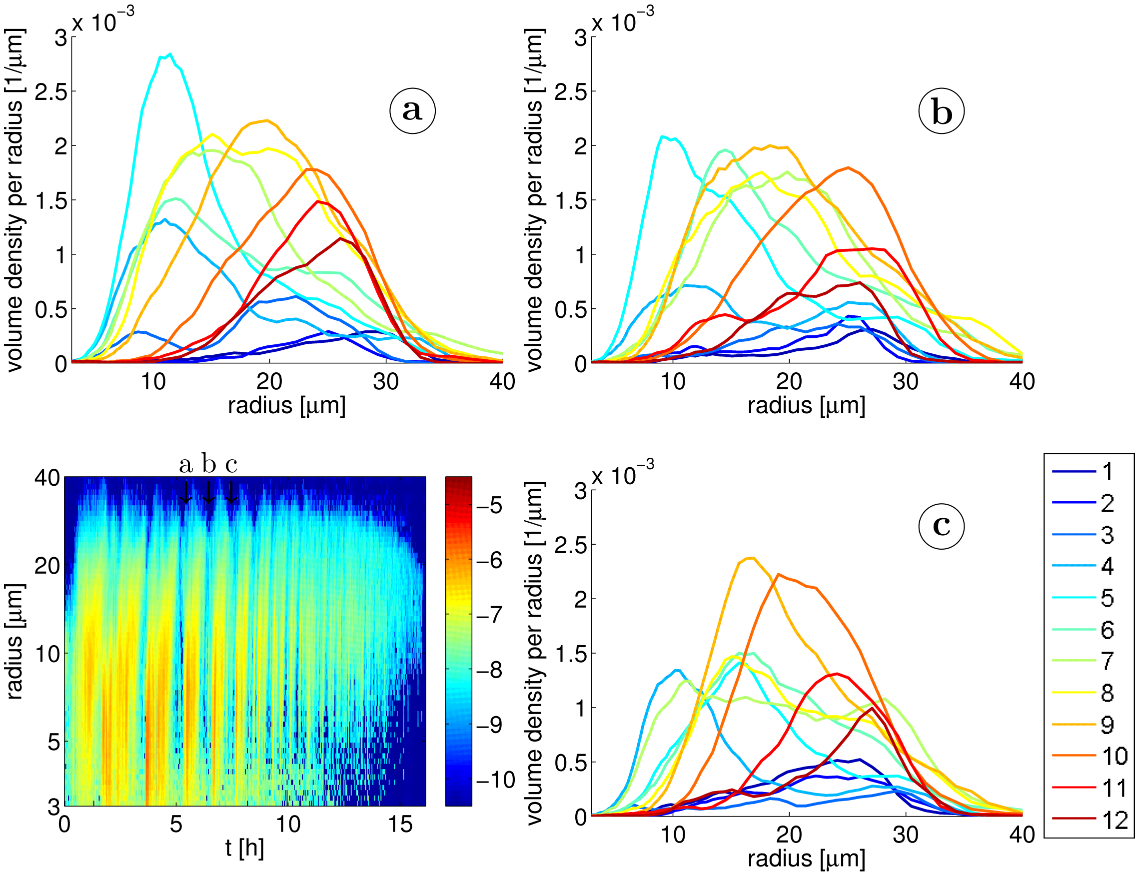

Figure 3.18: Evolution of the size distribution: number density of the whole measurement of the bottom phase with $\xi_l = 1.05 \cdot 10^{-5}\mathrm{s}^{-1}$ (lower left) for a water/isobutoxyethanol mixture on a decadic logarithmic color scale with unit $\mu\mathrm{m}^{-4}$. In the other three figures the droplet volume density is shown for the 12 parts of each oscillation, where a,b, and c correspond to the fourth, fifth and sixth oscillation in the size distribution.

Repeated precipitation cycles can be observed in the evolution of the size distribution: A rather narrow peak at $9\mu\mathrm{m}$ appears at the beginning of the oscillation. The peak gets broader and shifts towards $27\mu\mathrm{m}$. When it has almost disappeared a new peak arises at $9\mu\mathrm{m}$ and the next cycle starts.

This figure is reproduced from the Diploma thesis of Rohloff [96].

the following oscillations. Therefore the number density that is observed is larger than for the following oscillations. The distribution is broader and the peak of the droplet volume fraction evolution is flatter.

3.6.1.3 Oscillation Period Dependence on Driving Rate

For each measurement, the driving rate is kept constant. We find, that the oscillation period not only changes within each experimental run, but it also depends on the driving rate. To study the driving dependence, we conduct a series of runs with driving rates varying over almost 3 decades. For the fastest runs with measurement durations of down to 10 min, only one oscillation period can be observed. In the slowest runs, only small droplet number densities are observed. They have to be stopped after 30 to 60h because the dye in the sample is bleached. Figure 3.19 shows that the oscillation period decreases with increasing driving rate in both layers. The driving dependence is nontrivial, the time scale for the oscillation is not simply given by ξ^{-1}.

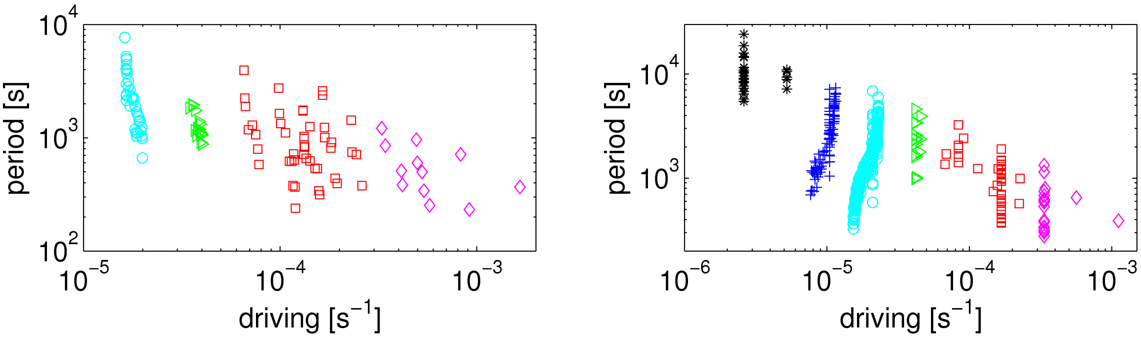

(a) (b)

Figure 3.19: The oscillation period Δt depends on the driving rate ξ_r (3.42) for the upper (a) and on ξ_l (3.43) for the lower (b) layer of a water/isobutoxyethanol mixture. The colors and symbols encode different heating rates ξ: black stars, $\xi < 6 \times 10^{-6}\,\mathrm{s}^{-1}$; blue crosses, $\xi < 1.3 \times 10^{-5}\,\mathrm{s}^{-1}$; cobalt circles, $\xi < 3 \times 10^{-5}\,\mathrm{s}^{-1}$; green triangles, $\xi < 6 \times 10^{-5}\,\mathrm{s}^{-1}$; red squares, $\xi < 3 \times 10^{-4}\,\mathrm{s}^{-1}$; and magenta diamonds, $\xi > 3 \times 10^{-4}\,\mathrm{s}^{-1}$. In both layers, the oscillation period decreases with increasing driving rate.

3.6.2 Droplet Growth

To understand what sets the time scale for the oscillation period, we consider the growth rate of individual droplets. For small droplets, growth by diffusion of supersaturation dominates. Big droplets however mainly grow by collisions with smaller droplets. Now, we explore the different growth mechanisms and show how the bottleneck in droplet growth is reflected in the evolution of the droplet size distribution. We derive a growth equation for the typical droplet radius which is inspired by the work of Wilkinson [137].

3.6.2.1 Ostwald Ripening

Droplet growth by diffusion is traditionally investigated with quench experiments (confer section 3.2.3.2), where temperature or pressure are suddenly changed and the time evolution of the typical droplet radius is observed in scattering measurements [111]. In this case, a fixed amount of supersaturation is created by the quench and diffuses to the droplets. The inital stage of droplet growth is described by classical Lifshitz-Slyozov theory [69]. Small droplets have a higher curvature and therefore a higher Laplace pressure. They dissolve and the material diffuses to big droplets with low Laplace pressure. This process is known as Ostwald ripening. Lifshitz-Slyozov theory predicts a scale invariant size distribution with the time evolution of the droplet radius given by

$$\dot{r} \sim D\sigma \frac{1}{r}\left(\frac{1}{\bar{r}} - \frac{1}{r}\right) \tag{3.34}$$

with D denoting the mutual diffusion coefficient, $\bar{r}$ is the average radius and σ is a prefactor with the unit of a length

$$\sigma \equiv \frac{2\gamma V_\mathrm{m} \Phi_\mathrm{e}}{RT}. \tag{3.35}$$

The surface tension is denoted by γ, V_m is the molecular volume, Φ_e is the equilibrium minority component concentration, R the gas constant and T the absolute temperature. The temperature dependence of the material properties as well as σ is given in the appendix 3.A. Note that this length scale is subatomar for the water/isobutoxyethanol system due to the small interfacial tension. Therefore, σ should be regarded as a temperature dependent prefactor with the unit of a length. It should not be interpreted as an actual length scale for the droplet sizes undergoing Ostwald ripening. Equation (3.34) implies that the biggest droplets grow like [137]

$$\dot{r} \sim D\sigma \frac{1}{r^2}. \tag{3.36}$$

Equation (3.34) can be rewritten as an equation for change of the individual droplet volume V_i

$$\dot{V_i} \sim D\sigma \left(\frac{r_i}{\bar{r}} - 1\right). \tag{3.37}$$

Summing over all droplets yields

$$\begin{aligned} \dot{V_\mathrm{tot}} &= \sum_i \dot{V_i} \sim D\sigma \sum_i \left(\frac{r_i}{\bar{r}} - 1\right) && (3.38) \\ &= D\sigma \left(\frac{N\bar{r}}{\bar{r}} - N\right) = 0. && (3.39) \end{aligned}$$

Hence equation (3.34) can only be valid in situations where the total volume of droplets is constant.

3.6.2.2 Droplet Volume Production

In the present study, however, the temperature is changed and therefore the total droplet volume changes in time. We now calculate the droplet volume production rate due to the temperature ramp. We consider droplets rich in component A in the say top layer, which is rich in component B. For the moment, sedimentation is neglected. We assume that diffusion is sufficiently fast so that the droplets and the bulk have equilibrium volume compositions $\varPhi_l$ and $\varPhi_r$ (referring to component B, left and right branch of the binodal in the phase diagram), respectively. The volume of component B which is stored in the droplet volume δV_d and in the bulk volume $V - \delta V_d$ is therefore equal to the volume of B in the sample volume before

$$\delta V_d \varPhi_l + (V - \delta V_d)\varPhi_r = V(\varPhi_r - \delta\varPhi_r). \tag{3.40}$$

Therefore the change in the droplet volume fraction $\delta v \equiv \delta V_d/V$ is given by

$$\delta v = \frac{\delta\varPhi_\mathrm{r}}{2\varPhi_0}. \tag{3.41}$$

We find ξ_r to be the growth rate of the droplet volume fraction

$$\dot{v} = \frac{1}{2\varPhi_0}\frac{\partial\varPhi_r}{\partial t} \equiv \xi_r \tag{3.42}$$

in the B rich layer. Analogous we identify

$$\xi_\mathrm{l} \equiv \frac{1}{2\varPhi_0}\frac{\partial\varPhi_\mathrm{l}}{\partial t} \tag{3.43}$$

with the growth rate of droplet volume fraction in the A rich layer. It is worth to note that the thermodynamic driving rate ξ_0 (3.7) derived in section 3.2.3.3 is the sum of the droplet volume production rate in the top and in the bottom layer.

Hence we now have an estimate what volume fraction of droplets to find in the sample when sedimentation and advective transport of droplets is not dominant. Figure 3.17 shows that the volume fraction is increasing in about the first half of the oscillation period. In the second part, sedimentation is dominant and the droplets leave the layer by sedimenting towards the interface, where they coalesce with the other layer. As a rule of thumb, the droplet volume fraction generated in the first half of the period

$$\varDelta v_\mathrm{sd} \equiv v_\mathrm{max} - v_\mathrm{min} \tag{3.44}$$

should be about the droplet volume created within half the period

$$\varDelta v_\xi \equiv \xi \varDelta t/2. \tag{3.45}$$

To check test this expectation, $\varDelta v_{\mathrm{sd}}$ and $\varDelta v_\xi$ are plotted in figure 3.20. We observe, that the expected droplet volume production roughly coincides with the measured amplitude of the volume density oscillations.

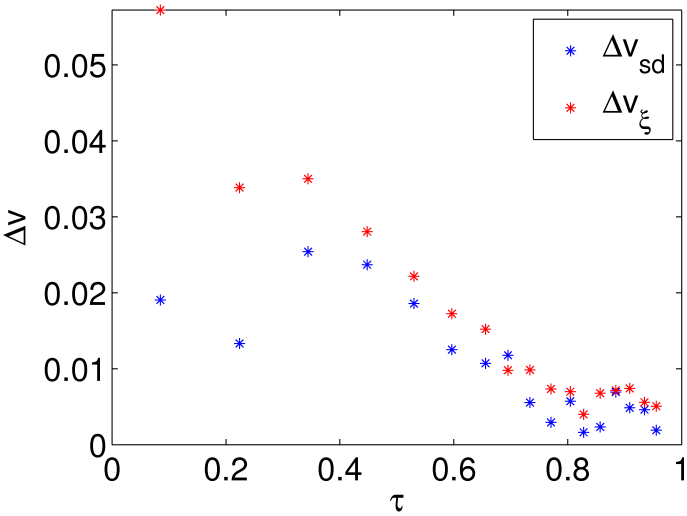

Figure 3.20: Comparison of the created (3.45) and measured (3.44) droplet volume as a function of time (3.23). The measured droplet volume fraction is similar to the predicted one.

Since typical droplet distances are bigger than typical droplet radii, it is reasonable to assume that the created droplet volume is distributed evenly on all droplets. Hence the volume growth rate of individual droplets is on average

$$\dot{V}_{\mathrm{drop}} = \frac{\xi}{n} \tag{3.46}$$

with n denoting the droplet number density. This relation can be transfered into an equation for the droplet radius growth rate

$$\dot{r} = \frac{1}{4\pi r^2} \frac{\xi}{n}. \tag{3.47}$$

Note that this growth law has the same scaling as the one predicted for Ostwald ripening (3.36) [137], but with a completely different prefactor, as we will see in section 3.6.3.1, figure 3.24.

3.6.2.3 Growth by Sweeping

For big droplets, another growth mechanism is dominant. Droplets moving relative to the fluid collide with small droplets which follow the flow. As we combined the tracking of droplets with a measurement of the droplet radius, we are able to measure how the vertical velocity of the droplets depends on the radius. For single spheres in a quiescent unbounded fluid the sedimentation velocity of a particle is given by the Stokes velocity [13, p. 234] (3.29)

$$u_{\text{Stokes}} \equiv \frac{2}{9}\frac{\Delta\rho g}{\eta} r^2 \equiv \kappa r^2 \tag{3.48}$$

with $\Delta\rho$ denoting the density difference between particle and fluid, g the gravitational acceleration and η the viscosity of the bulk fluid [67, 96]. The prefactors to the radius dependence are abbreviated by

$$\kappa \equiv \frac{2}{9}\frac{\Delta\rho g}{\eta}. \tag{3.49}$$

We are measuring close to the wall (typical distance 0.3mm) and the droplet distances are in the range of $50 - 150\mu$m. Therefore it is not obvious how well the Stokes velocity approximates the motion of droplets relative to the fluid. In figure 3.21 the vertical droplet velocities are compared to the sedimentation velocity (blue points) due to equation (3.29) modified by the mean vertical velocity of the flow, which is calculated from the flow field. The error bar of the Stokes velocity computation represents the deviation of density difference and viscosity in the considered time interval due to the temperature shift. The Stokes velocity of a sphere (3.29) appears to describe the average settling rate very well. We attribute the deviations for small droplet radii to the fact that both the droplet size distribution and the average flow velocity oscillate. Most of the small droplets can be found at the beginning of the oscillations, when the average downward flow velocity is relatively small (see below). The oscillations of the flow velocity that we were observe in the measurements of the flow field are presented in the Diploma thesis of Rohloff [96].

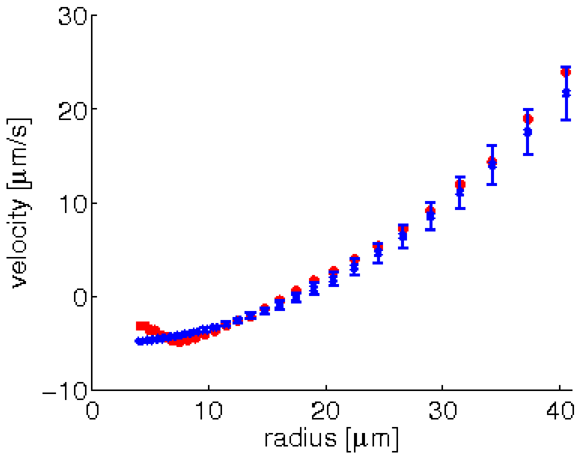

Figure 3.21: Comparison of the measured vertical velocity of the droplets (red) and the Stokes velocity modified by the mean flow (blue), in the bottom phase at 26°C. The error bar of the Stokes velocity corresponds to the deviation of density and viscosity within the investigated time interval. The statistical error of the mean vertical velocity (red) is smaller than the marker size. The systematic deviation for small droplets may be attributed to the fact that most small droplets are observed at times of small mean vertical flow velocity. The figure is reproduced from [67].

Droplets sedimenting with the Stokes velocity (3.29) sweep through a volume V_{sweep} with a rate

$$\dot{V}_{\text{sweep}} = \pi r^2 u_{sed} = \pi \kappa r^4. \tag{3.50}$$

We now want to estimate the growth rate of the biggest droplets. They sediment faster than the smaller droplets and therefore may collide and coalesce with some efficiency ϵ with the droplets in the swept volume V_{sweep}. The volume growth rate by collisions can therefore be estimated by [137]

$$\dot{V}_{drop} = \epsilon \pi \kappa r^4 v \tag{3.51}$$

with the droplet volume fraction v and the collision efficiency ϵ. Equation (3.51) can again be expressed as an equation for the radius growth

$$\dot{r} = \frac{\epsilon}{4} \kappa r^2 v. \tag{3.52}$$

The collision efficiency ϵ is not known a priory and cannot be measured directly. The efficiency has to be smaller than 1 and depends on droplet radii, density difference between droplet and fluid and the fluid viscosity. Pruppacher and Klett [90] (p. 470–471) argue that for small droplets ($\leq 10\mu$m) the collision efficiency is in the order of $1-3\%$ and does not depend very much on the droplet radii, as viscous effects are dominant over inertia. However these estimates refer to the case of water droplets in air. We expect ϵ to be in the range $0.01 < \epsilon < 1$ for our case. We therefore use it as a fit parameter to adjust our model to the experimental observations.

3.6.2.4 Bottleneck in Droplet Growth

Having derived growth equations for diffusional growth due to the temperature change (3.47) and the growth by gravitational collection (3.52), we can combine the two equations

$$\dot{r} = \frac{1}{4\pi r^2} \frac{\xi}{n} + \frac{\epsilon}{4} \kappa r^2 v. \tag{3.53}$$

In figure 3.22, the growth rate dependence on the radius is plotted in arbitrary units. The growth by driving the system is indicated by the blue dashed line, the gravitational collection is shown by the red dotted-dashed line. The sum of both, the black solid line has a global minimum at $r = r_c$. This implies a bottleneck in droplet growth resulting from the minimum in the growth speed for $r = r_c$. The droplets reach the bottleneck radius very fast by diffusion of supersaturation. It takes them a long time to grow through the bottleneck, as neither growth by diffusion is changing the radius significantly any more nor growth by sweeping is efficient yet. Once the droplets overcome the bottleneck, the growth is accelerated. The bigger the droplets are, the faster they sediment which in return increases the droplet volume gained by collisions with smaller droplets. This growth law yields a finite time runaway for the droplet radius. Hence the period is selected by the

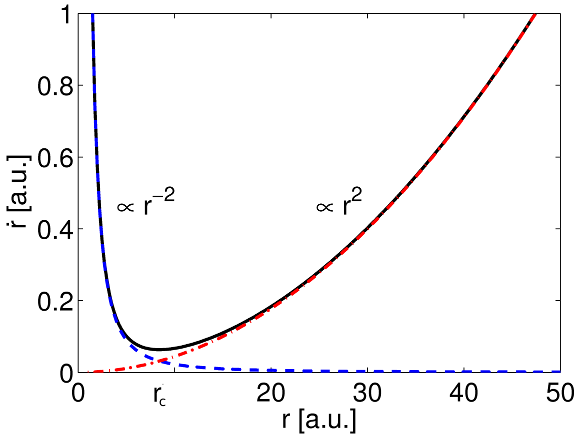

Figure 3.22: Sketch of the radius growth rate as a function of the radius (black solid line), equation (3.53). For small droplets, the diffusional growth $\dot{r} \sim r^{-2}$ (blue dashed line) is dominant, for large droplets sweeping $\dot{r} \sim r^2$ (red dotted-dashed line) is dominant. There is a bottleneck radius where the growth is slowest.

time the droplets need to cross the bottle neck. We will further explore this insight and compare it to our experimental data in section 3.6.3.

To calculate the bottleneck radius r_c, the two contributions of (3.53) are equated with each other, giving

$$r_c = \left(\frac{\xi}{\pi n \epsilon \kappa v} \right)^{1/4} \tag{3.54}$$

for the bottleneck radius.

Is the bottleneck in droplet growth observable in the droplet size distribution? In figure 3.18 we can see that at early stages of the oscillation cycle a peak develops at a mean radius of 9μm. The tail towards smaller droplets is physical, the detection threshold of our droplet detection and tracking algorithm is set to 3μm. Also by visual inspection of videos we observe that droplets appear with a typical radius of 9μm in the first few oscillations, though some smaller droplets are visible. This is consistent with the growth law described in (3.47) and a critical radius of about 9μm at the beginning of oscillations. To this end it is reasonable to conjecture that the typical droplet radius observed in the droplet size distribution is approximately the bottleneck radius r_c of droplet growth.

To test our assumption, we plot the droplet volume weighted average radius and the prediction (3.54) as a function of time in figure 3.23. We also plot the radius of the maximum in the volumedistribution shown in figure 3.18, where each oscillation is split into 12 time bins. The average radius is a rough estimate for the position of the peak in the droplet size distribution. Since the size distribution is quite broad for a considerable time of the oscillation period, the average radius varies less than the position of the peak in the distribution. Comparing the times of the peaks and the minima in the prediction for r_c and the average droplet radius we find excellent agreement. The peak position of the volume distribution r_{peak} follows our prediction for r_c quite well. Systematically, the average droplet radius increases before the prediction for the bottleneck radius increases. This observation may be attributed to the broadening of the size distributions when the

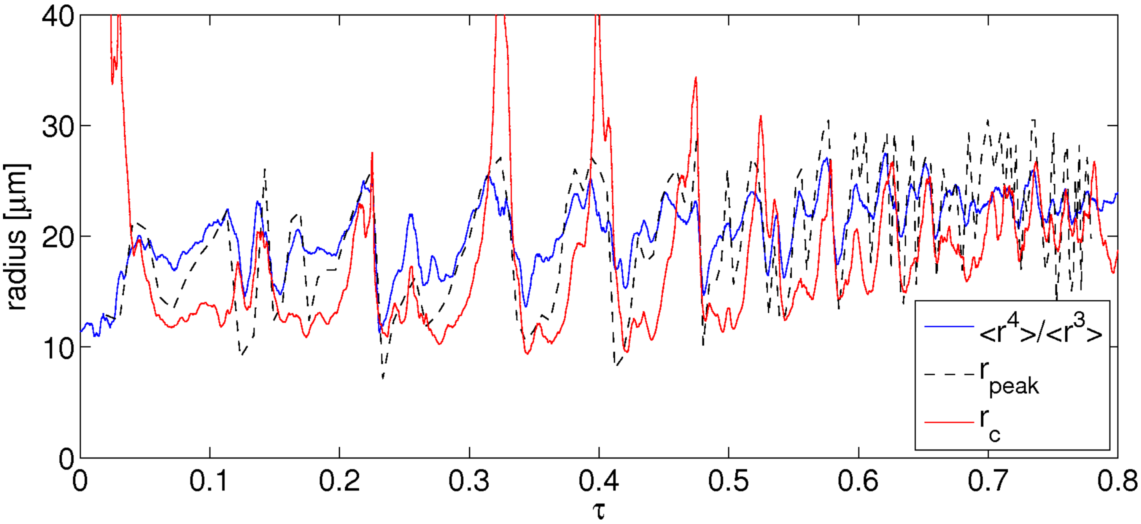

Figure 3.23: The plot shows the volume weighted average of the droplet radius (blue) as a function of time (3.23). The peak of the volume distribution (see figure 3.18) is indicated by a black dashed line. It is follows reasonably well the prediction of the bottleneck radius (3.54) (red). The times of the peaks and the minima of the curves fit very well. Since the volume distribution is at some times quite broad and even bimodal, the average radius varies rather less than the peak of the volume distribution.

collisions start to play a role. For the prediction of r_c (3.54) the collision efficiency ϵ was set to 0.1. This value is quite reasonable and within the expected interval $0.01 < \epsilon < 1$.

3.6.3 Model for Oscillation Period

Based on the growth equation for droplet radii (3.53), a prediction for the time scale of the oscillation period is worked out. In order to do this, we first have to investigate the driving dependence of the droplet number density.

3.6.3.1 Droplet Number Density: Scaling with Driving Rate

In figure 3.24(a) the droplet number density of tracked droplets is shown for four different heating rates. It is observed, that the number of droplets is higher for higher heating rates. For driving rates about 1-2 $\cdot 10^{-5}\text{s}^{-1}$ very clear oscillations in the droplet number densities are visible. The oscillations are less pronounced for higher driving rates. For lower driving rates tracking becomes difficult because the duration of the measurement increases. Also the tracking algorithm is optimized for droplet number densities typical for measurements with $\xi = \mathcal{O}(10^{-5}\text{s}^{-1})$. For significantly lower droplet number densities the calculation of the flow field becomes difficult, which is necessary for the prediction of the droplet position in the subsequent image.

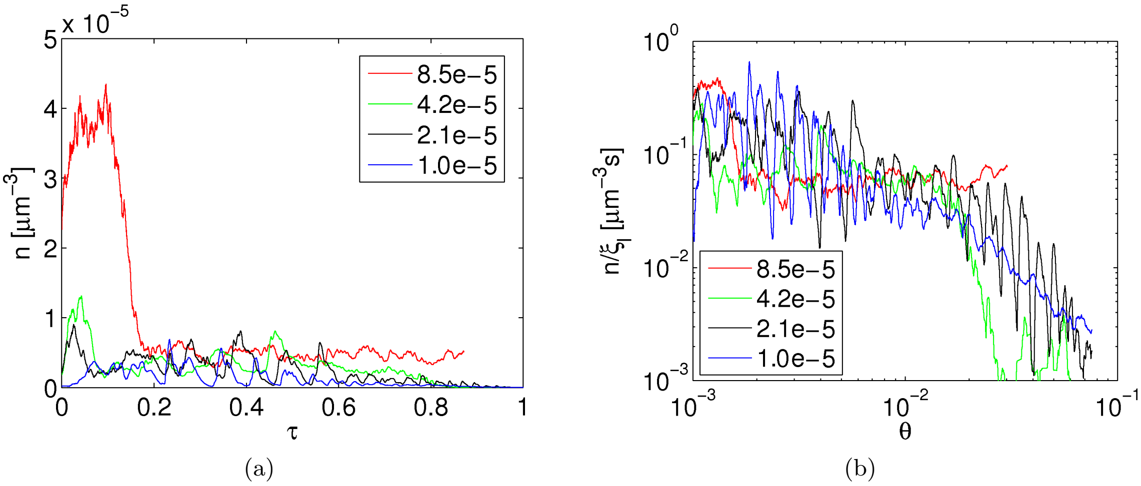

Figure 3.24: (a) The droplet number density in the bottom phases of a water/isobutoxyethanol sample is plotted for different heating rates as a function of time (3.23). The legend gives the average values for the driving rate ξ_l for the different curves. The droplet number density increases with increasing driving rate and decreases in time, because temperature is increasing.
(b) The droplet number density is rescaled by the driving rate ξ. It is plotted as a function of the reduced temperature θ.

We conjecture that the droplet number density may be proportional to the driving rate ξ. In figure 3.24(b) the droplet number density is divided by the droplet volume production rate (ξ_l in this case) and plotted as a function of the reduced temperature. The peaks of the rescaled droplet number density compare fairly well for the different driving rates and show a significant temperature dependence. The number of droplets nucleated at the beginning of the oscillations may depend on material parameters like the interfacial tension or the diffusion coefficient, which all depend strongly on the reduced temperature. In the appendix 3.A the most important material properties of our model systems are summarized. Up to now we are not aware of any satisfactory prediction for the droplet number density in slowly driven phase separation of binary mixtures. Assuming that the droplet number density is proportional to the driving rate, reduces the growth rate of small droplets to

$$\dot{r} = \frac{K(\theta)}{r^2} \tag{3.55}$$

where $K(\theta) \equiv \frac{\xi}{4\pi n}$ is a temperature dependent prefactor. Note that this growth law is similar to the one expected for the largest droplets in a mixture undergoing Ostwald ripening (confer section 3.6.2.1). The following line of argument was inspired by ideas of Wilkinson about the interplay of Ostwald ripening and growth by sweeping [137]. With

(3.55) the equation for the bottleneck radius (3.54) reads

$$r_c = \left(\frac{4K}{\epsilon\kappa v}\right)^{1/4}. \tag{3.56}$$

3.6.3.2 Theoretical Prediction

We aim to get an expression for the oscillation period of the precipitation cycle $\varDelta t$. In the lowest order approximation, it is the sum

$$\varDelta t = t_1 + t_2 \tag{3.57}$$

of the time t_1 it takes to grow by diffusion to the bottleneck radius r_c and the time t_2 it takes to reach by collisions the runaway for the droplet radius. Integrating equation (3.55) with the boundary conditions $r(t=0)=0$ and $r(t=t_1)=r_c$ yields

$$t_1 = \frac{r_c^3}{3K} \tag{3.58}$$

for the time it takes to grow to the bottleneck radius.
In section 3.6.2.2 it was shown that the droplet volume fraction can be well approximated (at least for the first half of the oscillation period) by

$$v(t) = \xi \cdot t. \tag{3.59}$$

Thus when the droplet radius has grown to r_c, the volume fraction is

$$v(t_1) = \xi t_1. \tag{3.60}$$

Inserting equations (3.56) and (3.60) into (3.58), we derive the scaling of the time t_1

$$t_1 \sim K^{-1/7}(\epsilon\kappa\xi)^{-3/7}. \tag{3.61}$$

We rewrite the growth equation for sweeping (3.52) by inserting (3.59)

$$\dot{r} = \frac{\epsilon}{4}\kappa r^2 \xi t. \tag{3.62}$$

We integrate (3.62)

$$\int_{r_c}^{r} \frac{1}{r'^2} dr' = \frac{\epsilon\kappa\xi}{4} \int_{t_1}^{t} t' dt' \tag{3.63}$$

yielding

$$\frac{1}{r_c} - \frac{1}{r} = \frac{\epsilon\kappa\xi}{8}\left(t^2 - t_1^2\right). \tag{3.64}$$

This means that the droplet radius diverges, $r \to \infty$, at a finite time $t \to \mathit{\Delta} t$

$$\frac{1}{r_c} = \frac{\epsilon\kappa\xi}{8}\left(\mathit{\Delta} t^2 - t_1^2\right). \tag{3.65}$$

This gives

$$\mathit{\Delta} t = \left(\frac{8}{\epsilon\kappa\xi}\frac{1}{r_c} + t_1^2\right)^{1/2}. \tag{3.66}$$

for the oscillation period. We insert equations (3.56), (3.58), and (3.59) into $\frac{8}{\epsilon\kappa\xi}\frac{1}{r_c}$ in (3.66) finding that t_1 and $\mathit{\Delta} t$ have the same scaling. For the oscillation period $\mathit{\Delta} t$ we get

$$\mathit{\Delta} t = \alpha\left(K\epsilon^3\kappa^3\right)^{-1/7}\xi^{-3/7} \tag{3.67}$$

with α being a numerical prefactor. As the droplet radius would grow to infinity at a finite time, the height of the sample is predicted to have no significant influence on the oscillation period.

3.6.3.3 Droplet Volume Density: Scaling with Driving Rate

The prediction for the oscillation time scale dependence on the driving rate implies together with (3.59) that the droplet volume fraction created in each oscillation scales with $v \sim \xi^{4/7}$. In figure 3.25(a) we show the measured droplet volume fraction for different driving rates. The data for the driving rates $\geq 10^{-5}\mathrm{s}^{-1}$ are from tracked droplet data, the slowest run is for droplet data coming from the analysis of individual images. In figure 3.25(b) we show that the rescaling the droplet volume density with $\xi^{4/7}$ gives a good agreement between the measurements.

Hence we have now found the explanation for the decrease of the amplitude in the signal for the heat capacity and turbidity and the increase of the oscillation frequency observed in many different experimental studies [8, 33, 60, 125–128]. On the one hand, for higher reduced temperatures, i.e. if the system is further away from the critical point (irrespecitve of the fact whether the system has an upper or a lower miscibility gap), the density difference is higher. Therefore the sedimentation velocities are increased, which increases the growth rate due to collisions. On the other hand, the number density of nucleated droplets is smaller, which may be associated with the increase of the diffusion coefficient and the interfacial tension. Since the droplet number density is smaller, the generated droplet volume is shared by less droplets and the individual droplets grow faster also in the diffusional growth regime. Both effects decrease the time that the droplets need to pass the bottleneck. So the observed oscillation periods decrease further away from the critical temperature. The decrease of the amplitude is a direct consequence of the decrease in the oscillation period: When the oscillation period is shorter, less droplet volume can be created during that time.

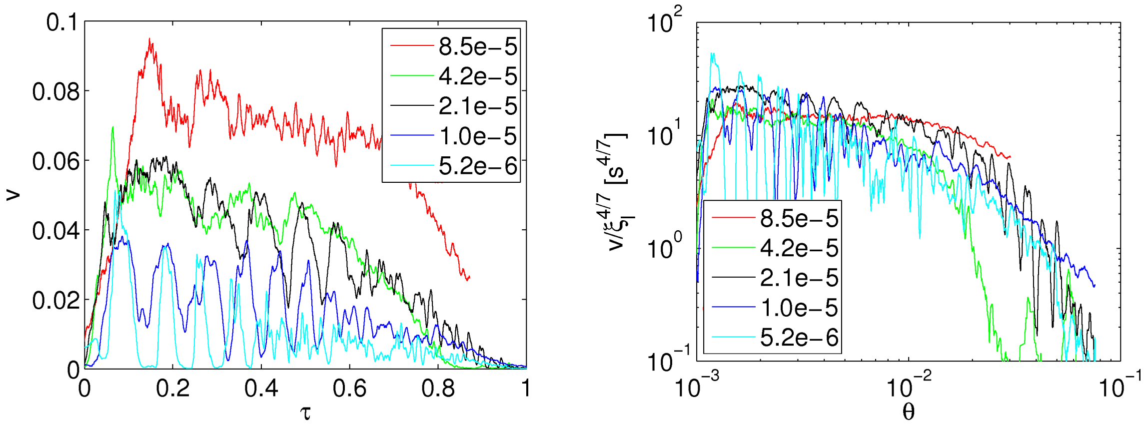

(a)

(b)

Figure 3.25: (a) The droplet volume fraction in the bottom phases of a water/isobutoxyethanol sample is plotted for different heating rates as a function of time (3.23). The legend gives the average values for the driving rate ξ_l for the different curves in units of s^{-1}. The droplet volume fraction increases with increasing driving rate and decreases in time, because temperature is increasing. The data in the range $1.010^{-5}\mathrm{s}^{-1} < \xi < 8.510^{-5}\mathrm{s}^{-1}$ is calculated from tracked droplets, the data for $\xi = 5.210^{-6}\mathrm{s}^{-1}$ comes from the analysis of single images without tracking (note that this measurement took 32h).
(b) The droplet volume fraction is rescaled by the expected driving dependence $\xi^{4/7}$. It is plotted as a function of the reduced temperature θ. The peaks of the rescaled droplet volume fraction fall roughly on top of each other. For fast heating rates the oscillations are not very pronounced and the agreement is not very good though.

3.6.3.4 Oscillation Period: Scaling with Driving Rate and Reduced Temperature

A more elaborate check of the prediction (3.67) is possible by rescaling the oscillation periods shown in figure 3.19 with $\xi^{3/7}$ and plotting them as a function of the reduced temperature θ. Indeed the oscillation periods fall on one master curve, presented in figure 3.19. This graph is the main result of the presented work on phase separation. Developing a theoretical prediction for the driving dependence of the oscillation period was the essential step to be able to create a master plot for the oscillation period. It is difficult to get the driving dependence from figure 3.19 directly since the dependence on the temperature is very pronounced.

Comparison of the droplet growth due to the equal partition of the created droplet volume (3.55) with the growth expected for Ostwald ripening (3.36) suggests that the prefactor $K = \xi/n$ may be proportional to $D\sigma$. We try this and find for the scaling of the oscillation period

$$\Delta t = \alpha' \left(D\sigma\epsilon^3\kappa^3\right)^{-1/7} \xi^{-3/7} \tag{3.68}$$

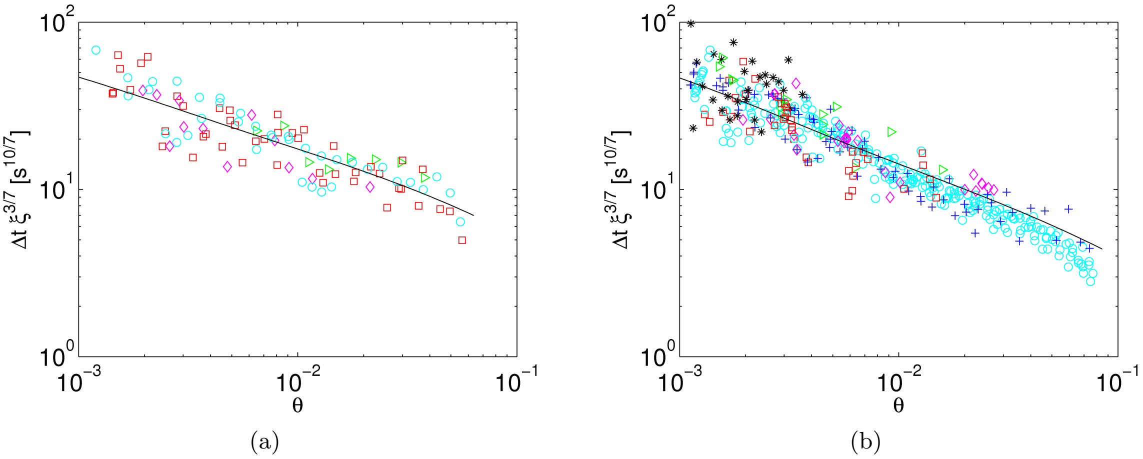

(a)

(b)

Figure 3.26: Plot of temperature dependence of $\Delta t\,\xi^{3/7}$, for the upper (a) and the lower (b) layer of water/isobutoxyethanol mixtures. The colors and symbols encode different heating rates ξ: black stars, $\xi < 6 \times 10^{-6}\,\mathrm{s}^{-1}$; blue crosses, $\xi < 1.3 \times 10^{-5}\,\mathrm{s}^{-1}$; cobalt circles, $\xi < 3 \times 10^{-5}\,\mathrm{s}^{-1}$; green triangles, $\xi < 6 \times 10^{-5}\,\mathrm{s}^{-1}$; red squares, $\xi < 3 \times 10^{-4}\,\mathrm{s}^{-1}$; and magenta diamonds, $\xi > 3 \times 10^{-4}\,\mathrm{s}^{-1}$. The solid line is a fit for a prediction using (3.67) together with the assumption that $K \sim D\sigma$.

with one single dimensionless fit parameter α'. We fit equation (3.68) to our data for the oscillation periods in one of the two layers and get the best fit for $\alpha' = 0.26$ assuming $\epsilon = 0.1$ as suggested by our fit of the bottleneck radius (confer section 3.6.2.4), presented in figure 3.26. The same value for the fit parameter α' gives also a good fit of the data in the other layer. Eventually, the oscillation period is predicted without any free fit parameter.

3.6.4 Dependence on any other Parameter?

The presented model predicts that the oscillation period does not depend on the height of the sample. To check this prediction, the oscillations of water/isobutoxyethanol samples with heights Λ of the bottom phase in the range of 2mm to 50mm were analyzed. For better comparison of the measurements, the periods are rescaled by the driving dependence $\xi^{3/7}$ and by the effective temperature scaling $\theta^{2/3}$. Figure 3.27 shows that the rescaled oscillation period indeed does not depend significantly on the height of the sample.

Furthermore, we took measurements with cells of width 4mm and 1mm. In both cases, oscillations with similar periods are observed. However, in the very thin cells (1×10mm), the measured oscillations of the droplet size distribution are not very pronounced. This may be due to the fact that in the very thin cell the convection is supressed. It synchronizes the nucleation wave by mixing the supersaturation in the sample. We also checked whether the height of the top layer has an influence on the oscillation period of the bottom layer, again finding no significant effect. This is in line with the numerical studies of Benczik

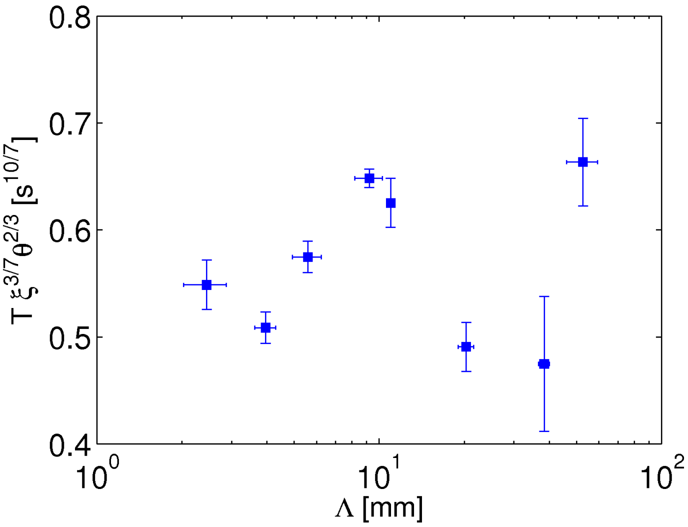

Figure 3.27: The oscillation period is measured for several heights of the oscillating layer. The periods are rescaled by the influence of the driving strength ξ and the effective temperature scaling. Within the measurement error no influence of the sample height on the oscillation period is observed. The measurements were taken in the bottom phase of water/isobutoxyethanol samples.

[15] and the measurements in two different geometries by [130].

Furthermore, we took measurements with different temperature ramps, not keeping ξ but a combination of ξ and a temperature dependent quantity constant. This way, almost constant oscillation periods or almost constant amplitudes can be observed. Also in these cases, our prediction for the oscillation period fits quite well to the data. Still we find that the most pronounced oscillations for a long fraction of the temperature ramp can be observed by keeping the driving constant, as suggested in [8].

Finally, we can conclude that the driving rate and the reduced temperature determine the oscillation period and the geometry and the form of the temperature ramp does not alter the period significantly in a wide range of parameters.

The amplitude of the droplet volume fraction oscillation, however, depends on the position of the measurement volume. Close to the meniscus, the droplet volume fraction is higher, because the droplet volume generated far away from the meniscus sediments through the fluid towards the meniscus. This implies that the scaling of the volume fraction with the driving rate and the temperature are conserved, however the prefactor varies with height. Hence the agreement of expected droplet volumes and measured amplitudes shown in figure 3.25 is only rough and not perfect.

3.7 Discussion

In this section we summarize and discuss our results for the phase separation of binary fluids.

- **Droplet Size Distribution:** Using a droplet detection and tracking algorithm developed from scratch for the phase separation of binary fluids (confer section 3.5), we measure the evolution of the droplet size distribution in time, shown in figure 3.18. The size distribution exhibits pronounced oscillations in time. We observe a precipitation cycle (section 3.6.1.2), that can be considered as an experimental analogy to the precipitation cycle in rain formation (confer section 3.1.2). Droplets are nucleated on impurities present in the system and grow rapidly to a radius of about 9μm. We show in figure 3.18 that the volume distribution of droplets has a pronounced peak at this radius. Slowly the droplets start to sediment and coalesce with smaller droplets. This leads to a broadening of the measured droplet size distribution. The peak of the volume distribution slowly shifts towards a radius of about 27μm. Once the droplet radius exceeds 30μm, the sedimentation velocity is sufficiently fast that to reach the interface within less than a minute. More and more droplets sediment and leave the system decreasing the droplet number density. This way the droplet distance increases and the constantly increased supersaturation takes more time to diffuse to the droplets. When the supersaturation reaches a critical value, droplets are nucleated and a new precipitation cycle begins.

- **Droplet Volume Fraction:** Typical droplet volume fractions during the phase separation process are between 1 and 5% (confer figure 3.17). The volume fraction shows pronounced oscillations, which are used to measure the oscillation period. As the droplet volume density is not very sensitive on the number of detected small droplets, we get also reasonable results for the calculation of the volume fraction from the analysis of individual images without running the droplet tracking algorithm. The droplet volume growth rate (3.42), (3.43) we derive in section 3.6.2.2 roughly fits to the volume production rate observed in the experiment (see figure 3.20). The mass transport in the system is dominated by the sedimentation of droplets. In section 3.6.2.3 we show that the sedimentation velocity of droplets fits very well to the Stokes law (figure 3.21).

- **Droplet Number Density:** We find in section 3.6.3.1 that the number density of droplets is proportional to the driving rate and decreases with incresing temperature, shown in figure 3.24. A satisfactory prediction how the number density is related to the material parameters is missing up to know. To enable upcoming suggestions for these relations, the temperature dependence of the relevant material properties of the studied model system is given in appendix 3.A.

- **Droplet Growth Rate:** Two growth mechanisms are explored in section 3.6.2: Small droplets grow by diffusion of the supersaturation created by the temperature ramp towards the droplets (3.47). Big droplets sediment with the Stokes velocity and collide with some efficiency of the order of 0.1 with the smaller droplets contained in the volume they sweep through (3.52). In section 3.6.2.4 we show that inserting the droplet number densities and droplet volume fractions measured in the experiment suggests a bottleneck in droplet growth (3.54) in the range between 9 and 27μm, as can be seen in figure 3.23. This is almost exactly the radius range where a bottleneck in the growth of cloud droplets is expected (compare section 3.1.2). The predicted evolution for the bottleneck radius coincides very well with the peak in the volume distribution measured in the experiment, as we show in figure 3.23. This is very strong evidence that we have modeled the droplet growth dynamics in an appropriate manner (3.53), using only a single fit parameter - the collision efficiency.

- **Oscillation Period:** The equation for the droplet growth rate (3.53) can be used to estimate the time scale for the oscillation period. We derive in section 3.6.3.2 that the period scales with the driving rate $\Delta t \sim \xi^{-3/7}$ (3.67), which is a nontrivial result. In figure 3.26 we show that the oscillations measured for two decades in driving rate in the top layer and almost three decades in driving rate for the bottom phase of water/isobutoxyethanol mixtures fall on a master plot for each layer by rescaling the period with $\xi^{3/7}$. The reduced temperature was varied within two decades. In section 3.6.3.4 we derive a prediction for the oscillation period (3.68) based on the assumption that the droplet number density scales with $n \sim \xi/D\sigma$ (confer appendix 3.A for the values of D and σ). Fitting only a single numerical prefactor for the data of one of the two layers, we also get an acceptable prediction (without fit parameter) for the data of the other layer (compare figure 3.6.3.4). Varying many parameters one at a time, we find no significant dependence of the oscillation period (section 3.6.4) on the height of the sample, as shown in figure 3.27, the width, the global composition or the type of the temperature ramp. This is in perfect agreement with our prediction for the oscillation period (eqn:deltat). Further more, we show in figure 3.25, that the droplet volume density scales with $v \sim \xi^{4/7}$, which is a direct consequence of our model for the oscillation period, as outlined in section 3.6.3.3. Finally, we have resolved the riddle of the drift in the oscillation period and the decrease in the amplitude, that was observed in the literature, as discussed in section 3.1.1.

3.A Material Properties of Water/Isobutoxyethanol

For comparison of the measured droplet velocities and oscillation periods with theoretical predictions, besides the phase diagram, also the density, viscosity, diffusion coefficient and interfacial tension of the two phases have to be known. The phase diagram of the systems water/isobutoxyethanol and the technique applied to measure it is presented in section 3.3. The material parameters are taken from literature and interpolated. We plot the material parameters as a function of the reduced temperature θ (3.1). We compare them to a scaling ansatz $m \propto \theta^{\alpha}$ with m denoting the material property of interest and α its scaling exponent. In this section, we denote the two liquids in a binary mixture by the subscripts a and b. The mass, volume and molar fractions $\varPhi^m$, $\varPhi^V$ and $\varPhi^n$ refer to the component a, namely isobutoxyethanol in our case.

3.A.1 Effective Scaling Exponents

For an easy check of theoretical predictions for the temperature dependence of various measured quantities, the effective scaling exponents to the temperature dependence of the density difference, viscosity, diffusion coefficient, interfacial tension, molar volume and the prefactor σ are fitted. The fitted scaling relations are indicated by dahed lines in the figures of this section. Prefactors and scaling exponents of the form

$$A = A_0 \cdot \theta^{\alpha} \tag{3.69}$$

for the θ-dependence are listed in table 3.1.

	A_0	α
$\varDelta\rho$	174kg/m^3	0.36
η_{top}	$2.3{\cdot}10^{-3}\text{Pas}$	-0.05
η_{bot}	$4.8{\cdot}10^{-4}\text{Pas}$	-0.23
D_{top}	$1.6{\cdot}10^{-9}\text{mm}^2/\text{s}$	0.89
D_{bot}	$3.6{\cdot}10^{-9}\text{mm}^2/\text{s}$	0.94
γ	$1.0{\cdot}10^{-2}\text{N/m}$	1.20
$V_{\text{m,top}}$	$5.6{\cdot}10^{-5}\text{m}^3/\text{mol}$	0.13
$V_{\text{m,bot}}$	$1.6{\cdot}10^{-5}\text{m}^3/\text{mol}$	-0.04
σ_{top}	$7.1{\cdot}10^{-11}\text{m}$	1.09
σ_{bot}	$5.7{\cdot}10^{-12}\text{m}$	0.85

Table 3.1: Prefactors and exponents for effective scaling of density difference, viscosity, diffusion coefficient, interfacial tension, molar volume and LS-prefactor with reduced temperature for water/isobutoxyethanol.

3.A.2 Density

The densities of the phases are determined by the composition, thermal expansion and molar excess volume. The density of a mixed phase mainly depends on the volume composition

$$\rho = \frac{m_a + m_b}{V} = \rho_a \varPhi^{\mathrm{V}} + \rho_b \left(1 - \varPhi^{\mathrm{V}}\right). \tag{3.70}$$

Both liquids expand slightly with increasing temperature. For water and isobutoxyethanol, Doi et al [39] propose a linearly approximation around room temperature $T_0 = 25$°C

$$\rho_{a,b}(T) = \rho_{a,b}(T_0)) - \alpha_{a,b}(T - T_0) \tag{3.71}$$

with the linear expansion coefficient α. The values for $\rho_{a,b}$ and $\alpha_{a,b}$ are given in table 3.2.

	isobutoxyethanol	water
ρ(25°C) [gcm^{-3}]	0.886255	0.997043
α [gcm^{-3}K^{-1}]	$0.968 \cdot 10^{-3}$	$0.2571 \cdot 10^{-3}$

Table 3.2: Densities and thermal expansion coefficients for water and isobutoxyethanol, taken from [39, 96]

When two liquids are mixed, gernerally the mixture has a volume deviating from the sum of the individual component volumes. This volume difference per mol is called molar excess volume. Thus the volume V in equation (3.70) has to be replaced by $V_{\mathrm{ideal}} + nV_{\mathrm{E}}^{n}$, where V_{ideal} is the sum of the volumes of the two components, n is the sum of the number of molecules in mol and V_{E}^{n} is the molar excess volume, which is typically negative. Taking this into account, the density can be formulated in terms of the mass fraction $\varPhi^m$

$$\rho = \left[\frac{\varPhi^m}{\rho_a} + \frac{(1-\varPhi^m)}{\rho_b} + \left(\frac{\varPhi^m}{M_a} + \frac{(1-\varPhi^m)}{M_b}\right) V_{\mathrm{E}}^{n}\right]^{-1}. \tag{3.72}$$

A derivation of (3.72) can be found in [96, pp. 61], as well as conversion formulars between volume, mass and molar fractions. Doi et al [39] give data for the molar excess volume of the water/isobutoxyethanol system and provide a fit to their data

$$V_{\mathrm{E}}^{n}(\varPhi^n) = \frac{\varPhi^n(1-\varPhi^n)}{1 - G(1-2\varPhi^n)} \cdot \left(A_1 + A_2(1-2\varPhi^n) + A_3(1-2\varPhi^n)^2\right) \tag{3.73}$$

with the parameters G=0.975, A_1=-3.079cm^3/mol, A_2=1.801cm^3/mol and A_3=0.839cm^3/mol. They report a slight temperature dependence of the fit parameters, which we do not take into account.

The density of the bottom, the top phase and the density difference as a function of the reduced temperature θ is shown in figure 3.28.

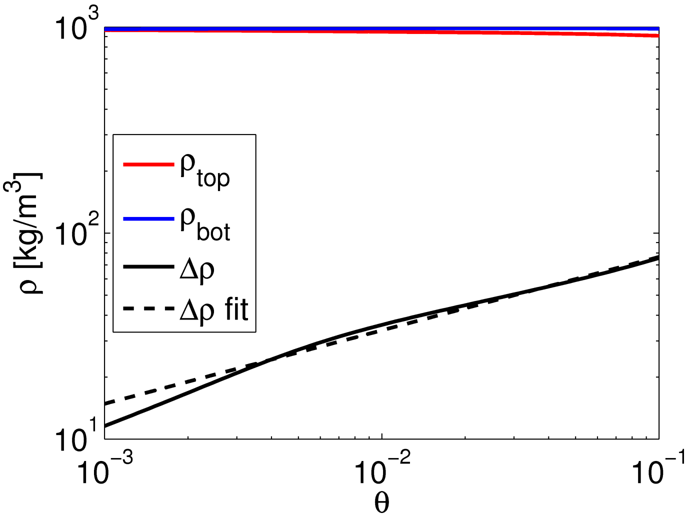

Figure 3.28: The density of the two phases and the density difference depend on temperature. Using equations (3.71), (3.72) and (3.73) with the coefficients given by [39], the densities for the water/isobutoxyethanol system are calculated for a range of reduced temperatures. The density difference is fitted by a scaling $\Delta\rho \sim \theta^{0.36}$.

3.A.3 Viscosity

We measured the viscosity of isobutoxyethanol with an Ubbelohde viscosimeter type 537 10/I made by Schott. The temperature dependence of the viscosity η [kg/ms] is fitted by

$$\eta(T) = A \cdot 10^{\frac{B\cdot(20-T)-C\cdot(T-20)^2}{T+D}} \tag{3.74}$$

with temperatures expressed in °C. The coefficients are given in table 3.3, where the values for water are taken from [134].

	$A[kg/ms]$	B	C	D
water	$1.002 \cdot 10^{-3}$	1.3272	0.001053	105
i-BE	$3.36 \cdot 10^{-3}$	1.730	0.001	108

Table 3.3: Fit coefficients for the viscosity of water and i-BE, defined by equation (3.74), the data for water is taken from [134].

To interpolate the viscosities for a mixed phase of given mass fraction Φ we use the composition-dependent viscosities at 25°Cfor a homogeneous mixture in the single phase regime given in [81]. The data is fitted with a fifth order polynomial

$$\begin{aligned}\eta(\Phi,\mathrm{T} = 25°\mathrm{C}) = -40.66\Phi^5 + 103.44\Phi^4 - 100.32\Phi^3 \\ +39.35\Phi^2 + 0.17\Phi + 0.91.\end{aligned} \tag{3.75}$$

Assuming that the coefficients of interpolation are not changing substantially in the temperature range of our measurements, a rescaled viscosity $\tilde{\eta}(\Phi)$ is defined. It only depends on the composition Φ

$$\eta(\Phi,T) = \tilde{\eta}(\Phi) \cdot \eta_{iBE}(T) + (1 - \tilde{\eta}(\Phi)) \cdot \eta_{H_2O}(T). \tag{3.76}$$

The viscosities of the two phases are shown in figure 3.29 as a function of temperature. To check the strong assumption entering this interpolation, we have measured the viscosity of the two phases at $T = 40$°C. For both phases it followes the prediction of equation (3.76) to within 2%. This is sufficiently accurate for our means.

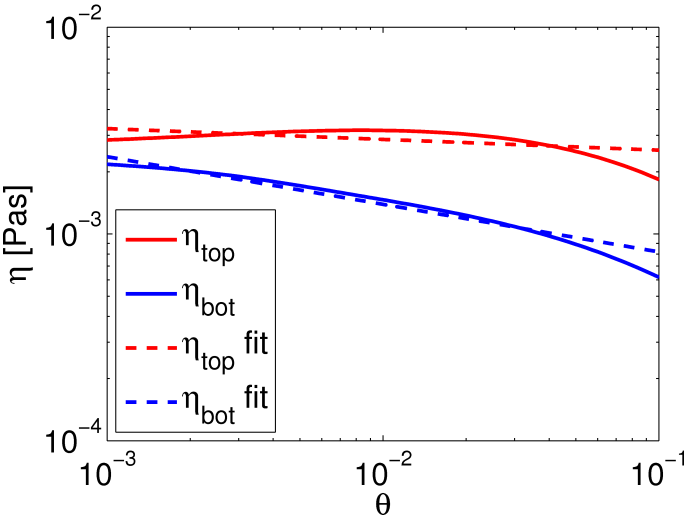

Figure 3.29: The viscosity of the two phases depends on temperature. Using equations (3.74), (3.75) and (3.76) with the coefficients given by [81, 134], the viscosities for the water/isobutoxyethanol system are calculated for a range of reduced temperatures. The viscosities of the two phases are fitted by scaling laws $\eta_{\text{top}} \sim \theta^{-0.05}$ and $\eta_{\text{bot}} \sim \theta^{-0.23}$.

3.A.4 Diffusion Coefficient

The diffusion coefficient for the two phases shows a linear dependence on temperature. At the critical point, the diffusion coefficient D approcheas the same, not vanishing value D_{c}

$$D(\theta) = D_{\text{c}} + \delta_{\text{top,bot}}\theta \tag{3.77}$$

A fit of the data for the isobutoxyethanol/water system presented by [111] gives $D_{\text{c}} = 6.4 \cdot 10^{-12}\text{m}^2/\text{s}$, $\delta_{\text{top}} = 2.1 \cdot 10^{-9}\text{m}^2/\text{s}$ and $\delta_{\text{bot}} = 4.1 \cdot 10^{-9}\text{m}^2/\text{s}$.
The temperature dependence of the diffusion coefficient is shown in figure 3.30. Be aware of the limited range of data in [111], which we extrapolate to reduced temperatures $\theta \leq 0.1$.

3.A.5 Interfacial Tension

The interfacial tension vanishes at the critical temperature. Its dependence can roughly be represented by a powerlaw

$$\gamma(\theta) = \gamma_0 \cdot \theta^{\alpha_\gamma}. \tag{3.78}$$

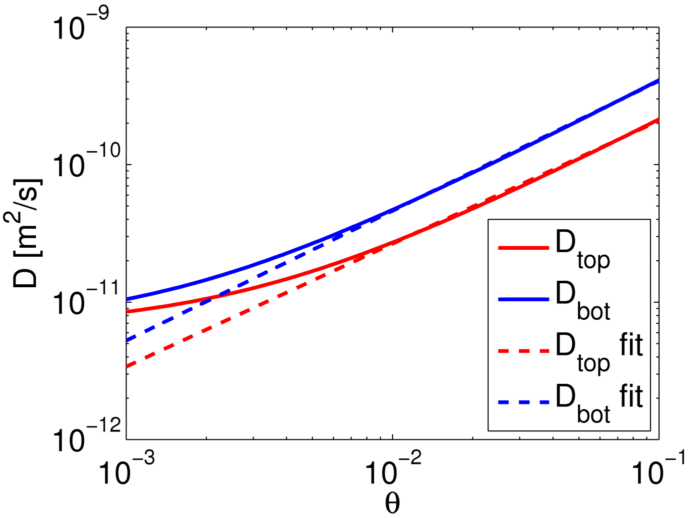

Figure 3.30: The equilibrium diffusion coefficients of the two phases depend on temperature. Using equation (3.77) with the coefficients determined from the data presented in [111], the diffusion coefficients for the water/isobutoxyethanol system are calculated for a range of reduced temperatures. The diffusion coefficients of the two phases are fitted by scaling laws $D_{\mathrm{top}} \sim \theta^{0.89}$ and $D_{\mathrm{bot}} \sim \theta^{0.94}$.

The data shown in [6] for water/isobutoxyethanol can be approximated by equation (3.78) with $\gamma_0 = 7.3 \cdot 10^{-4}$N/m and $\alpha_\gamma = 1.2$. Again be aware of the limited range of data in [6], which we extrapolate to reduced temperatures $\theta \leq 0.1$.

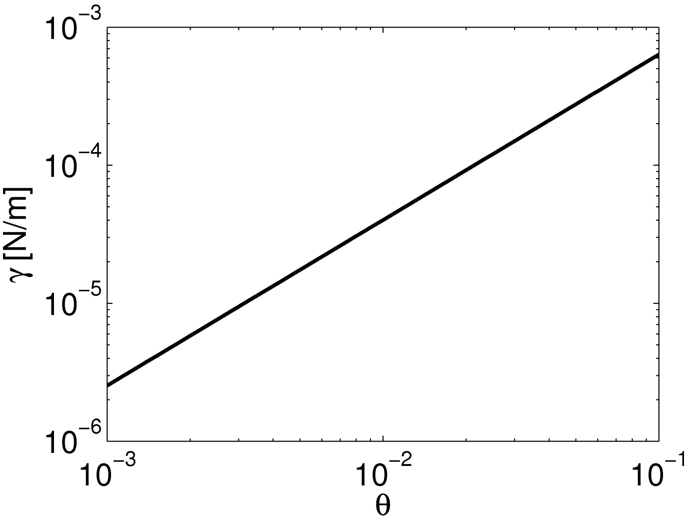

Figure 3.31: The interfacial tension of the two phases depend on temperature. Using equation (3.78) with the coefficients given by [6], the diffusion coefficients for the water/isobutoxyethanol system are calculated for a range of reduced temperatures.

3.A.6 Molar Volume

Another quantity that we need to look at for the comparison of the theoretical prediction for oscillation periods with the experimental data is the molar volume. It is the volume

V_m of one mol of the mixture. According to [41], it can be approximated by

$$V_\mathrm{m} = \phi^n V_\mathrm{m}^a + (1 - \phi^n) V_\mathrm{m}^b \tag{3.79}$$

with $V_\mathrm{m}^{a,b}$ being the apparent molar volumes of the pure components a,b in the binary mixture. In [41] we find $V_\mathrm{m} = 124\mathrm{cm}^3/\mathrm{mol}$ for isobutoxyethanol and $V_\mathrm{m} = 15.98\mathrm{cm}^3/\mathrm{mol}$ for water. The temperature dependence of the molar volume is shown in figure 3.32.

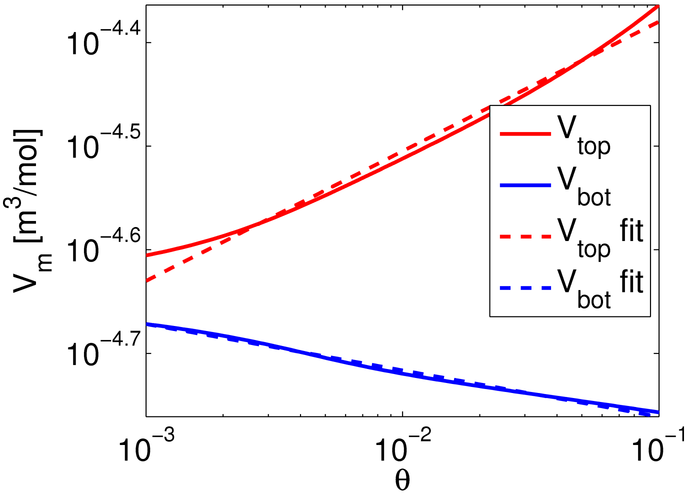

Figure 3.32: The molar volumes of the two phases depend on temperature. Using equation (3.79) with the coefficients given by [41], the molar volumes for the water/isobutoxyethanol system are calculated for a range of reduced temperatures. The molar volumes of the two phases are fitted by scaling laws $V_\mathrm{m,top} \sim \theta^{0.13}$ and $V_\mathrm{m,bot} \sim \theta^{-0.04}$.

3.A.7 Prefactor in Lifshitz-Slyozov theory

Lifshitz-Slyozov theory for droplet growth [69] (see section 3.6.2.1) uses a lengthscale which is defined by

$$\sigma \equiv \frac{2\gamma V_\mathrm{m} \mathit{\Phi}_\mathrm{e}}{RT}, \tag{3.80}$$

see section 3.6.2.1. The surface tension is denoted by γ, V_m is the molecular volume, $\mathit{\Phi}_\mathrm{e}$ is the equilibrium minority component concentration, R the gas constant and T the absolute temperature. Apart from the ideal gas constant R, all involved parameters are temperature dependent. In figure 3.33 we show how the lengthscale depends on temperature.

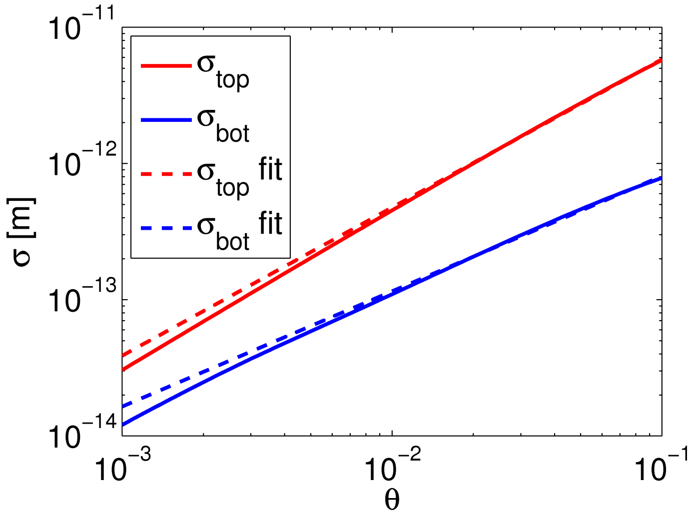

Figure 3.33: The prefactor σ of Lifshitz-Slyozov theory for the two phases depends on temperature. It is defined by equation (3.80). We show its temperature dependence for the water/isobutoxyethanol system for a range of reduced temperatures. Note the subatomar order of magnitude. It should be regarded as a temperature dependent prefactor with the unit of a length, rather than as an actual length scale involved in the process of Ostwald ripening. The prefactors of the two phases are fitted by scaling laws $\sigma_{\mathrm{top}} \sim \theta^{1.09}$ and $\sigma_{\mathrm{bot}} \sim \theta^{0.85}$.

4 Summary

In the present thesis, we have studied the evolution of droplet size distributions in two different hydrodynamic systems. For each setting, we have designed and constructed an experimental setup, which has been optimized to image droplets from the smallest possible scale $\mathcal{O}(\mu\text{m})$ to the largest $\mathcal{O}(\text{mm})$.

Image Processing The main challenge of the project has been to develop an image processing algorithm from scratch for each type of images. In high resolution images of breath figures, we have managed to detect almost 3 decades of droplet radii simultaneously in each individual image (confer figure 2.12 in section 2.4.2). The formidable reliability of the droplet detection in the low resolution images has enabled us to detect and characterize multi-droplet-coalescence and dripping events (see figure 2.25).
For our investigations on polydisperse sedimenting droplets in binary fluids we developed a droplet detection and tracking algorithm (described in section 3.5) validated to work reliable for droplet radii down to 3μm (confer figure 3.18). This enabled us to get detailed knowledge about the evolution of the droplet size distribution in phase separating binary fluids and to measure droplet and flow velocities (section 3.6.2.3).

Droplet Distribution of Breath Figures For the first time, not only droplet size distributions but also spatial correlations of droplet sizes (section 2.5.3) in breath figures have been measured (confer figure 2.19). We have extended the scaling theory of Family and Meakin [46] incorporating the concept of the fractal dimension of packings in section 2.5.1. Thus we have explained the scaling of the droplet size distribution observed in numerical simulations and the present experiments (figure 2.15). We have shown how the growth rate of the smallest droplets affects the lower end of the droplet size distribution (equation (2.45)). Fully rescaled droplet size distributions for experimental and numerical data with flat tails are shown in figure 2.16. We have measured a pronounced peak in the pair distribution function of adjacent droplets (figure 2.19) and established a connection to the shape of the droplet size distribution in section 2.5.3.5.

Bottleneck in Droplet Growth As a second system, we have studied the oscillations in the phase separation of binary fluids. We have shown that the droplet size distribution undergoes repeated precipitation cycles, described in section 3.6.1.2. Starting with a simple model for the growth rate of droplet radii (3.53), we have predicted in section 3.6.2.4

the bottleneck in droplet growth on the basis of measured droplet number and volume densities (3.54). We have demonstrated that the bottleneck in droplet growth describes the peak of the droplet volume distribution very well, as can be seen in figure 3.23. Hence there is strong evidence that we arrived at a consistent description of droplet growth in phase separating binary fluids. We have shown that the number of droplets created in each oscillation cycle is proportional to the driving rate and has a strong temperature dependence (compare figure 3.24). However, a satisfactory model for the droplet number density created by the temperature ramp is still missing.

Oscillation Period and Amplitude Based on our analysis of the bottleneck in droplet growth, we derived a prediction for the oscillation period (3.67) and amplitude of the droplet volume fraction in section 3.6.3. With the fully automated experimental setup (described in section 3.4) we have investigated the parameter dependence of the oscillation period on the driving rate, temperature and geometry of the sample. In figure 3.26 we show that the oscillation period scales with the driving rate with a nontrivial exponent $\Delta t \sim \xi^{-3/7}$ as predicted by our model (3.67). Fixing the only fit parameter by the oscillation period data of one layer, we get good agreement also with the data of the other layer. Further more, we find a scaling of the amplitude in the volume fraction oscillation with $v \sim \xi^{4/7}$ in agreement with our model (figure 3.25). Our model implies that the decrease of the oscillation period and amplitude with increasing temperature is due to the increase of the density difference between the two phases and the decrease in the number density, as outlined in section 3.6.3.3. Also in agreement with our prediction, we find no dependence of the oscillation period on the height of the sample (figure 3.27), the width, the height of the other layer or the type of the temperature protocol. Finally, we can conclude, that we solved the riddle of the drift in the oscillation period and amplitude that was observed in literature (confer section 3.1.1) together with the unknown driving dependence .

List of Figures

List of Tables

Bibliography

[1] Shabira Abbas, John Satherley, and Robert Penfold. The liquid-liquid coexistence curve and the interfacial tension of the methanol-n-hexane system. *J Chem Soc, Faraday Trans*, 93(11):2083–2089, 1997. Cited on page 69.

[2] M. Issa Abdul-Hadi. An analytical investigation into dropwise condensation of different steam-air mixtures on substrates of various materials. *The Canadian Journal of Chemical Engineering*, 57(4):459–466, 1979. Cited on page 1.

[3] Aitken. Breath figures. *Nature*, 86:516–517, 1911. Cited on pages 1 and 5.

[4] Aitken. Breath figures. *Nature*, 90:619–621, 1913. Cited on pages 1 and 5.

[5] Jean-Regis Angilella. Asymptotic analysis of chaotic particle sedimentation and trapping in the vicinity of a vertical upward streamline. *Phys Fluids*, 19(7):073302, 2007. Cited on page 1.

[6] M. Aratono, S. Nakayama, N. Ikeda, and K. Motomura. Thermodynamic consideration on the interface formation of water and ethylene glycol isobutyl ether mixture. *Colloid & Polymer Science*, 268(9):877–882, 1990-09-01. Cited on pages 88 and 129.

[7] M. J. Assael and S. K. Polimatidou. Measurements of the viscosity of alcohols in the temperature range 290-340 k at pressures up to 30 mpa. *International Journal of Thermophysics*, 15(1):95–107, 1994. Cited on page 88.

[8] Gunter K. Auernhammer, Doris Vollmer, and Jurgen Vollmer. Oscillatory instabilities in phase separation of binary mixtures: Fixing the thermodynamic driving. *J Chem Phys*, 123(13):134511–8, October 2005. Cited on pages 3, 69, 70, 81, 85, 86, 105, 118, and 121.

[9] Robert Aveyard, Bernard P. Binks, and John H. Clint. Emulsions stabilised solely by colloidal particles. *Adv Colloid Interface Sci*, 100-102:503–546, February 2003. Cited on page 93.

[10] Orlando Ayala, Bogdan Rosa, and Lian-Ping Wang. Effects of turbulence on the geometric collision rate of sedimenting droplets. part 2. theory and parameterization. *New J Phys*, 10(7):075016, 2008. Cited on page 73.

[11] Orlando Ayala, Bogdan Rosa, Lian-Ping Wang, and Wojciech W Grabowski. Effects of turbulence on the geometric collision rate of sedimenting droplets. part 1. results from direct numerical simulation. *New J Phys*, 10(7):075015, 2008. Cited on page 73.

[12] Khandekar S. Muralidhar K. Bansal, G.D. Measurement of heat transfer during drop-wise condensation of water on polyethylene. *Nanoscale and Microscale Thermophysical Engineering*, 13(3):184–201, 2009. cited By (since 1996) 1. Cited on pages 5 and 21.

[13] G.K. Batchelor. *An Introduction to Fluid Dynamics.* Cambridge University Press, 2005. Cited on pages 93, 98, and 112.

[14] K.V. Beard and H.T. Ochs. Warm-rain initiation: An overview of microphysical mechanisms. *Journal of Applied Meteorology and Climatology*, 32(4):608–625, April 1993. Cited on pages 1 and 72.

[15] I. J. Benczik and J. Vollmer. A reactive-flow model of phase separation in fluid binary mixtures with continuously ramped temperature. *Europhys Lett*, 91(3): 36 003, 2010. Cited on pages 3, 80, and 121.

[16] D. Beysens. The formation of dew. *Atmospheric Research*, 39(1-3):215–237, October 1995. Cited on pages 1 and 12.

[17] D. Beysens. Dew nucleation and growth. *Comptes Rendus Physique*, 7(9-10):1082–1100, November 2006. Cited on pages 1, 5, 12, 13, and 35.

[18] D. Beysens and C. M. Knobler. Growth of breath figures. *Phys Rev Lett*, 57(12):1433–, September 1986. Cited on pages 1, 5, 8, and 14.

[19] D. Beysens, A. Steyer, P. Guenoun, D. Fritter, and C. M. Knobler. How does dew form? *Phase Transitions*, 31(1):219–246, 1991. Cited on page 1.

[20] D. K. Biegelsen, F. A. Ponce, B. S. Krusor, J. C. Tramontana, and R. D. Yingling. Graded-thickness samples for molecular beam epitaxial growth studies of gaas/si heteroepitaxy. *Appl. Phys. Lett.*, 52(21):1779–1781, 1988. Cited on page 5.

[21] K. Binder. Spinodal decomposition in confined geometry. *J. Non-Equilib. Thermodyn.*, 23:1–44, 1998. Cited on page 80.

[22] Bernard P. Binks. Particles as surfactants — similarities and differences. *Curr Opin Colloid Interface Sci*, 7(1-2):21–41, March 2002. Cited on page 93.

[23] Johannes P. Blaschke. Formation and evolution of breath figures. Master's thesis, Physics Department of Philipps-University Marburg, 2010. Cited on pages 2, 6, 10, 33, 34, 38, 42, 54, 59, and 60.

[24] E. Bodenschatz, S. P. Malinowski, R. A. Shaw, and F. Stratmann. Can we understand clouds without turbulence? *Science*, 327(5968):970–971, 2010. Cited on pages 71 and 73.

[25] Daniel Bonn, Jens Eggers, Joseph Indekeu, Jacques Meunier, and Etienne Rolley. Wetting and spreading. *Reviews of Modern Physics*, 2008. Cited on page 8.

[26] M Borkovec, W de Paris, and R Peikert. The fractal dimension of the Apollonian sphere packing. *Fractals*, 2(4):521–526, 1994. Cited on page 17.

[27] D Boyd. The sequence of radii of the Apollonian packing. *mathematics of computation*, 39:249–254, January 1982. Cited on page 17.

[28] A.J. Bray. Theory of phase-ordering kinetics. *Advances in Physics*, 43(3):357–459, June 1994. Cited on pages 75 and 77.

[29] Jean-Louis Brenguier and Laure Chaumat. Droplet spectra broadening in cumulus clouds. part i: Broadening in adiabatic cores. *Journal of the Atmospheric Sciences*, 58(6):628–641, 2001. Cited on pages 71 and 72.

[30] B J Briscoe and K P Galvin. The evolution of a 2d constrained growth system of droplets-breath figures. *Journal of Physics D: Applied Physics*, 23(4):422, 1990. Cited on pages 1, 5, and 12.

[31] B. J. Briscoe and K. P. Galvin. Growth with coalescence during condensation. *Phys Rev A*, 43(4):1906–, February 1991. Cited on pages 10 and 12.

[32] A. N. Campbell and S. C. Anand. Densities, excess volumes, surface tensions, viscosities, and dielectric constants of the systems: Methanol – cyclohexane, acetone – methanol, acetone – cyclohexane, and methanol – cyclohexane – acetone. *Canadian Journal of Chemistry*, 50(8):1109–1114, 1972. Cited on page 88.

[33] M. E. Cates, J. Vollmer, A. Wagner, and D. Vollmer. Phase separation in binary fluid mixtures with continuously ramped temperature. *Philos Trans R Soc London, Ser A*, 361(1805):793–807, April 2003. Cited on pages 3, 69, 81, and 118.

[34] Fikrettin Celik and John D. Marwitz. Droplet spectra broadening by ripening process. part i: Roles of curvature and salinity of cloud droplets. *Journal of the Atmospheric Sciences*, 56(17):3091–3105, 1999. Cited on pages 71 and 72.

[35] Laure Chaumat and Jean-Louis Brenguier. Droplet spectra broadening in cumulus clouds. part ii: Microscale droplet concentration heterogeneities. *Journal of the Atmospheric Sciences*, 58(6):642–654, 2001. Cited on pages 71 and 72.

[36] William R. Cotton and Richard A. Anthes. *Storm and Cloud Dynamics*. Academic Press, 1989. Cited on page 1.

[37] John N. Coupland and D. Julian McClements. Droplet size determination in food emulsions: comparison of ultrasonic and light scattering methods. *Journal of Food Engineering*, 50(2):117 – 120, 2001. Cited on page 1.

[38] Vassilios Dallas Dallas and J. Christos Vassilicos. Rain initiation in warm clouds. 2010. Cited on page 73.

[39] Hideshige Doi, Katsutoshi Tamura, and Sachio Murakami. Thermodynamic properties of aqueous solution of 2-isobutoxyethanol at T = (293.15, 298.15, and 303.15) K, below and above LCST. *J Chem Thermodyn*, 32(6):729–741, June 2000. Cited on pages 88, 126, and 127.

[40] Joachim Domnick. Effect of bell geometry in high-speed rotary bell atomization. In *23rd Annual Conference on Liquid Atomization and Spray Systems*, Brno, Czech Republic, September 2010. ILASS - Europe. Cited on page 69.

[41] Gerard Douheret, Michael I. Davis, Joao Carlos R. Reis, Inger Johanne Fjellanger, Marit Bo Vaage, and Harald Hoiland. Aggregative processes in aqueous solutions of isomeric 2-butoxyethanols at 298.15 k. *Phys Chem Chem Phys.*, 4(24):6034–6042, 2002. Cited on pages 88 and 130.

[42] Jens Eggers. Existence of receding and advancing contact lines. *Phys Fluids*, 17:082106–1–082106–10, 2005. Cited on page 7.

[43] Lawrence D. Eicher and Bruno J. Zwolinski. Molecular structure and shear viscosity. isomeric hexanes. *The Journal of Physical Chemistry*, 76(22):3295–3300, October 1972. Cited on page 88.

[44] G. Falkovich, A. Fouxon, and M. G. Stepanov. Acceleration of rain initiation by cloud turbulence. *Nature*, 419(6903):151–154, September 2002. Cited on pages 1 and 73.

[45] Fereydoon Family and Paul Meakin. Scaling of the droplet-size distribution in vapor-deposited thin films. *Phys Rev Lett*, 61(4):428–, July 1988. Cited on pages 5, 14, and 33.

[46] Fereydoon Family and Paul Meakin. Kinetics of droplet growth processes: Simulations, theory, and experiments. *Phys Rev A*, 40(7):3836–3854, October 1989. Cited on pages 1, 2, 3, 5, 6, 14, 15, 16, 17, 18, 33, 36, 40, 42, 46, 59, 60, and 133.

[47] R. Ferrara, G. Fiocco, and Tonna G. Evolution of the fog droplet size distribution observed by laser scattering. *Applied Optics*, 9:2517–2521, 1970. Cited on page 1.

[48] Marshall Fixman. Viscosity of critical mixtures. *J. Chem. Phys.*, 36(2):310–318, 1962. Cited on page 88.

[49] DME Foster. On the exponent of the Apollonian packing of circles. *Journal of the London Mathematical Society*, 2(2):281, 1971. Cited on page 17.

[50] SD Fowler and P Greenspan. Application of Nile red, a fluorescent hydrophobic probe, for the detection of neutral lipid deposits in tissue sections: comparison with oil red O. *J Histochem Cytochem*, 33(8):833–836, 1985. Cited on page 84.

[51] Daniela Fritter, Charles M. Knobler, and Daniel A. Beysens. Experiments and simulation of the growth of droplets on a surface (breath figures). *Phys Rev A*, 43(6):2858–, March 1991. Cited on pages 1, 5, 9, 10, 12, 13, and 35.

[52] Daniela Fritter, Charles M. Knobler, Didier Roux, and Daniel Beysens. Computer simulations of the growth of breath figures. *Journal of Statistical Physics*, 52(5):1447–1459, September 1988. Cited on pages 1 and 5.

[53] Hartmut Gau and Stephan Herminghaus. Ripening of ordered breath figures. *Phys Rev Lett*, 84(18):4156–, May 2000. Cited on pages 1 and 60.

[54] J.W Gibbs. *Scientific Papers of J Willard Gibbs.* Dover, New York, 1961. Cited on page 79.

[55] Rafael C. Gonzalez, Richard E. Woods, and Steven l. Eddins. *Digital Image Processing Using MATLAB.* Pearson Education, Inc., 2004. Cited on pages 30, 51, 95, and 151.

[56] Wojciech W. Grabowski and Paul Vaillancourt. Comments on "preferential concentration of cloud droplets by turbulence:effects on the early evolution of cumulus cloud droplet spectra". *Journal of the Atmospheric Sciences*, 56(10):1433–1436, 1999. Cited on page 73.

[57] Clark Graham and Peter Griffith. Drop size distributions and heat transfer in dropwise condensation. *Int. J. Heat Mass Transfer*, 16:337–346, 1973. Cited on pages 1 and 5.

[58] RL Graham, JC Lagarias, CL Mallows, AR Wilks, and CH Yan. Apollonian circle packings: number theory. *Journal of Number Theory*, 100(1):1–45, 2003. Cited on page 17.

[59] Carlos A. Grattoni, Richard A. Dawe, C. Yen Seah, and Jane D. Gray. Lower critical solution coexistence curve and physical properties (density, viscosity, surface tension, and interfacial tension) of 2,6-lutidine + water. *Journal of Chemical & Engineering Data*, 38(4):516–519, 1993. Cited on page 69.

[60] Yumino Hayase, Mika Kobayashi, Doris Vollmer, Harald Pleiner, and Gunter K. Auernhammer. Asymmetric oscillations during phase separation under continuous cooling: A simple model. *J Chem Phys*, 129(18):184109–7, November 2008. Cited on pages 3, 69, 71, 105, and 118.

[61] L. M. Hocking and P. R. Jonas. The collision efficiency of small drops. *Q.J.R. Meteorol. Soc.*, 96(410):722–729, 1970. Cited on page 1.

[62] Bin Hu, Panagiota Angeli, Omar K. Matar, Christopher J. Lawrence, and Geoffrey F. Hewitt. Evaluation of drop size distribution from chord length measurements. *AlChE J*, 52(3):931–939, 2006. Cited on pages 1 and 93.

[63] Alain Karma and Armand Sarkissian. Dynamics of banded structure formation in rapid solidification. *Phys Rev Lett*, 68(17):2616–, April 1992. Cited on page 69.

[64] Piotr Korczyk, Szymon P. Malinowski, and Tomasz A. Kowalewski. Mixing of cloud and clear air in centimeter scales observed in laboratory by means of particle image velocimetry. *Atmospheric Research*, 82(1-2):173–182, November 2006. Cited on page 72.

[65] Mark Kreizer, David Ratner, and Alex Liberzon. Real-time image processing for particle tracking velocimetry. *Exp Fluids*, 48(1):105–110–110, 2010. Cited on page 93.

[66] Dennis Lamb. *Severe Convective Storms*, volume 28 of *Meteorological Monographs*. American Meteorological Society, Boston, 2001. Cited on pages 71 and 72.

[67] Tobias Lapp, Martin Rohloff, Jürgen Vollmer, and Björn Hof. Particle tracking for polydisperse sedimenting droplets in phase separation. arXiv:1107.1194. Cited on pages 74, 94, 102, and 112.

[68] J. Leopoldes and D. G. Bucknall. Coalescence of droplets on chemical boundaries. *Europhys Lett*, 72(4):597, 2005. Cited on page 5.

[69] I. M. Lifshitz and V. V. Slyozov. The kinetics of precipitation from supersaturated solid solutions. *J. Chem. Phys. Solids*, 19:pp 35, 1963. Cited on pages 109 and 130.

[70] J Lovick, AA Mouza, SV Paras, GJ Lye, and P Angeli. Drop size distribution in highly concentrated liquid/liquid dispersions using a light back scattering method. *J Chem Technol Biotechnol*, 80(5):545–552, 2005. Cited on pages 1 and 93.

[71] S. Maaß, S. Wollny, A. Voigt, and M. Kraume. Experimental comparison of measurement techniques for drop size distributions in liquid/liquid dispersions. *Exp Fluids*, 50(2):259–269, 2011. Cited on page 93.

[72] H. G. Maas, A. Gruen, and D. Papantoniou. Particle tracking velocimetry in three-dimensional flows. *Exp Fluids*, 15(2):133–146, 1993. Cited on page 93.

[73] S. Maass, J. Grünig, and M. Kraume. Measurement techniques for drop size distributions in stirred liquid-liquid systems. *Chem Process Eng*, 30:635–651, 2009. Cited on pages 1 and 93.

[74] N. A. Malik, Th. Dracos, and D. A. Papantoniou. Particle tracking velocimetry in three-dimensional flows. *Exp Fluids*, 15(4):279–294, 1993. Cited on page 93.

[75] Szymon P Malinowski, Miroslaw Andrejczuk, Wojciech W Grabowski, Piotr Korczyk, Tomasz A Kowalewski, and Piotr K Smolarkiewicz. Laboratory and modeling studies of cloud-clear air interfacial mixing: anisotropy of small-scale turbulence due to evaporative cooling. *New J Phys*, 10(7):075020, 2008. Cited on pages 1 and 73.

[76] S. S. Manna. Space filling tiling by random packing of discs. *Physica A: Statistical Mechanics and its Applications*, 187(3-4):373 – 377, 1992. Cited on pages 17 and 18.

[77] SS Manna and HJ Herrmann. Precise determination of the fractal dimensions of Apollonian packing and space-filling bearings. *Journal of Physics A*, 24(1991):481–490, July 2004. Cited on page 17.

[78] M. R. Maxey. The gravitational settling of aerosol particles in homogeneous turbulence and random flow fields. *Journal of Fluid Mechanics*, 174:441–465, 1987. Cited on page 73.

[79] Paul Meakin. Droplet deposition growth and coalescence. *Rep. Prog. Phys.*, 55:157–240, 1992. Cited on pages 5 and 12.

[80] Paul Meakin. Steady state behavior in a model for droplet growth, sliding and coalescence: the final stage of dropwise condensation. *Physica A: Statistical and Theoretical Physics*, 183(4):422–438, May 1992. Cited on pages 5 and 16.

[81] K. Menzel, S. Z. Mirzaev, and U. Kaatze. Crossover behavior in micellar solutions with lower critical demixing point: Broadband ultrasonic spectrometry of the isobutoxyethanol-water system. *Phys Rev E*, 68(1):011501, July 2003. Cited on pages 88, 127, and 128.

[82] M. Muselli, D. Beysens, M. Mileta, and I. Milimouk. Dew and rain water collection in the dalmatian coast, croatia. *Atmospheric Research*, 92(4):455–463, 2009. Cited on page 5.

[83] F. J. Muzzio, M. Tjahjadi, and J. M. Ottino. Self-similar drop-size distributions produced by breakup in chaotic flows. *Phys. Rev. Lett.*, 67(1):54–57, July 1991. Cited on page 1.

[84] H. Nakayama, H. Kanenaga, and T. Fujioka. The study of water structure in aqueous solutions of butoxyethanol by enthalpy of mixing measurements. *J Therm Anal Calorim*, 64(1):193–199, April 2001. Cited on pages 69, 83, and 84.

[85] R. D. Narhe and D. A. Beysens. Nucleation and growth on a superhydrophobic grooved surface. *Phys Rev Lett*, 93(7):076103–, August 2004. Cited on page 5.

[86] V. S. Nikolayev, D. Beysens, A. Gioda, I. Milimouka, E. Katiushin, and J. P. Morel. Water recovery from dew. *Journal of Hydrology*, 182(1-4):19–35, July 1996. Cited on pages 1 and 5.

[87] Kevin J. Noone, John A. Ogren, and Jost Heintzenberg. An examination of clouds at a mountain-top site in central sweden: The distribution of solute within cloud droplets. *Atmospheric Research*, 25(1-3):3 – 15, 1990. <ce:title>Cloud Physics Conference, Part 2 </ce:title>. Cited on page 72.

[88] Nicholas Ouellette, Haitao Xu, and Eberhard Bodenschatz. A quantitative study of three-dimensional Lagrangian particle tracking algorithms. *Exp Fluids*, 40(2):301–313, 2006. Cited on page 93.

[89] Josef Podzimek. Droplet concentration and size distribution in haze and fog. *Studia Geophysica et Geodaetica*, 41(3):277–296, July 1997. Cited on page 1.

[90] H. R. Pruppacher and J. D. Klett. *Microphysics of Clouds and Precipitation.* Kluwer Academic Publications, 2nd edition, 1997. Cited on pages 1, 71, 72, 73, and 113.

[91] Rayleigh. Breath figures. *Nature*, 86:416–417, 1911. Cited on pages 1 and 5.

[92] Rayleigh. Breath figures. *Nature*, 90:436–438, 1912. Cited on pages 1 and 5.

[93] N. Riemer, A. S. Wexler, and K. Diehl. Droplet growth by gravitational coagulation enhanced by turbulence: Comparison of theory and measurements. *J Geophys Res*, 112(D7):D07204–, April 2007. Cited on page 1.

[94] Claudia Roero. Contact angle measurements of sessile drops deformed by a dc electric field. In *4th International Symposium on Contact Angle, Wettability and Adhesion*, Philadelphia, USA, 2004. Cited on page 8.

[95] T. M. Rogers, K. R. Elder, and Rashmi C. Desai. Droplet growth and coarsening during heterogeneous vapor condensation. *Phys. Rev. A*, 38(10):5303–, November 1988. Cited on pages 10, 11, 13, 17, 18, 43, 46, 47, and 52.

[96] Martin Rohloff. Measuring the droplet-size and velocity distributions in binary phase separation. Diploma Thesis, Max-Planck-Institute for Dynamics und Self-Organization and Georg-August-University Göttingen, 2011. Cited on pages 79, 84, 85, 86, 87, 94, 102, 103, 105, 107, 112, and 126.

[97] J. W. Rose and L. R. Glicksman. Dropwise condensation - the distribution of drop sizes. *Int. J. Heat Mass Transfer*, 16:411–425, 1973. Cited on pages 1, 5, and 16.

[98] Alfred Ruf, Jörg Worlitschek, and Marco Mazzotti. Modeling and Experimental Analysis of PSD Measurements through FBRM. *Part Part Syst Charact*, 17(4):167–179, 2000. Cited on page 93.

[99] P. G. Saffman and J. S. Turner. On the collision of drops in turbulent clouds. *Journal of Fluid Mechanics*, 1(01):16–30 M3 – 10.1017/S0022112056000020, 1956. Cited on page 73.

[100] Ebie M. Sam, Yumino Hayase, Gunter K. Auernhammer, and Doris Vollmer. Pattern formation in phase separating binary mixtures. *Phys. Chem. Chem. Phys.*, pages –, 2011. Cited on page 69.

[101] Friedhelm Schönfeld, Karl-Heinz Graf, Steffen Hardt, and Hans-Jürgen Butt. Evaporation dynamics of sessile liquid drops in still air with constant contact radius. *International Journal of Heat and Mass Transfer*, 51(13-14):3696–3699, July 2008. Cited on pages 1 and 5.

[102] L. E. Scriven and C. V. Sternling. The marangoni effects. *Nature*, 187(4733):186–188, July 1960. Cited on page 75.

[103] Raymond A. Shaw. Particle-turbulence interactions in atmospheric clouds. *Annu Rev Fluid Mech*, 35(1):183–227, 2003. Cited on pages 1, 72, and 73.

[104] A. I El Sherbini and A. M. Jacobi. Modeling condensate drops retained on the air-side of heat exchangers. Technical Report (217) 333-3115, Air Conditioning and Refrigeration Center University of Illinois Mechanical & Industrial Engineering Dept., Air Conditioning and Refrigeration Center University of Illinois Mechanical & Industrial Engineering Dept. 1206 West Green Street Urbana, IL 61801, February 2003. Cited on pages 1, 5, 10, 16, and 42.

[105] H. Siebert, S. Gerashchenko, A. Gylfason, K. Lehmann, L.R. Collins, R.A. Shaw, and Z. Warhaft. Towards understanding the role of turbulence on droplets in clouds: In situ and laboratory measurements. *Atmospheric Research*, 97(4):426–437, September 2010. Cited on page 72.

[106] Battoo N.K. Khandekar S. Muralidhar K. Sikarwar, B.S. Dropwise condensation underneath chemically textured surfaces: Simulation and experiments. *Journal of Heat Transfer*, 133(2):021501, 2011. cited By (since 1996) 1. Cited on page 5.

[107] Mark J. H. Simmons, Sohial H. Zaidi, and Barry J. Azzopardi. Comparison of laser-based drop-size measurement techniques and their application to dispersed liquid-liquid pipe flow. *Opt Eng*, 39:505, 2000. Cited on page 93.

[108] M. V. Smoluchowski. Drei vortrage über diffusion, brownsche bewegung und koagulation von kolloidteilchen. *Zeitschrift fur Physik*, 17:557–585, 1916. Cited on pages 18 and 54.

[109] J. R. Snider, H. Wex, D. Rose, A. Kristensson, F. Stratmann, T. Hennig, S. Henning, A. Kiselev, M. Bilde, M. Burkhart, U. Dusek, G. P. Frank, A. Kiendler-Scharr, T. F. Mentel, M. D. Petters, and U. Pöschl. Intercomparison of cloud condensation nuclei and hygroscopic fraction measurements: Coated soot particles investigated during the lacis experiment in november (lexno). *J. Geophys. Res.*, 115(D11):D11205–, June 2010. Cited on page 72.

[110] R. Stephen Sparks, Herbert E. Huppert, Takehiro Koyaguchi, and Mark A. Hallworth. Origin of modal and rhythmic igneous layering by sedimentation in a convecting magma chamber. *Nature*, 361:246–249, 1993. Cited on pages 1 and 69.

[111] B. Steinhoff and D. Woermann. Slowing down of the kinetics of liquid/liquid phase separation along the binodal curve of a binary liquid mixture with a miscibility gap approaching the critical point. *J Chem Phys*, 103(20):8985–8992, November 1995. Cited on pages 80, 88, 109, 128, and 129.

[112] A. Steyer, P. Guenoun, D. Beysens, and C. M. Knobler. Growth of droplets on a substrate by diffusion and coalescence. *Phys Rev A*, 44(12):8271–, December 1991. Cited on page 5.

[113] G. Stringano, G. Pascazio, and R. Verzicco. Turbulent thermal convection over grooved plates. *Journal of Fluid Mechanics*, 557:307–336, 2006. Cited on page 5.

[114] Roland Stull. *Meteorology for Scientists and Engineers.* Gary Garlson, Brooks/Cole, second edition edition, 2000. A Technical Companion Book with Ahrens' Meteorology Today. Cited on pages 72 and 73.

[115] Rafael Tadmor. Line energy and the relation between advancing, receding, and young contact angles. *Langmuir*, 20(18):7659–7664, 2004. Cited on page 8.

[116] Rafael Tadmor. Line energy, line tension and drop size. *Surface Science*, 602(14):L108–L111, July 2008. Cited on page 8.

[117] H. Tanaka. Measurements of drop-size distributions during transient dropwise condensation. *Journal of Heat Transfer*, 75:341–346, 1975. Cited on pages 1, 5, 16, and 60.

[118] Job H J Thijssen and Paul S Clegg. Emulsification in binary liquids containing colloidal particles: a structure-factor analysis. *J Phys Condens Matter*, 22(45):455102, 2010. Cited on page 93.

[119] Shashi Thutupalli, Ralf Seemann, and Stephan Herminghaus. Swarming behavior of simple model squirmers. *New Journal of Physics*, 13(7):073021, 2011. Cited on page 1.

[120] Paul A. Vaillancourt and M. K. Yau. Review of particle-turbulence interactions and consequences for cloud physics. *Bull Am Meteorol Soc*, 81(2):285–298, 2000. Cited on pages 1, 73, and 74.

[121] Francesco Varrato and Giuseppe Foffi. Apollonian packings as physical fractals. *Molecular Physics*, 2011. Cited on page 17.

[122] Emmanuel Villermaux and Benjamin Bossa. Single-drop fragmentation determines size distribution of raindrops. *Nat Phys*, 5(9):697–702, September 2009. Cited on pages 1 and 72.

[123] Jean Louis Viovy, Daniel Beysens, and Charles M. Knobler. Scaling description for the growth of condensation patterns on surfaces. *Phys. Rev. A*, 37:4965–4970, Jun 1988. Cited on pages 12 and 13.

[124] O. Vohl, S. K. Mitra, S. C. Wurzler, and H. R. Pruppacher. A wind tunnel study of the effects of turbulence on the growth of cloud drops by collision and coalescence. *J. Atmos. Sci.*, 56(24):4088–4099, December 1999. Cited on page 72.

[125] D. Vollmer. Phase separation in microemulsions: stepwise change of the droplet size. *Colloid & Polymer Science*, 278(8):728–735, August 2000. Cited on page 118.

[126] D. Vollmer, R. Strey, and J. Vollmer. Oscillating phase separation in microemulsions. i. experimental observation. *J Chem Phys*, 107(9):3619–3626, 1997. Cited on page 69.

[127] D. Vollmer, J. Vollmer, and R. Strey. Oscillations in the dynamics of temperature-driven phase separation. *Europhys Lett*, 39(3):245–250, July 1997.

[128] D. Vollmer, J. Vollmer, and A. J. Wagner. Oscillatory kinetics of phase separation in a binary mixture under constant heating. *Phys Chem Chem Phys*, 4:1380–1385, 2002. Cited on pages 3, 69, 70, 81, 84, and 118.

[129] J. Vollmer. Phase separation under ultraslow cooling: Onset of nucleation. *J Chem Phys*, 129(16):164502–8, October 2008. Cited on pages 77 and 78.

[130] J. Vollmer, G. K. Auernhammer, and D. Vollmer. Minimal model for phase separation under slow cooling. *Phys Rev Lett*, 98(11):115701, March 2007. Cited on pages 3, 69, 71, 80, 81, 105, and 121.

[131] Jürgen Vollmer and Doris Vollmer. Cascade nucleation in the phase separation of amphiphilic mixtures. *Faraday Discuss.*, 112:51–62, 1999. Cited on page 105.

[132] Jürgen Vollmer, Doris Vollmer, and Reinhard Strey. Oscillating phase separation in microemulsions. ii. description by a bending free energy. *J Chem Phys*, 107(9):3627–3633, 1997. Cited on page 69.

[133] James S. Walker and Chester A. Vause. Wiederkehrende phasen. *Spektrum der Wissenschaft*, page 86ff, 1987. Cited on pages 69 and 83.

[134] Robert C. Weast. *CRC Handbook of Chemistry and Physics.* CRC Press, Inc. Boca Raton, Florida, 69. edition, 1988-1989. Cited on pages 88, 127, and 128.

[135] Henry C. Wente. The stability of the axially symmetric pendent drop. *Pac. J. Math.*, 88:421–470, 1980. Cited on page 10.

[136] A. J. White and M. J. Hounslow. Modelling droplet size distributions in polydispersed wet-steam flows. *International Journal of Heat and Mass Transfer*, 43(11):1873–1884, June 2000. Cited on page 1.

[137] M Wilkinson. Ostwald ripening and the kinetics of rain initiation. arXiv:1106.0334v1 [physics.ao-ph], 2011. Cited on pages 73, 109, 111, 113, and 116.

[138] Xiu Qing Xing, David Lee Butler, Sum Huan Ng, Zhenfeng Wang, Steven Danyluk, and Chun Yang. Simulation of droplet formation and coalescence using lattice boltzmann-based single-phase model. *Journal of Colloid and Interface Science*, 311(2):609–618, July 2007. Cited on page 1.

[139] H. Yokoyama, A. Takano, M. Okada, and T. Nose. Phase diagram of star-shaped polystyrene/cyclohexane system: location of critical point and profile of coexistence curve. *Polymer*, 32(17):3218–3224, 1991. Cited on page 69.

[140] Seong Soo Yum and James G. Hudson. Adiabatic predictions and observations of cloud droplet spectral broadness. *Atmospheric Research*, 73(3-4):203–223, February 2005. Cited on pages 71 and 72.

[141] Jin-Qiang Zhong, Denis Funfschilling, and Guenter Ahlers. Enhanced heat transport by turbulent two-phase rayleigh-bénard convection. *Phys. Rev. Lett.*, 102:124501, Mar 2009. Cited on page 72.

[142] M. Zinke-Allmang, L. C. Feldman, and W. van Saarloos. Experimental study of self-similarity in the coalescence growth regime. *Phys Rev Lett*, 68(15):2358–, April 1992. Cited on pages 1 and 5.

Acknowledgements

I am grateful to Wilhelm Hüttner, Konstantin Christou, Kristian Hantke, Alberto de Lozar and Eric Stellamanns for enlightening discussions and experimental tests of several illumination techniques. I thank Doris Vollmer and Günther Auernhammer for advice in designing the setup, choosing the system and developing the experimental protocol. I thank Jens Pick and Thorsten Harenkamp for careful construction of the experiment and Thomas Eggers, Johannes Blaschke and Marc Avila for helping to get the image processing algorithm run on the cluster. Special thanks to Thomas Eggers for support on IT problems and challenges. I am thankful to Ulrich Degenhardt for pointing me towards the image processing book of Gonzalez et al. [55] which has served as a source of inspiration for the development of the image processing algorithm. I would like to thank Christoph Gögelein and Paul Steffen for helpful discussions and advice on running the project.

Further I am grateful for the possibility to work together with other students on parts of the project. I would like to thank Andrew Scullion for helping in optimizing the illumination of the breath figure setup and contributions to the data analysis, Elizabeth Heines for her commitment in performing measurements on the methanol/ hexane system and Johannes Blaschke for enlightening discussions and fruitful collaboration on breath figures. I am particularly grateful to Martin Rohloff for joining the work on phase separation and making substantial contributions to the project during his Diploma thesis. This includes measuring the phase diagram of water/isobutoxyethanol and calculating the temperature ramps, preparing and conducting a part of the phase separation measurements and developing the droplet tracking algorithm.

I thank Michael Wilkinson for enlightening discussions and for developing the main ideas for modeling the scaling of the oscillation period. I am grateful to Björn Hof and Jürgen Vollmer for the opportunity to be part of two thriving research groups and for exceptionally good working conditions. Thank you for all the freedom and the confidence in me so that I could balance work, social activities and family in a good way. I especially thank Björn Hof for the advice in designing and setting up the experiments and the support and advice in day-to-day work. In particular, I am grateful to Jürgen Vollmer for his advice, support and feedback in many areas. I thank him for the time he invested in supervising and teaching me and for giving me the possibility to work on such an interesting PhD-project.

I want to thank Izabella Benczik, Ilenia Battiato, Markus Holzner, Bernhard Altaner, Jan-Hendrik Trösemeier, Ariane Papke, Andreas Heymann, Björn Hof and of course Jürgen Vollmer for feedback on parts of the manuscript.

Finally, I want to say thanks to my wonderful wife Annette who supported and encouraged me through the course of the thesis and especially in the last few weeks. I thank my daughter Johanna for most joyful moments and for helping me to balance work with family and other activities. Last but not least I am in awe of the One who created everything that can be studied in physics and what is beyond scientific research.